

This is to certify that the

thesis entitled

SURFACE MODIFICATION OF ZINC SULFIDE BY ION IMPLANTATION WITH 200 KEV NICKEL IONS

presented by

STEPHEN CURTIS WHITE

has been accepted towards fulfillment of the requirements for

MASTERS degree in MATERIALS SCIENCE

Major professor

Date 12/22/93

O-7639

MSU is an Affirmative Action/Equal Opportunity Institution



LIBRARY Michigan State University

PLACE IN RETURN BOX to remove this checkout from your record.
TO AVOID FINES return on or before date due.

DATE DUE	DATE DUE	DATE DUE

MSU is An Affirmative Action/Equal Opportunity Institution characteristics pm3-p.1

SURFACE MODIFICATION OF ZINC SULFIDE BY ION IMPLANTATION WITH 200 KEV NICKEL IONS

Ву

Stephen Curtis White

A THESIS

Submitted to
Michigan State University
in partial fulfillment of the requirements
for the degree of

MASTER OF SCIENCE

Department of Metallurgy, Mechanics, and Materials Science
1993

ABSTRACT

SURFACE MODIFICATION OF ZINC SULFIDE BY ION IMPLANTATION WITH 200 KEV NICKEL IONS

By

Stephen Curtis White

Zinc sulfide is an important infrared transmitting optical window material. Because of it's brittleness and low strength it is vulnerable to erosion and impact damage in severe environments. It has been suggested by Kriven, et.al., that the compound nickel sulfide (NiS) could act as a metastable transformation toughener due to the positive volume expansion associated with the displacive transformation to the low temperature allotrope. was irradiated with 1 x 10¹⁷ ions/cm² of 200 keV Ni⁺ at approximately 400 K, aimed at producing metastable NiS precipitates capable of improving the strength and toughness of the surface layer of ZnS. The effect of ion implanation and postirradiation anneals upon the mechanical properties of ZnS were investigated through hardness evaluations, and evidence of precipitates were observed with transmission electron microscopy. Significant improvement in the hardness was found for postirradiated annealed zinc sulfide.

Copyright by

STEPHEN CURTIS WHITE

1994

ACKNOWLEDGEMENTS

I would like to thank Dr. David Grummon of the Department of Metallurgy, Mechanics, and Materials Science at Michigan State University for his technical guidance, encouragement, and patience throughout the duration of completing this work.

I would also like to thank Dr. Eldon Case of the Department of Metallurgy, Mechanics, and Materials Science at Michigan State University for his guidance and council with many technical issues within this project.

I thank Dr. A. J. Armini of Implant Sciences in Danvers, Massachusetts for contributing the implantation processing and computer modeling.

And, I thank my wife, Kathy, for her endless encouragement, motivating spirit, and sacrifices she made for this work, and mostly for her love.

TABLE OF CONTENTS

LIST OF TABLES	vi
LIST OF FIGURES	vii
CHAPTER 1. INTRODUCTION	
1.1 BACKROUND	1
1.2 ION IMPLANTATION	6
1.3 ION IMPLANTATION IN CERAMICS	14
1.4 ZINC SULFIDE	30
1.5 TRANSFORMATION TOUGHENING	33
1.6 NICKEL SULFIDE AS A TRANSFORMATION TOUGHENER	36
CHAPTER 2. EXPERIMENTAL PROCEDURE	41
2.1 SPECIMEN PREPARATION	41
2.1.1 Cutting	43
2.1.2 Polishing	44
2.1.3 Mounting	46
2.1.4 Ion Implantation	47
2.1.5 Dimple Grinding	48
2.1.6 Chemical Thinning	50
2.1.7 Ion Milling	55
2.2 X-RAY DIFFRACTION	64
2.3 TRANSMISSION ELECTRON MICROSCOPY	67
2.4 INDEXING TEM DIFFRACTION PATTERNS	69
2.5 HARDNESS	71

2.5.1 Nickel-implanted ZnS	71
2.5.2 Annealed Nickel-implanted ZnS	73
2.6 SCANNING ELECTRON MICROSCOPY	76
2.7 X-RAY PHOTOELECTRON SPECTROSCOPY	77
CHAPTER 3. RESULTS AND DISCUSSION	78
3.1 ION MILLING EFFECTS	78
3.2 X-RAY DIFFRACTION	89
3.3 TEM RESULTS	92
3.4 INDEXING DIFFRACTION PATTERNS	96
3.4.1 Zinc Sulfide	96
3.4.2 Nickel-implanted Zinc Sulfide	103
3.5 HARDNESS	115
3.5.1 Nickel-implanted Zinc Sulfide	116
3.5.2 Annealed Nickel-implanted Zinc Sulfide	118
3.6 SCANNING ELECTRON MICROSCOPY	125
3.7 X-RAY PHOTOELECTRON SPECTROSCOPY	133
3.8 DIFFUSION	139
CHAPTER 4. CONCLUSION	147
APPENDICES	
APPENDIX A. VICKERS INDENT HARDNESS DATA	151
APPENDIX B. BASIC PROGRAM - HARDNESS IN GIGAPASCALS	156
LIST OF REFERENCES	159

LIST OF TABLES

- Table 1. Chemical thinning durations and observations.
- Table 2. XRD diffraction data for β -ZnS.
- Table 3. Indexing data for SAD pattern of unmodified ZnS using camera constant of 2.035.
- Table 4. Indexing data for SAD pattern of unmodified ZnS using camera constant of 2.707.
- Table 5. Indexing data for irradiated ZnS using calibrated camera constant of 2.035.
- Table 6. Indexing data for "reflections" in irradiated ZnS with a camera constant of 2.097.
- Table 7. Indexing data for ring pattern of Figure 24 with camera constant of 2.097.
- Table 8. Indexing data for ring patterns from enlargement of Figure 24 with calibrated camera constant of 2.097.
- Table 9. Comparison of Ni-irradiated ZnS d-spacings to various phases of nickel, sulfur, and zinc.
- Table 10. Vickers hardness data for nickel-irradiated and non-irradiated ZnS pre- and post-anneal.
- Table 11. Binding energies of nickel, zinc, and sulfur.

LIST OF FIGURES

- Figure 1. Infra-red transmission wavelengths [2].
- Figure 2. Defect generation by ion implantation.
- Figure 3. Effect of varying ion dose in ceramic [13].
- Figure 4. Relative hardness of Cr-implanted alumina [18].
- Figure 5. Flexural strength of implanted alumina [19].
- Figure 6. Flexural strength of alumina with ion species [20].
- Figure 7. Nickel concentration in alumina [19].
- Figure 8. Knoop microhardness for YSZ [23].
- Figure 9. Atomic structure of zinc sulfide [29].
- Figure 10. Nickel-sulfur phase diagram [27].
- Figure 11. Slicing ZnS for TEM specimens.
- Figure 12. ZnS specimen arrangement for irradiation.
- Figure 13. Gatan hand-held disc grinder[35].
- Figure 14. Gatan Model 656 Dimple Grinder (top view)[35].
- Figure 15. Dimple grinder specimen mounts[35].
- Figure 16. Ion mill specimen holder cross-section.
- Figure 17. Anneal profiles of Ni-irradiated ZnS.

- Figure 18. TEM micrograph of thinned edge of 200keV Ni-irradiated ZnS. (Mag:100k)
- Figure 19. "Saw tooth" features observed in TEM micrograph of 200keV
 Ni-irradiated ZnS. (Mag:100k)
- Figure 20. Bright-field TEM micrograph of 200keV Ni-irradiated ZnS. (Mag:100k)
- Figure 21. "Reflections" observed in dark
 -field TEM micrograph of 200keV
 Ni-irradiated ZnS. (Mag:100k)
- Figure 22. Bright-field TEM micrograph in precipitant-rich region of Ni-irradiated ZnS. (Mag:100k)
- Figure 23. Dark-field image of region in
 Figure 22 showing precipitant
 reflections in Ni-irradiated ZnS.
 (Mag:100k)
- Figure 24. Selected-area diffraction pattern of 200keV nickel-irradiated ZnS. (Mag:100k)
- Figure 25. X-ray diffraction pattern of ZnS.
- Figure 26. Selected-area diffraction pattern of zinc sulfide.
 (Mag: 100k)
- Figure 27. Illustration of ZnS selected-area diffraction pattern of Figure 26.
- Figure 28. Monograph matching ZnS in Figure 26.[39]

- Figure 29. Illustration of Ni: ZnS pattern of Figure 24.
- Figure 30. Monograph matching Ni: ZnS in Figure 24.[39]
- Figure 31. Increase in Vickers hardness for 200keV Ni-irradiated ZnS and control samples with annealing.
- Figure 32. Scanning electron micrograph of zinc sulfide. (Mag:1100)
- Figure 33. Scanning electron micrograph of zinc sulfide surface "voids." (Mag:3300)
- Figure 34. Scanning electron micrograph of 200keV Ni-irradiated ZnS. (Mag:1100)
- Figure 35. Scanning electron micrograph of
 Ni-irradiated ZnS annealed to 750
 degrees celsius. (Mag:1100)
- Figure 36. Scanning electron micrograph of
 Ni-irradiated ZnS annealed to 850
 degrees celsius. (Mag:1100)
- Figure 37. X-Ray photoelectron spectrum of 200keV nickel-irradiated zinc sulfide.
- Figure 38. X-Ray photoelectron spectrum of 200keV nickel-irradiated zinc sulfide in region of nickel peak.
- Figure 39. X-Ray photoelectron spectrum of 200keV nickel-irradiated zinc sulfide in region of sulfur peak.
- Figure 40. X-Ray photoelectron spectrum of 200keV nickel-irradiated zinc sulfide annealed to 800 degrees celsius.

Figure 41. Distribution of 200keV nickel ions implanted into zinc sulfide.

CHAPTER 1. INTRODUCTION

1.1 BACKROUND

Thermal imaging systems detect energy in the form of radiation emitted by warm bodies which exhibit spectra in the wavelength range defined as infrared (IR). For operation in the earth's atmosphere, the application of IR optics is limited by selective transmission to three wavelength bands: 0.8-1.3 microns, 3-5 microns, and approximately 8-14 microns as shown in Figure 1 [1,2]. Use of these systems on aircraft expose the infrared optical material, or "window," to hostile environments. (This use of the term "window" refers to the actual optical material, such as ZnS or ZnSe, used in an IR detector, rather then the conventional reference to a band of wavelengths in the IR transmission spectra.) The purpose of the IR window is to protect the delicate imaging system from such environments while permitting reception and processing of input received via IR signals that pass through the window material. Output data is then generated by the input, and is used for telemetry and quidance.

Improvements in material selection and processing continue to be explored to enhance the effectiveness of IR windows in fulfilling these objectives. However, difficulties may lie in altering the window material properties and performance while maintaining the optical characteristics necessary for system

operation. Wien's displacement law [3] gives the wavelength of maximum emission, λ_{m} , for a blackbody radiating at a given absolute temperature T:

$$\lambda_{m}T = 2898 \text{ microns-Kelvin}$$
 (1)

For objects at an approximate temperature of 20 degrees celsius (298 Kelvin) the IR wavelength band between 8 and 14 microns is suitable for their detection. Zinc sulfide (ZnS) is IR transmitting in this range.

It has been observed that ZnS experiences mechanical damage and transmission losses as a result of impact with rain droplets [4,5,6]. Ceramics are most susceptible to failure in tension, thus it is probable that pre-existing flaws in the near-surface region of this ceramic experience growth initiated by radial tensile stresses. Rayleigh surface waves generated by the impacts with water droplets were reported to be the source of these stresses and considered to ultimately be responsible for the growth of surface cracks. Donald and McMillan [7] conclude that "any improvement in the mechanical properties of existing infrared materials should ideally be achieved by increasing the strain to failure of the material" and that the techniques which are the most suitable for achieving this are those involving surface modification.

Ion implantation has been studied considerably in the 1980's as a method to modify surface and near-surface regions of metals, ceramics, and polymers to improve properties such as wear resistance, hardness, and fracture toughness. Significant widespread interest in the implantation process for affecting such

a diverse range of materials attests to the unique advantages offered by ion implantation.

Fundamentally, ion implantation is the physical acceleration, bombardment, and injection of a particular ion species into the surface of a substrate. With typical energies ranging from 100,000 electron-volts (100 keV) to as high as 1 million electron-volts, a single ion may enter the target and come to rest in approximately 10⁻¹² seconds (1 picosecond). Essentially the effect is that of an extremely rapid cooling rate, or "quench." Thus, the thermodynamic constraints present during conventional surface-altering or alloying processes do not apply with this technique. Although thermal diffusion of atomic species is minimal, other mechanisms of atomic mobility may occur both during and shortly after the ion implantation process is complete. This will be explored in greater detail in the next section.

Ion implantation also offers no distinct interface between modified and unmodified regions. This is achieved by the intimate mixing of the projectile and target species as well as a gradual decrease in ion concentration with depth towards the bulk region. Therefore, interface delamination or debonding are not experienced by ion implanted materials.

The objective of the investigation described herein was to introduce a transformation toughener into the subsurface region of zinc sulfide. This was attempted by the ion implantation of nickel-beam ions into the subsurface region of a prepared surface of ZnS, followed by thermal annealing. Changes in hardness were observed as well as physical evidence of the atomic species

proposed to be responsible for improvements in the surface of this infra-red transmitting ceramic.

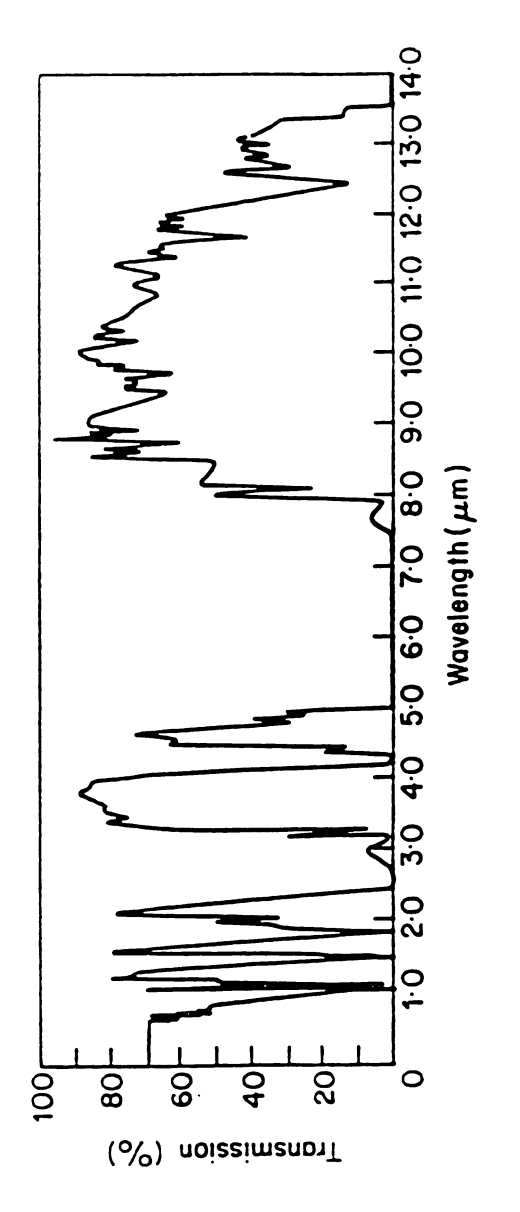


Figure 1. Infra-red transmission wavelengths [2].

1.2 ION IMPLANTATION

Ion implantation is gaining momentum as a method to alter the surface and sub-surface properties of ceramics used in various applications. This process is relatively advanced and can be considerably expensive, however, its advantages over conventional surface modification techniques have resulted in experimental investigations with respect to metals, ceramics, and polymers. These advantages are 1) a clean process, 2) lack of sharp interface thus no interface delamination, 3) potential to implant any material, 4) with any ion species, 5) at a wide range of accelerating voltages, 6) achieving a specified dose, and 7) without the thermodynamic equilibrium constraints normally associated with conventional processing.

The process of ion implantation is one of rapidly accelerating a selected ion species into a solid target. The atomic composition and structure of the near-surface region of the target are altered by the presence of the new species and resulting defects. Typically, the equilibrium solubility of the implanted species in the target material is exceeded. This occurs because of two characteristics of ion implantation.

First, is the relatively shallow depth to which a typically high dose of implanted ions penetrate into the target material in a very short time, resulting in a high concentration per unit volume of the implanted species in the sub-surface region. Second is due to the lack of thermal energy available for driving

temperature-dependent diffusion of this high concentration of implanted ions. The event marked by the ions impact and subsequent decceleration and dissipation of kinetic energy is a process which occurs in approximately 10^{-12} seconds [8]. The effects of such a "quench rate" coupled with the ability to maintain the implanted substrate at low temperatures releases the thermodynamic constraints associated with equilbrium dependent processes.

This implanted region may be considered to be in a metastable energy state. That is, the entire layer affected by ion implantation is in a higher Gibbs free energy state relative to the bulk material. However, each implanted ion comes to rest at a position that represents a local minimum energy state. The ions, having dissipated their kinetic energies through atomic and nuclear collisions, now possess insufficient energy to mobilize further towards an even lower Gibb's free energy position. An additional driving force such as thermal energy would be required to initiate this motion. The subsurface region, in effect, is one that is super-saturated with the implanted species, and metastable in terms of its energy state; a condition which lends itself to a precipitate transformation reaction of the type:

$$\alpha' --> \alpha + \beta$$
 (2)

where, α' = a metastable supersaturated solid solution,

 α = a structure identical to α' but closer to an equilibrium concentration, and

 β = a stable or metastable precipitate [9].

An accelerating ion incident upon a substrate loses its kinetic energy by interacting with the target material's atoms ("nuclear stopping") and electrons ("electronic stopping"). Elastic scattering by the atomic nuclei which are shielded by their electron configuration, and the ionizaiton of these electrons, constitutes the means by which most of the energy dissipation occurs [10]. Figure 2 depicts a binary atomic structure in which ions are being implanted. The path labeled "1" illustrates a non-displacing collision. In this case, as the incident ion passes by a stationary lattice atom, a portion of the ion's kinetic energy is imparted to the atom, temporarily increasing it's vibrational energy. The path of the ion is altered by this elastic scattering event and the lattice atom remains in its original position. (Many sources are available which discuss in detail the dynamics of particle collisions and the phenomena of vacancy and interstitial defect generation, radiation-enhanced diffusion, and ion channeling [8,10,11,12].)

A significant number of additional energy-loss processes also occur which result in the generation of a large number of defects by atomic rearrangement. One mechanism for this is the case in which the amount of energy imparted to a lattice atom exceeds its threshold displacement energy and the atom is displaced (primary displacement), leaving a vacant atomic position, or "vacancy" in the lattice structure. In Figure 2, this is depicted by path 2. The displaced lattice atoms with their newly absorbed vibrational energies, themselves, become "incident" ions. Each of these ions in turn lose their energy

by displacing additional atoms in the target ("secondary displacement"). This is shown by path 4 in which a lattice atom, having been displaced by an incident ion's second collision event (path 3), leaves its site and impacts and displaces another lattice atom of the same type.

Multiple occurrences of this type of event along an incident ion's path result in a "collision cascade" region. Many of the atomic positions closest to the ion's path become vacancies. The increased number of vacancies, which are point defects, significantly enhances the diffusivity of the various species, for vacancies are central to the mechanism by which substitutional atoms diffuse.

At the end of the displacement phase, many of the displaced atoms do not regain a position as in the original structure.

Depending on the incident and target species characteristics, there can be a high concentration of these atoms at interstitial positions within the lattice. These are referred to as "self-interstitial atoms" (SIA's). Many of these SIA's end up adjacent to vacancies. Such a vacancy-interstitial pair, referred to as a "Frenkel pair," is shown in the atomic model of Figure 2.

The incident ions form defects not only by the energy they impart but by their presence. Once they come to rest, an interstitial or substitutional defect is formed (labeled "i" or "s" in Figure 2). The ion species have sizes and energy characteristics that differ from the target material atoms and the substitutional ions may bond with the cations or anions of

the target material. As mentioned previously, their concentration usually exceeds equilibrium solubility limits, and their redistribution is dependent upon the various processes which occur in ion irradiated materials.

Atoms present in a region of high concentration in a material typically diffuse to regions of lower concentration, for this reduces the overall Gibb's Free Energy. "Radiation-enhanced diffusion" refers to the increased potential for diffusing species in irradiated materials due to the excess number of point defects and defect clusters that are introduced by the implantation process. As is true for the implanted species, the number of other defects generated by ion implantation typically far exceed their equilibrium concentrations. The diffusion of these defects, whether they are vacancy, substitutional, or interstitial, can be activated thermally either during ion implantation or with subsequent annealing. The result is an increased flux of defect migration due to the increased quantity of diffusing species. This redistribution is significant because it determines the change in properties of the modified material. Radiation-enhanced diffusion is a thermally activated process, therefore the microstructure is driven towards a state of equilibrium.

"Radiation-induced segregation" occurs by the influence of irradiation-generated defect fluxes upon the implanted species. The implanted ions "couple" to the defect fluxes and result in nonequilibrium concentration gradients. For example, such a gradient will exist between regions of high and low

concentrations of vacancies generated during implantation. As vacancies in the high region move across the gradient to the low region, the implanted atomic species will move accordingly, in the opposite direction of the vacancy flux. This type of vacancy motion can occur during the implantation process and is driven by the abrupt atomic changes taking place within the bombarded atomic structure. Activated independent of thermal energy, this activity typically drives towards a nonequilibrium state. Since this results in local changes in composition, precipitation of a second phase may be induced.

Both radiation-induced segregation and radiation-enhanced diffusion play significant roles in irradiated materials which undergo subsequent heat treament. Due to the nature of their mechanisms, radiation-induced segregation would be expected to be prevalent during ion implantation in which the target material is kept at a low temperature throughout the process. This results in a supersaturated region that has been rapidly generated.

Therefore, it would be metastable and more conducive to precipitation of a second phase, possibly assisted by the segregation of newly bonded species to second-phase embryo sites.

It follows that radiation-enhanced diffusion would most likely be the dominant effect during annealing of the implanted material. Second-phase precipitants which may have formed prior to annealing would grow in volume, thus moving the atomic structure closer to equilibrium.

The final results on morphology and mechanical properties

are ultimately governed by the characteristics of the constituents that are combined, and the parameters of the ion implantation process. Variations in both of these are reviewed in Section 1.3 on ion implantation in ceramic materials.

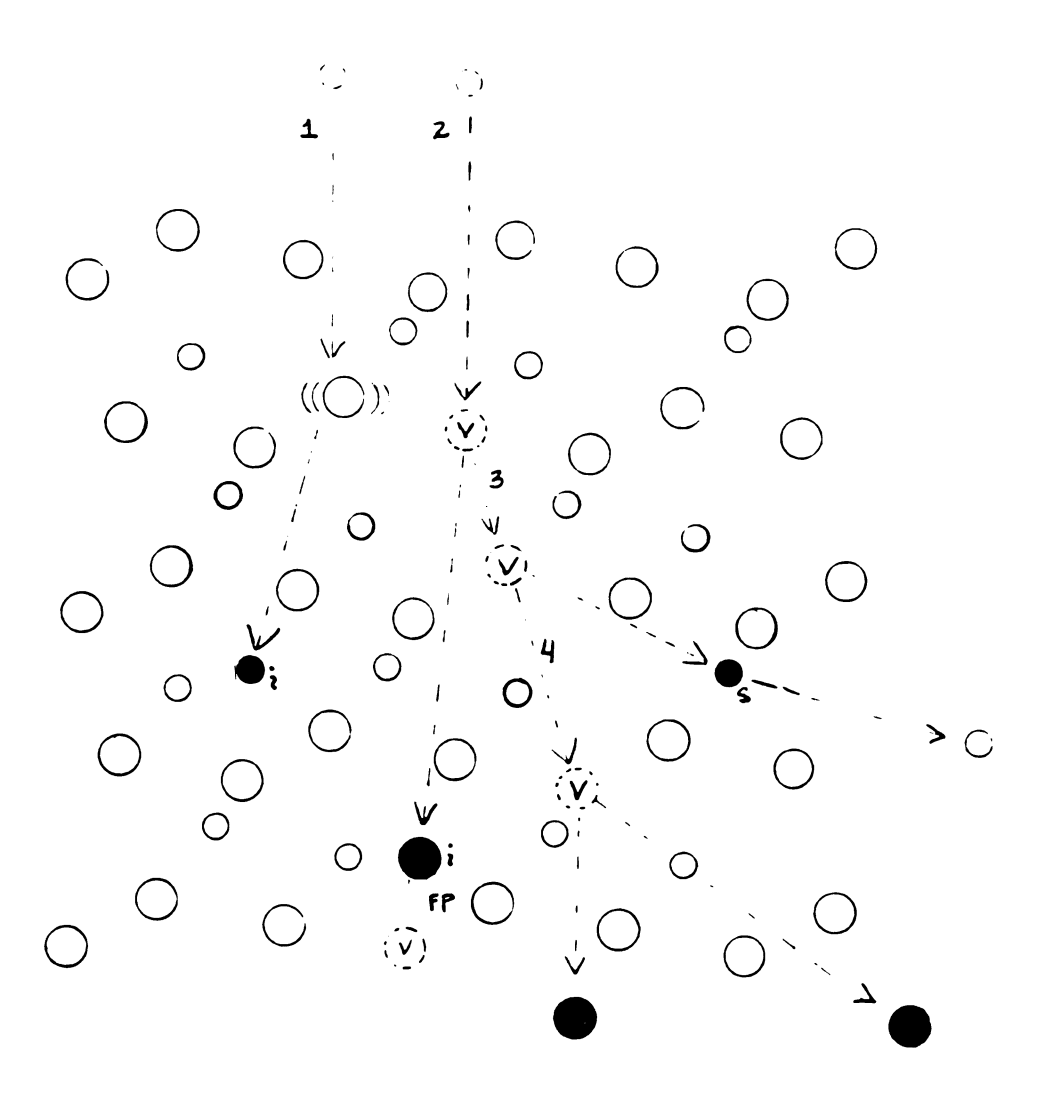


Figure 2. Defect generation by ion implantation.

1.3 ION IMPLANTATION IN CERAMICS

Various studies have shown that ion implantation into particular ceramic materials improves the mechanical properties of the material. It is known that when a load is applied to a ceramic, the tendency towards failure is due to the tensile components of the load. The corresponding stresses induced in the surface initiate and propagate cracks until failure occurs. Pre-existing cracks typically occur in ceramic materials and therefore are even more susceptible to cause damage or failure. These surface phenomena are amenable to modification by ion implantation.

The controllable factors which determine the characteristics of implantation are the ion dose (typically 10^{13} to 10^{18} ions per square centimeter for ceramics), the energy (typically 20 to 200 keV), incident ion mass, and target material. Of these, most commonly the ion dose, or "fluence," is varied.

McColm and Clark [13] illustrate the effect on the near-surface structure of a ceramic with varying ion dose (Figure 3). Three regions considered unique are described by the authors whom speculate on mechanisms which may be responsible for mechanical property improvements. A summary of these descriptions follow.

The lower dose of 10¹⁶ ions per square centimeter is labeled as Region I. The damage resulting from this fluence is low enough so that the solid maintains crystallinity, i.e. both short- and long-range order is maintained in the lattice

structure. Damage is present and substitutional and/or interstitial solid solutions contribute to surface hardening. By selecting a large ion relative to the substrate atomic size, implantation may result in a compressive stress which can inhibit crack initiation and propagation, thereby improving the surface toughness.

An amorphous layer just below the surface is marked by Region II in the figure from McColm and Clark. This layer is attributed to ion doses around 10¹⁷ ions per square centimeter. Surface softening, as observed by Burnett and Page in silicon [14], is expected due to the amorphous region. An increase in surface toughness may be realized due to the plasticity of this layer.

Region III corresponds to ion doses exceeding 10¹⁸ ions per square centimeter and possesses a thicker amorphous layer than Region II. Additionally, Region III begins at the material surface. It is likely that this is due to removal of the original surface by sputtering, thereby exposing the amorphous region of material. Flaw geometries in this region are altered and contribute to both the strength and the surface toughness. Many of the experimental investigations performed on ceramics subjected to ion implantation have led to observations which may be supported by the strengthening mechanisms suggested by McColm and Clark.

McHargue et. al. [15] implanted polycrystalline ${\rm TiB_2}$ (titanium diboride) with nickel ions at an energy of 1 MeV (1 MeV = 10^6 electron-volts). One use of ${\rm TiB_2}$ is as a thermal barrier coating for erosive and wear environments. Powder was

vacuum hot-pressed to produce specimens with a theoretical density of 98.4 percent and grain sizes ranging from 50 to 100 microns (10^{-6} meters) . A fluence of 1×10^{17} ions per square centimeter yielded TiB_2 with a nickel-titanium ratio of about 0.12. Specimens were prepared to permit transmission electron microscopy (TEM) of the cross-section of the implanted region and for hardness testing using a Knoop microhardness technique.

Bright-field and weak-beam dark-field micrographs of the implanted specimen revealed dislocation tangles in the implanted layer with a thickness of about 550 nanometers (1 nanometer = 10⁻⁹ meters). The dislocation density was moderate and relatively uniform. The local regions between these dislocation structures was viewed to be free of defects. Defects ranging from 5 to 10 nanometers were found to occupy the layered region extending from 550 nanometers to 750 nanometers. These defects were present in a greater density than that of the dislocation tangles. After 750 nanometers no damage was observed. As noted by the authors and confirmed by the presence of these defect species, the implanted layer remained crystalline.

Using a 15 gram load (0.147 Newtons) to measure Knoop microhardness, it was determined that the depth of the indentations (250-300 nanometers) would result in hardness data of the composite consisting of the modified layer and the unmodified substrate. Due to the relatively shallow depth of penetration of accelerated ions, this is generally the nature of the data for hardness of ion implanted ceramics. Thus, the results are usually reported as relative hardness values which

indicate whether the effects provide improvement or degradation of surface properties. Because of the hexagonal structure of ${\rm TiB}_2$ and the corresponding anisotropy, the hardness of individual grains were measured.

Relative hardness values of 1.7 to 2.0 were found. This represents a 70 to 100 percent increase over that of the unimplanted sample. After partial recovery of irradiation damage by annealing, a decrease in the hardness ratio from 1.7 to 1.45 resulted. An increase from 40 to 80 percent of indentation fracture toughness was determined from 0.49 and 0.98 Newton loads of Vickers indents. The methods of Evans [16] and Marion [17] were used to calculate the apparent fracture toughness reported above.

In a separate study, McHargue et. al. investigated the effect of ion implantation of alumina [18]. In this work, single crystals of aligned and random high purity $\mathrm{Al}_2\mathrm{O}_3$ were implanted with various ion species (Cr, Zr, Nb, Al+O, Xe) at temperatures of 77, 300, or 640 degrees Kelvin. Energies between 40 and 300 keV were used to implant fluences ranging from 10^{15} to 10^{17} ions per square centimeter, with current densities of approximately 2 microamps per square centimeter. Characterization techniques used were Rutherford backscattering-ion channeling (RBS-C), transmission electron microscopy, and Knoop microhardness.

It was observed by RBS-C that the aluminum and oxygen sublattices sustained significant damage at 300 degrees Kelvin, and metastable interstitial solid solutions were formed. A relative hardness increase of 50 percent was determined for a

specimen implanted with 10^{17} chromium ions per square centimeter at 300 Kelvin (Figure 4). It was also noted that a hardness increase only on the order of about 10 percent was found for a solid solution of Cr_2O_3 - Al_2O_3 prepared using a conventional method, and possessing a cation concentration similar to that of the implanted specimen, (approximately 10 percent Cr).

The response of fracture stress of alumina to the implantation of ions was the subject of study conducted by T. Hioki et. al. [19]. This work included a pre-anneal of single crystal alpha-alumina specimens to eliminate mechanical damage prior to the implantation step. Nitrogen, and in a separate study, nickel ion doses from 10¹⁵ to approximately 10¹⁷ ions per square centimeter were implanted at 400 keV and a current density of approximately 3 microamps per square centimeter, while under vacuum.

Three-point bending strength tests which placed the implanted surfaces in tension were performed at room temperature on five specimens from each of the conditions of interest. Figure 5 is a plot of the flexural strength versus nitrogen ion dose. Increases of 100 to 300 x 10^6 Pascals $(10^6$ Pascals = 1 Mega-Pasacal, or 1 MPa) of the average flexural strength were measured with respect to an average initial value of 500 MPa for the unimplanted material. These increases were accompanied by a decrease for the ion dose greater than 10^{17} ions per square centimeter. Softening of the surface layer due to amorphization at the higher fluence has been suggested as being responsible for this decrease.

Further results of this work were summarized [20], and are

shown in Figure 6 as average relative flexural strengths versus ion dose for argon, nickel, and nitrogen ion species. Figure 6 shows that an increase in the flexural strength of the single crystal α -alumina of 37 percent was measured. Furthermore, it appears that heavier ions have a greater effect if implanted at lower fluences. It is suggested that the ion implantation strength improvements are related to the damage incurred by the substrate. This is consistent with the microstructural and mechanical property changes observed by McHargue et. al. [15].

Volume expansion in the surface region of α -alumina was reported by Krefft and EerNisse [21] to occur as a result of implantation-induced damage. Hioki et. al. [19] proposed that "a lateral surface compressive stress is induced" as a result of the restraint imposed by the undamaged substrate material upon the expanding implanted region. Additionally, each work suggests a compressive stress, determined to be approximately 10^3 MPa in the damaged surface, may be responsible for the improvement in surface strength.

For the nickel-implanted sapphire (α -alumina) specimens in the second study by Hioki, RBS-C data indicated extensive damage to the surface region [19]. Nickel concentration profiles for annealing temperatures of 800, 1000, and 1300 degrees celsius were compared to the as-implanted concentration. Figure 7 shows the significant change in the as-implanted profile to those of the 1000 and 1300 degrees celsius annealing results. A spinel compound NiAl₂O₄ was detected by x-ray diffraction for specimens that were annealed beyond 1000 degrees celsius. From optical and

scanning electron microscope inspections, a phase composition of $xNiAl_2O_4 + (1-x)Al_2O_3$ was suspected of forming a surface layer with a thickness of about 0.1 microns. Though recovery of the implantation-induced lattice damage was considerable, it was discovered that the flexural strength of the nickel-implanted specimens (Figure 6) did not experience recovery (return to the lower initial relative flexural strength of alumina of 1.0) upon annealing.

One possible mechanism for this strengthening, as givin by Hioki, is a residual surface compressive stress present after cooling the composite implanted/non-implanted layers. This stress results from the thermal expansion mismatch between the polycrystalline $NiAl_2O_3$ and the substrate.

Yttria stabilized zirconia (YSZ) was subjected to ion bombardment, heat treatment, and hardness and fracture toughness testing by K. O. Legg et. al. [23]. Single crystals of skull melted 9.4 mass percent YSZ were implanted with Al⁺ or Zr⁺ ions of doses ranging from 10¹⁶ to 4x10¹⁷ ions per square centimeter at 190 keV. A 25 percent improvement in Knoop microhardness values (0.5 Newton indent load) was reported for aluminum implanted samples annealed from 1300 to 1400 degrees celsius (Figure 8). This result was anticipated, for alumina was found to crystallize from the zirconia matrix, covering over 32 percent of the surface, and alumina is harder than cubic zirconia. However, thermal expansion mismatch was also considered as a source of increased hardness by generation of a compressive stress in the surface layer. It was reported that fracture toughness

increased only about 10 percent.

Significant improvements in the Al implanted specimens was realized after annealing the higher dose (4x10¹⁷ Al cm⁻²) specimens at 1400 degrees celsius and a heating rate of 75 degrees celsius per hour. What the authors referred to as a "nucleation controlled microstructure" (NCM) was formed with this schedule. Interlocking ribbons of the two phases possessed widths of approximately 0.5 microns. It was suggested that their presence was the mechanism responsible for a 40 percent increase in hardness and an improvement in fracture toughness of 70 percent. No significant changes were observed in the zirconia-implanted YSZ.

In review, mechanical properties of ceramic surfaces can be modified with the ion implantation of species that initiate the mechanisms attributed to the modifications. Microstructural changes and residual stresses induced by various methods have been shown to result in these modifications [24]. In general, these investigations found the changes in the atomic structure to be of two types. One was extensive lattice damage in the form of various defect types. The second was the presence of an additional nucleated phase formed upon annealing.

Lattice damage is expected to be present in any irradiated material. However, for work in which a second phase was not found, the irradiation damage was recovered following heat treatment, and a loss of the mechanical improvements measured prior to annealing were diminished. This strongly suggests that a second phase forming from the metastable region of implantation is

necessary in order to retain the improvements in mechanical properties established by the surface compressive stress.

Improvements in relative hardness values and fracture toughness for nickel-implanted ${\rm TiB_2}$ ranged from 70 to 100 percent and 40 to 80 percent, respectively. McHargue et. al. [15] also observed metastable interstitial solid solutions in alumina implanted with chromium. The result was a 50 percent increase in relative hardness. For both studies, thermal treatments reduced, but did not eliminte the mechanical property improvements.

Increases of 100 to 300 MPa of the average flexural strength of alumina containing implanted nitrogen ions were reported by Hioki et. al. [19]. The modifications were attributed to a compressive surface stress induced in the surface region by volume expansion differences between the implanted and unimplanted layers. For nitrogen-implanted alumina, the retention of flexural strength in spite of rigorous annealing environments was correlated to the thermal expansion mismatch of a dual phase spinel compound which had formed during low temperature anneals.

Finally, yttria stabilized zirconia was found to develop a "nucleation controlled microstructure" of "interlocking ribbons" [23] following aluminum implantation and annealing. The presence of this new microstructure was suspected to be responsible for a 40 percent increase in hardness and a fracture toughness increase of 70 percent. Several mechanisms have been suggested for the observations reviewed here. Though diverse, they share in common the end result of establishing a residual compressive stress in the subsurface region of a material. This condition is achieved

through volume expansion in the atomic structure of the original sub-surface region and, to be sustained, may require the formation of a second phase that will provide this increase in volume.

Solid solution-strengthening and defect interactions appear to lead to improvements in hardness, fracture toughness, and flexural strength in implanted crystalline layers [24]. Due to the relatively shallow depth of implantation, only trends in hardness measurements are reported for Vickers and Knoop hardness values. These results coupled with transmission electron micrographs of the altered material's structure provide insight into further understanding of the mechanisms for changes in mechanical properties of the surface.

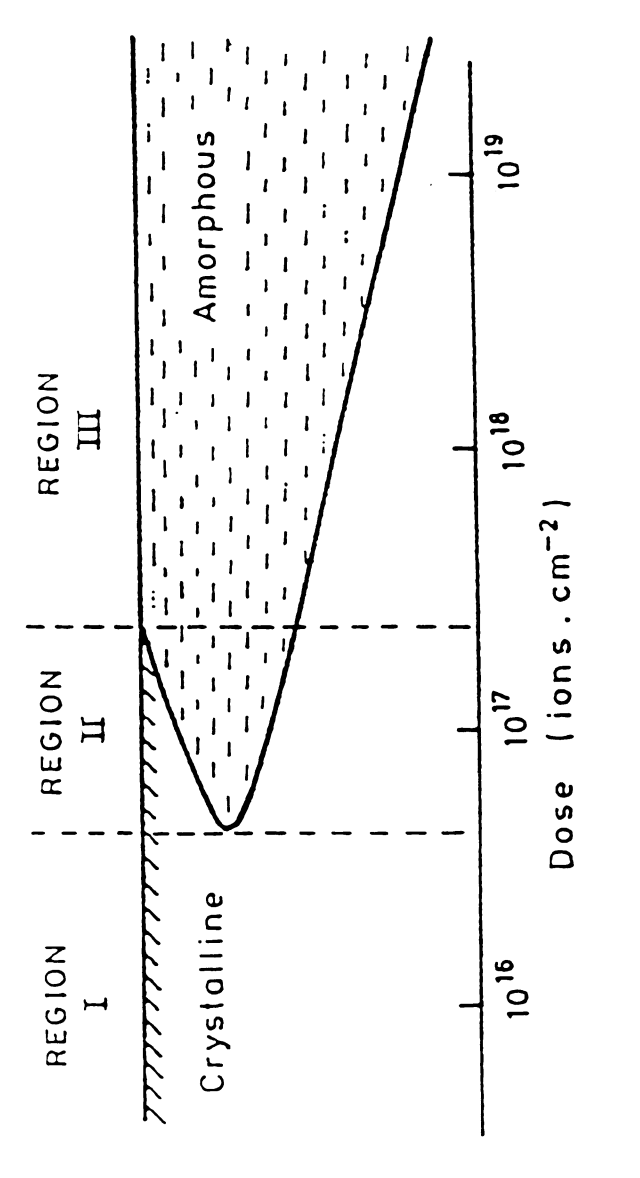
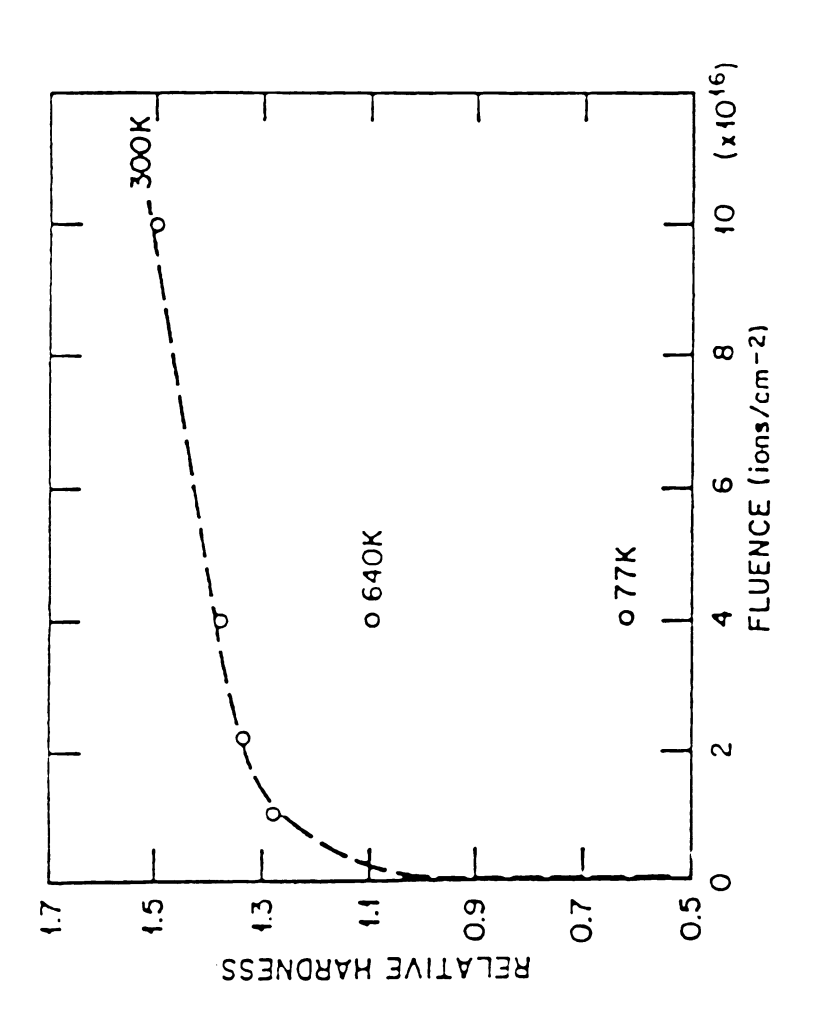


Figure 3. Effect of varying ion dose in ceramic [13].



Relative hardness of Cr-implanted alumina [18]. Figure 4.

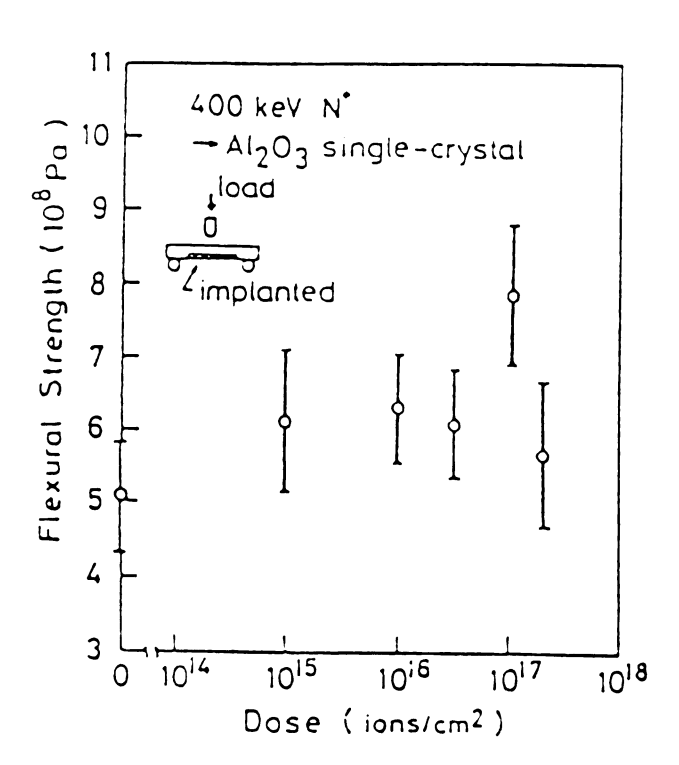


Figure 5. Flexural strength of implanted alumina [19].

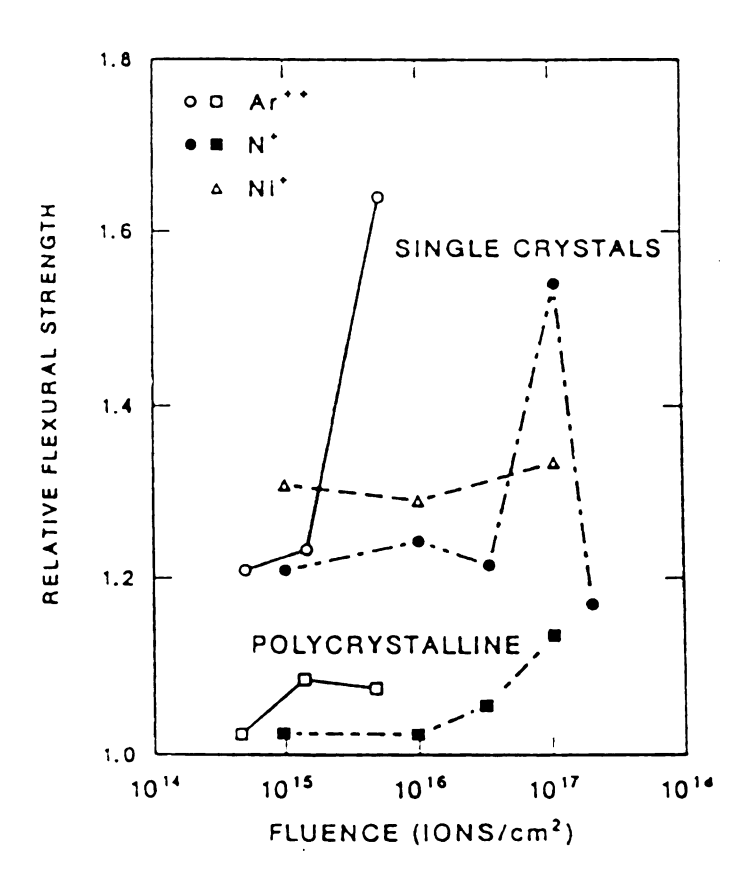


Figure 6. Flexural strength of alumina with ion species[20].

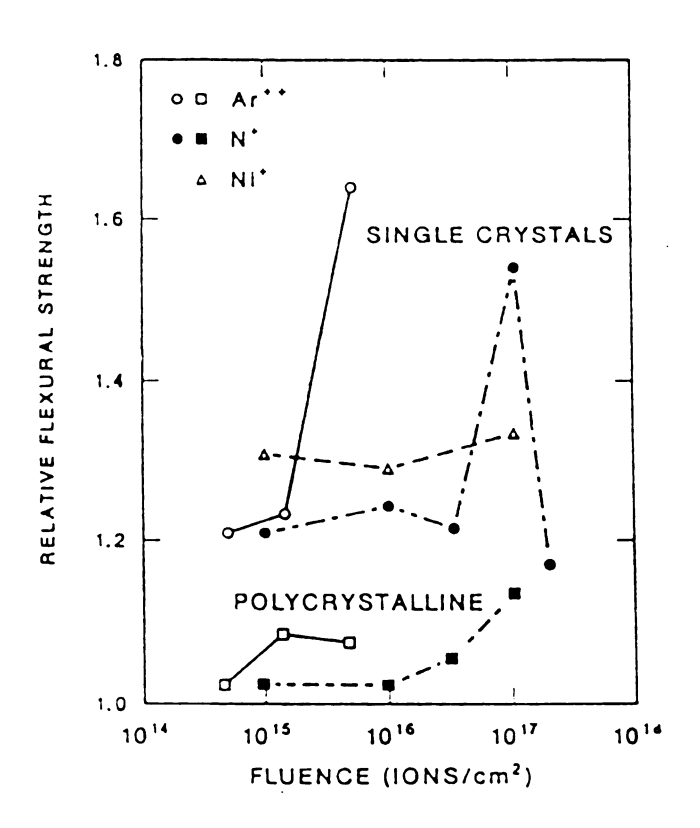


Figure 6. Flexural strength of alumina with ion species[20].

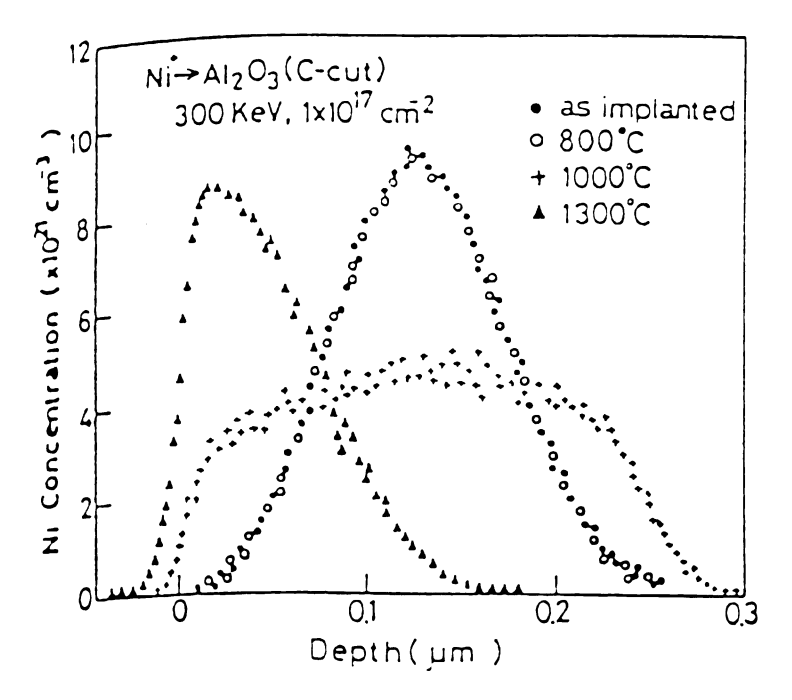


Figure 7. Nickel concentration in alumina [19].

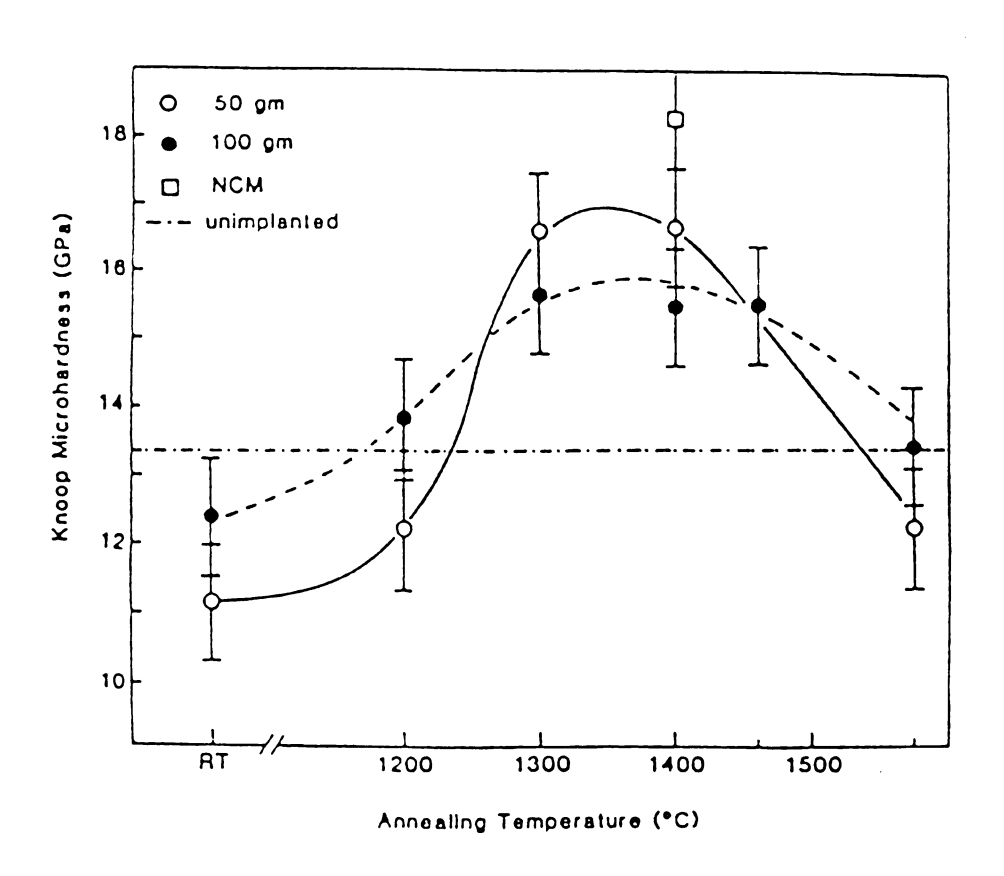


Figure 8. Knoop microhardness for YSZ [23].

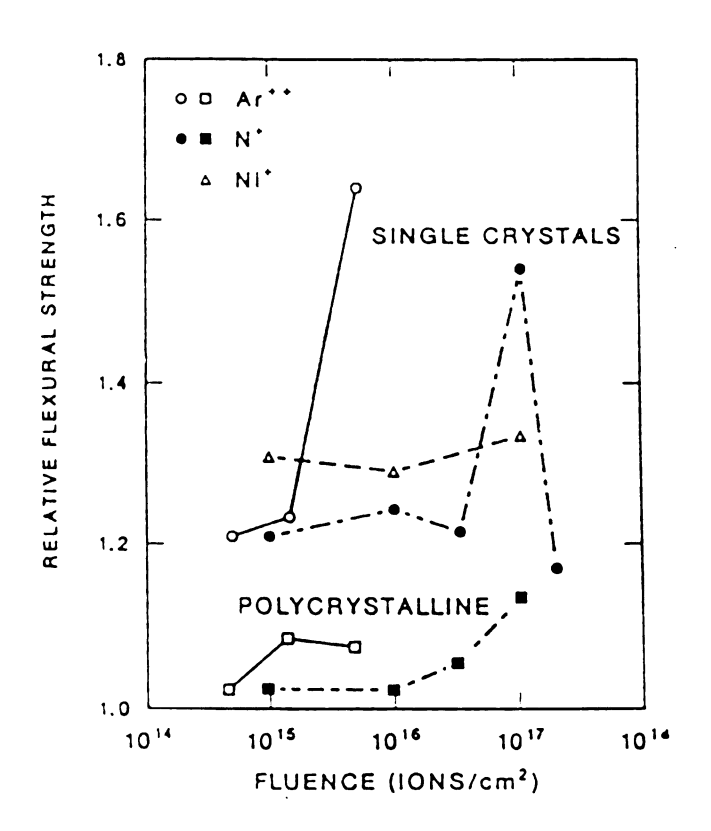


Figure 6. Flexural strength of alumina with ion species[20].

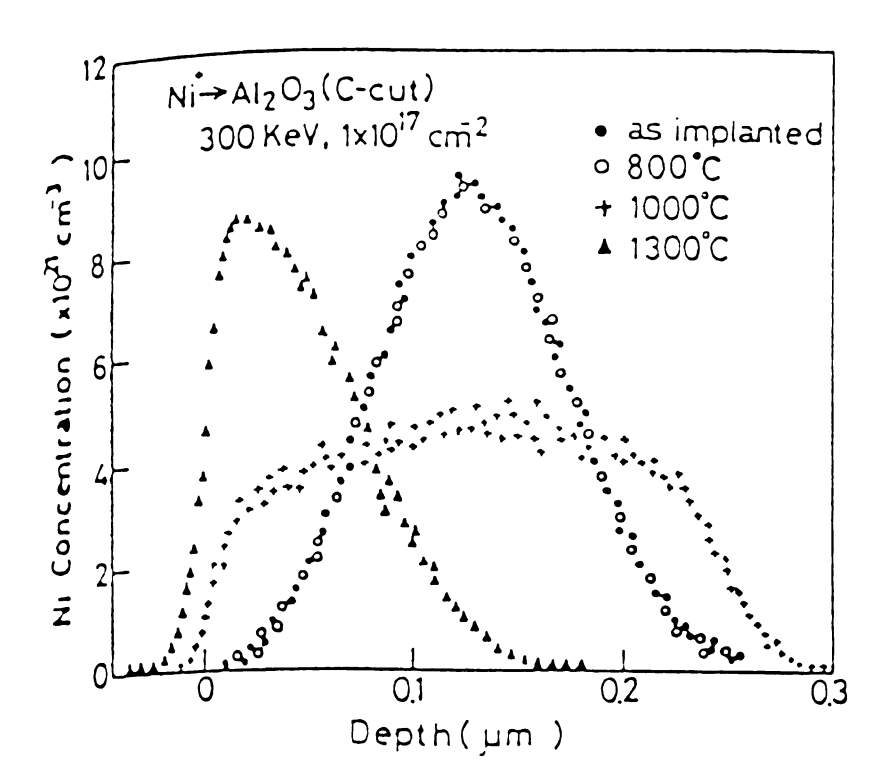


Figure 7. Nickel concentration in alumina [19].

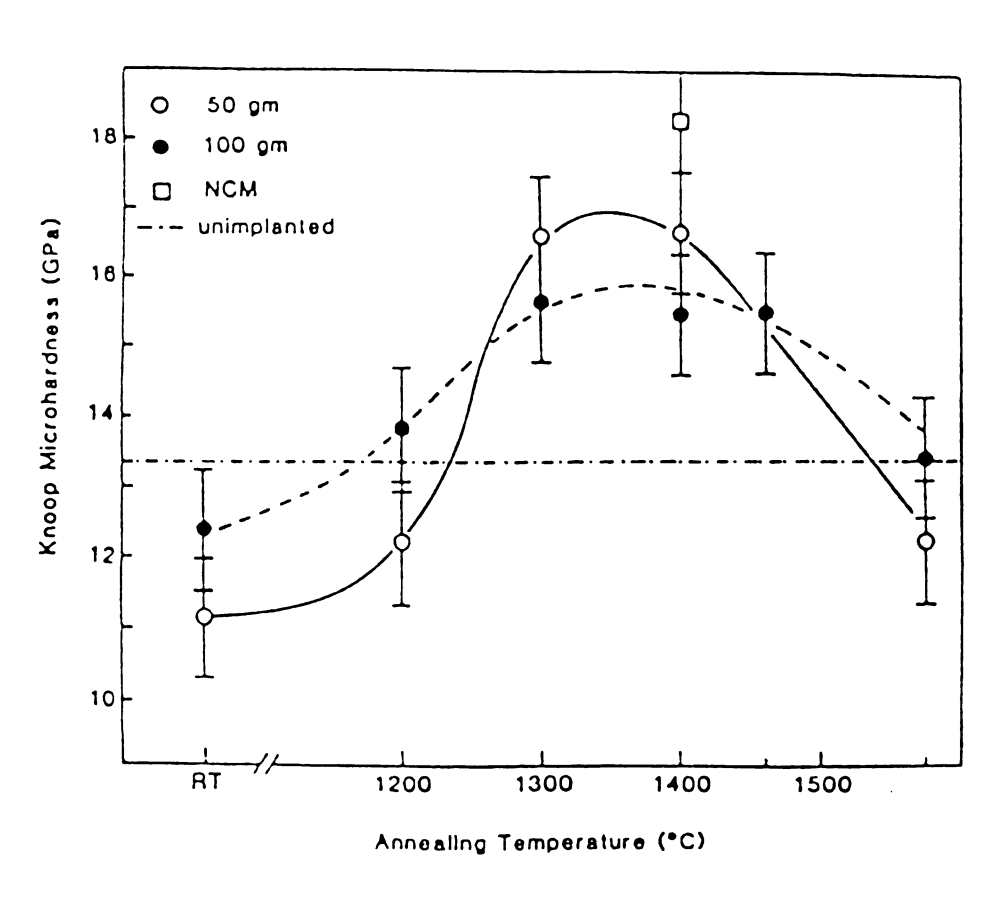


Figure 8. Knoop microhardness for YSZ [23].

1.4 ZINC SULFIDE

ZnS is a II-VI type ceramic that transmits infra-red wavelengths in the 8 to 14 micron wavelength range. The zinc-sulfer bond has 82 percent covalent character and an open atomic packing structure which is present due to the ratio of cation to anion diameters. Atomic diameters for zinc and sulfur are 2.7 and 2.0 angstroms, respectively (1 Angstrom = 10⁻¹⁰ meters). The principle structure types are face-centered cubic zincblende, referred to as sphalerite, and the high-temperature hexagonal form known as wurtzite. Their indices of refraction, according to one source [25], are 2.356 and 2.378 for wurtzite, and 2.368 for sphalerite, with no indication of wavelength of measure. A second reference reports the refractive indices for chemically-vapor deposited ZnS as 2.2520 at a wavelength of 4 microns and 2.2005 at 10 microns [26].

The melting point for sphalerite is estimated as 1830 degrees celsius although, under atmospheric pressure, ZnS volatilizes without decomposing at around 1000 degrees celsius. This is the temperature at which sphalerite has been observed to transform to wurtzite [27]. The Handbook of Chemistry and Physics [28] gives the lattice constant of sphalerite as a = 5.4093 angstroms and of wurtzite as a = 3.814 and c = 6.2576 angstroms. The structure of sphalerite is illustrated in Figure 9 [29].

Commercial zinc sulfide material is generally made from hot-pressed polycrystalline compacts which have been processed

from compounds of pure inorganic materials. These materials are placed in a mold which is then subjected to hydraulic pressure. Induction heating of the compact while under pressure raises the material temperature high enough for plastic deformation, without melting, to obtain a relatively pore-free optically dense product. Aggregates of small crystals form upon cooling and close packed grains with minimal grain boundaries result. The scattering of radiation by grain boundaries is present, but optical transmission is prevalent [30].

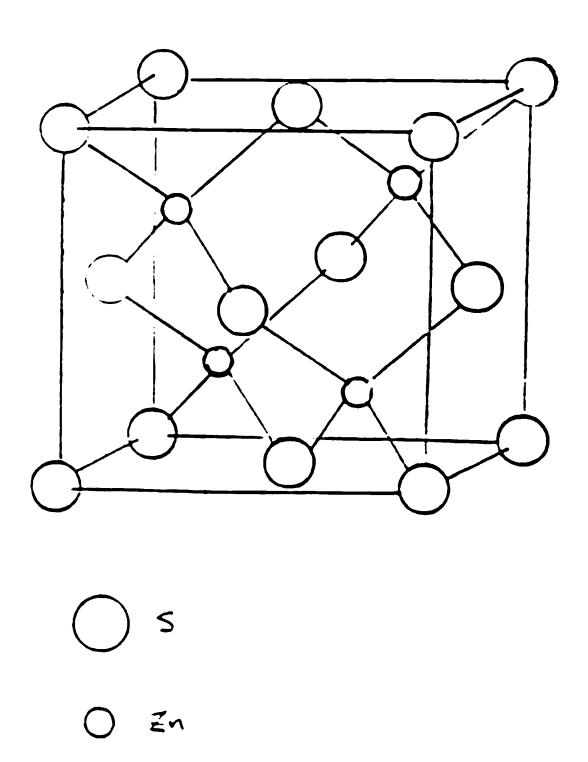


Figure 9. Atomic structure of zinc sulfide [29].

1.5 TRANSFORMATION TOUGHENING

Transformation toughening is a method of improving the ability for a material to resist fracturing due to the propagation of cracks within the material structure. All ceramics contain flaws within the subsurface region. The flaws usually originate during the processing of the ceramic and may exist as imperfections in the atomic structure, as mechanical abrasion at the surface, and in some cases, resulting from the difference in coefficient of thermal expansion between two phases of the material. According to Griffith [31] local stresses are concentrated at these flaws and the ceramic structure develops openings in the atomic planes to relieve these localized stresses. Such openings are referred to as "microcracks."

Fundamentally, a crack propagates through a material when the stress at the crack tip exerts a force that exceeds the fracture strength of the material. Transformation toughening, according to Evans [32], is regarded as a process whereby the crack tip is "shielded" from the stresses which induce this propagation; "shielded" referring to any method by which the crack tip stresses are reduced.

It is important to make the distinction between the stresses which induce initial microcrack formation, and those stresses which drive the pre-existing microcracks to propagate. The first originates within the material at inherent flaws which produce lattice strain and a corresponding stress concentrated

at these sites. In the mechanical equilibrium state, all stresses existing in the material matrix are lower than that required for crack propagation, thus the cracks are dormant. The second stress results from the external application of forces, ie. by physical impact with the surface or by loading. Since these sources are external, stress-induced transformation toughening is a useful method for improving the performance of materials which are more susceptible to damage at the surface than in the bulk.

The stress above which a displacive phase transformation is induced is the critical transformation stress, σ^C_T . Once this diffusionless transformation takes place, the volume of the new structure may be greater than or less than the initial phase, depending on the resulting structures atomic arrangement. Diffusionless refers to atomic movement which is less than one interatomic spacing. For transformation toughening to be imposed upon a material, the phase transformation must result in an increase in volume to the new phase. At the tip of a propagating crack, this volume increase creates a constraint upon the material matrix and compression of the atomic structure in the zone surrounding the crack tip. This lowers the strain and the corresponding stress to a level below that which is required for further propagation of the crack.

From the previous section, it was seen that establishing a residual surface compressive stress was the general principle for improving the surface mechanical properties of surface-sensitive ceramics. It was also seen that ion implantation which resulted in formation of a second phase in the

sub-surface region experienced sustained surface enhancement.

These improvements were attributed to a compressive stress established in the surface by the presence of the second phase.

It is likely, then, that the second phase structures were larger in volume than the original matrix.

If a stress-induced transformation toughener could be formed as a second phase in the surface of a ceramic by ion implantation, the resistance to damage from external loads would be greatly enhanced. Transformation to a phase with a larger volume upon impact by a load could prevent fracture of the ceramic surface. The following section introduces nickel sulfide as a transformation toughener with potential for this application

1.6 NICKEL SULFIDE AS A TRANSFORMATION TOUGHENER

Millerite is the naturally occurring nickel sulfide at room temperature and has a rhombohedral structure. It is also referred to as β -NiS, whereas α -NiS is the hexagonal high-temperature form, with the transition temperature reported to be at approximately 380 degrees celsius, and the melting point around 1000 degrees celsius [27]. The composition by weight is approximately 65 percent nickel and 34 percent sulfur for stoichiometric nickel sulfide. For α -NiS, the hexagonal lattice parameter ranges are a = 3.438 to 3.426 angstroms and c = 5.348 to 5.316 angstroms for the nickel-rich and sulfur rich compositions [27]. Figure 10 shows the nickel-sulfur equilibrium phase diagram.

Many materials have more than one crystallographic form in which they can exist, their chemical and mechanical stabilitydependent on factors such as temperature, pressure, and stoichiometry. Pure zirconia, for example, transforms from the high-temperature cubic phase to a tetragonal form at approximately 2400 degrees celsius, then to monoclinic at 950 degrees celsius. A significant increase in volume occurs primarily for the second of these transitions and results in the ceramic body crumbling into powder, i.e., it self-destructs [34]. Typically, additives to zirconia result in stability of this tetragonal phase. The advantage this material then offers lies in the fact that the phase transformation may be induced by an externally applied stress. The stress at the tip of an advancing crack is

reduced by the positive change in volume that occurs upon transformation, which results in a residual compressive stress. The crack is "arrested" which results in improved toughness.

Similar volume changes for nickel sulfide were reported in work by M.V. Swain [33] which involved the study of microcracking in glass. The local regions of cracking observed in the glass were identified to be in close proximity to inclusions of nickel sulfide. A volume expansion of approximately 4 percent was observed to accompany the microcracking. This change in volume was attributed to the α -to- β phase transformation of α -NiS, metastably retained in the quench-cooled glass. Transformation was initiated during a subsequent heating of the glass as it approached the transformation temperature of approximately 380 degrees celsius.

W. M. Kriven has explored several materials with potential as transformation toughening alternatives to zirconia based upon their crystallograpy and empirical results [34]. The criteria recognized by Kriven for a transformation to be considered "martensitic" (diffusionless) were that the particles undergo both shear and volumetric strains. This translates to the distortion of the material structure without breaking the atomic bonds. This is a "displacive" transformation and is usually accompanied by a change in volume due to the deformation of the lattice. Initiated by Swain's work, research conducted by Kriven led to the suggestion of NiS as a metastable stress-induced transformation toughener.

Following Kriven's supposition, work was initiated to

evaluate the potential of introducing α -NiS as a stress-induced transformation toughener in the surface of ZnS by ion implantation and thermal treatment. The final system proposed in this work is one in which nickel ions, implanted into zinc-sulfide, form bonds with sulfur and precipitate as nickel-sulfide. The metastable phase of α -NiS is desired as a fine distribution of particles in the near-surface region of ZnS bulk material, a ceramic known to be surface sensitive. When a stress is applied to the surface, the associated shear and volumetric strains would then induce the displacive transformation of α -NiS particles to β -NiS. This transformation results in a positive change in volume, therefore, the stresses at the microcracks which exist within the ZnS subsurface region would be reduced and the cracks would not propagate. Following one impact of the surface, the subsurface region in which the transformations took place would retain the residual compressive stress of the volume increase. Ceramics tend to fail in tension, thus, a surface stress of a compressive nature would further guard against mechanical failure due to crack propagation in this region of the ZnS material.

Zinc sulfide has been ion implanted with nickel-beam ions of a fluence of $10^{17}~\rm ions/cm^2$ at 200 keV. The goal was to form metastable $\alpha\textsc{-NiS}$ precipitates in the ZnS surface region. Annealing of the modified material was conducted towards this end. Diffraction patterns of the specimens generated by transmission electron microscopy were analyzed for evidence of nickel sulfide precipitates. Additionally, hardness of the zinc sulfide before and after implantation and annealing was determined

to investigate the effects on the mechanical properties.

Electron diffraction patterns did reveal the presence of a second phase of very fine particles in the near-surface region of the irradiated ZnS. Indexing of the pattern provided evidence that α -NiS precipitants were present in the material. Increases in hardness were also found for nickel-irradiated material that was followed by heat treatment. Chapter 2 provides the detail of the experimental procedures and Chapters 3 and 4 present the results and conclusions, respectively.

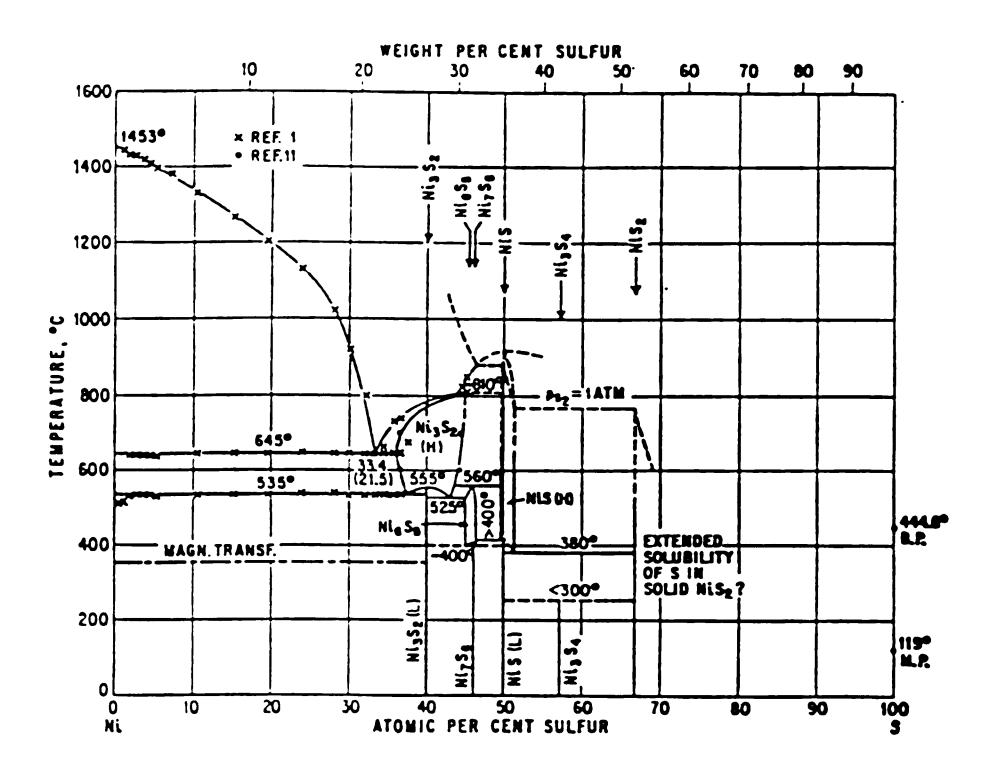


Figure 10. Nickel-sulfur phase diagram [27].

CHAPTER 2 EXPERIMENTAL PROCEDURE

This chapter describes the methods used for specimen preparation of zinc sulfide for ion implantation. Specimens were prepare for both TEM analyses and surface hardness testing. The role of X-ray diffraction for improving the accuracy of an internal standard is discussed as well as use of this standard in the work completed by transmission electron microscopy. TEM patterns were generated in the selected-area diffraction mode, along with bright- and dark-field images of the sub-surface region in the nickel-irradiated ZnS. Indexing of the diffraction patterns is discussed briefly. Vicker's hardness testing was conducted to measure the change in mechanical properties for the irradiated samples and scanning electron microscopy provided a close look at the surface grain morphology. X-ray photoelectron spectroscopy was conducted on experimental and control specimens to investigate the presence of various constituents.

2.1 SPECIMEN PREPARATION

Two geometries of zinc sulfide ceramic material were prepared for TEM analysis and hardness testing, respectively. A core saw had been used prior to this work to cut 15 millimeter "plugs" from a disc of zinc sulfide (Irtran II, Eastman Kodak Co., Rochester, NY), approximately 25 centimeters in diameter. Four of these were dedicated to ion implantation and four were retained as the

control samples for the surface hardness evaluation.

Once the plugs were removed, the remaining scrap material shapes resembled a parallelpiped with dimensions of approximately 25 centimeters in length and 5 centimeters width and height. An initial polishing test was conducted to determine the resistance of the material to removal by a rough medium. It was found that the ZnS could be easily shaped and formed by hand polishing with 400 grit polishing paper.

The method for obtaining the desired TEM specimen geometry was developed for the ZnS material with the parallelpiped shape. Though the cross-sectional geometry of these were not circular, as is typical for metallic TEM specimens, it was concluded that a 3 millimeter diagonal of the parallelpiped cross-section would be sufficient for securing a specimen in a TEM holder. After further work it was found that the corners of this shape experienced stress concentrations too high for reasonable handleability of the ZnS ceramic material. These specimens fractured during transfer operations using TEM tweezers.

A revised shape was obtained by carefully grinding the material by hand on 600 grit polishing paper. The finer grit was used to remove the corners and reduce the surface roughness to achieve an approximately cylindrical shape, thereby decreasing the possibility of damage to the material. Distilled water dispensed from a plastic squeeze bottle was used for a coolant and to carry particles away from the grinding paper.

2.1.1 Cutting

A diamond blade variable speed saw was used to cut specimens to their initial TEM thickness. Figure 11 illustrates the arrangement for slicing. Zinc sulfide was mounted to a clean glass slide with thermoplast, a heat setting polymer-resin commercially available (Beuhler) as a solid "stick" at room temperature. Heating the slide with a Beuhler hot plate to approximately 170 degrees celsius, and applying thermoplast to the slide surface resulted in a small pool of thermoplast upon which a specimen was located. Removing the heat source solidified the resin, thus adhering the cylinder of zinc sulfide to the slide. The glass slide was then mounted in the cutting saw clamp. This arrangement, prevented distortion or damage to the specimen, and made available the entire specimen bulk for sample preparation. Approximately forty samples were cut from this arrangement, ranging in thickness from 1000 to 700 microns. All transfer of the specimens in this procedure was performed with nonmagnetic TEM tweezers, size 3c (A. Dumont & Fils, Switzerland).

Following the removal of the specimens by reheating the glass slide, the specimens were successively cleaned ultrasonically in warm water with a mild surfactant, acetone, and ethyl alcohol to remove contaminants such as cutting oil, thermoplast, and ZnS residue. Care was exercised to expose the specimens to ultrasonic energy transmitted only through the fluid medium (water) to minimize exposure to the transducer vibrations. This was accomplished by suspending a glass beaker of water and the samples into the bath, making no contact with the reservoir surfaces.

2.1.2 Polishing

A polishing block was prepared to aid the polishing of the ZnS ceramic specimens. A cylinder of aluminum alloy, approximately 3 centimeters in diameter and 2 centimeters in height, was polished on 320, 400, and 600 grit polishing paper, successively. To ensure uniformity in the surface of the polishing block, the polishing papers were attached to a photographic plate approximately 30 centimeters square. A light microscope at 50X was used to inspect the polishing progress.

TEM specimens were then mounted to the polishing block with cryanoacrylate (Super Glue Corporation, Hollis, NY) in groups of five. Care was exercised in arranging the specimens on the block to promote an equal distribution of pressure throughout the hand polishing steps. The glue was cured for one hour at room temperature.

The polishing procedure included six different polishing media. First, the specimens were coarse-polished on 600 grit paper attached to a photographic plate. This was done until "rocking" of the block-specimen arrangement was eliminated, to assure uniform contact of each specimen. Preparation of the surfaces continued with a fine, 1200 grit polishing paper. This, too, was secured to a photographic plate.

The last four polishing steps were performed on motor driven polishing wheels. The "laps" or cloths used on the wheels were either nylon or "Micromet" polishing discs; both were backed with adhesive. The media used on these wheels were 5 micron and 1 micron polishing alumina (Al_2O_3) on the nylon discs and 0.3 micron

alumina and 0.05 micron Buehler deagglomerated alumina on the "Micromet" discs. Duration of polishing for each grade of polishing media was approximately five minutes. After attaching the zinc sulfide specimens to the aluminum block, and between each polishing step, the samples were cleaned using the following sequence:

*	water rinse	2	mins
*	distilled water rinse	30	secs
*	distilled water ultrasonic	20	secs
*	ethyl alcohol ultrasonic	20	secs

The appearance of the surfaces of the zinc sulfide specimens changed with the polishing procedure from opaque, to translucent, then to transparent with a slight hue of greenish-yellow, attributed to normal scattering by inherent defects.

Upon completion of polishing one side, the specimens were removed from the aluminum block by soaking in acetone for 2.5 hours, then remounted to permit a rough polish of the other surfaces using 1200 grit polishing paper. These surfaces would be prepared further with dimple grinding and ion milling, following the implantation process, thus, the 1200 grit paper alone provided the necessary finishes. This was followed by the procedure described above for removal, then cleaning, and storage in a TEM specimen holder. Once both sides of the specimens were polished and approached TEM geometry requirements, they were divided into two groups of twenty. One group was selected as the control,

whil

impl

2.1.

and be

chi

zir Fig

io.

'nу

10

à;

8]

a a

1: Wa

.

1

\$ 6

while the other specimens were prepared for exposure to the ion implantation processing.

2.1.3 Mounting

An aluminum plate with thickness of approximately 0.5 inch and measuring 6 inches by 6.5 inches, was designed and machined to be used as the specimen's mount that would be attached to the chill block in the ion implantation chamber. This plate and the zinc sulfide sample arrangements on the plate are illustrated in Figure 12. The plate was cleaned with a water-detergent mixture followed by iso-propyl alcohol. To remove any corrosion products remaining on the aluminum surface, the plate was soaked in hydrofluoric acid for 3 minutes. Rubber gloves were used for further handling and transfer of the plate following the acid treatment to minimize contamination.

The twenty TEM specimens selected for ion bombardment were attached to the aluminum plate with electrical and heat-conductive silver paint in the arrangement shown in Figure 12. The four ZnS discs 15 millimeters in diameter and 3 millimeters thick were also attached. These were used for hardness and annealing experiments. The discs and cluster of TEM specimens were contained within a 2 inch diameter centrally located on the aluminum plate. The plate was heated in a low-temperature oven for 1 hour at approximately 90 degrees farenheit to aid in the drying of the silver paint.

After cooling, the plate was placed in a single "Ziploc" polyethelene bag which was filled with liquid-nitrogen vapor and sealed. A second bag containing several dessicator capsules and

surrounding the first bag was similarly filled and sealed. A corrugated cardboard structure was designed to trap the liquid-nitrogen vapor in a "pocket" over the specimens. Additional packaging materials were used to protect the aluminum plate and ZnS specimens during shipping to the ion beam facility.

2.1.4 Ion Implantation

The specimens prepared for ion treatment were shipped to Implant Sciences Corporation in Danvers, MA. Nickel ions were implanted into the ZnS substrate at a dose of $1 \times 10^{17} \, \text{ions/cm}^2$ with 200 keV of energy and a beam current of 165×10^{-6} amps. The angle between the beam direction and horizontal was 90 degrees. Freon cooling temperature was minus 45 degrees celsius and freon cooling pressure was 9 pounds per square inch (psi). The beam aperture was open 100 percent and the inert chamber gas used during the implant was chlorine at 0.85 psi.

The surface of the implanted specimens as-received appeared to be dark purple or scarlet in color. A similar but lighter appearance was observed on the 2 inch diameter of the aluminum plate. One of the TEM specimens was lighter in color and it appeared as though partial masking of the beam occurred, for this sample was located at the edge of the beam diameter. It could be assumed that this specimen received a dose of nickel lower than 10^{17} ions/cm².

Soaking in an acetone bath dissolved the silver paint and permitted removal of the specimens from the aluminum base.

Ultrasonic cleaning in acetone, then absolute ethanol, preceded

storage of the TEM specimens in a TEM "grid-storage" container.

The 15 millimeter discs were stored in plastic laboratory

containers each filled with a layer of dessicant, then cotton, and

laboratory tissue paper.

2.1.5 Dimple Grinding

Further specimen preparation steps were necessary following ion implantation to make TEM specimens of the 3 millimeter discs of nickel-implanted zinc sulfide. Two separate methods typically used for ceramic TEM specimen preparation were attempted. One utilized dimple grinding followed by ion milling to physically thin the material such that an electron transparent region exists adjacent to a perforation edge. The other involved chemistry following dimple grinding which resulted in a thinning effect by etching.

Dimple grinding is typically used to prepare specimens for ion milling. The grinding provides material removal rates far exeeding those achieved with ion milling, thus reducing the duration necessary for the latter process which is both, more precise in material removal (atomic effect), and more expensive. The "dimple" or bowl-shaped contour of a previously flat specimen surface is achieved by grinding material away from the specimen with a fine diamond paste slurry carried on a brass wheel. The specimen rests on a rotating stage during grinding, thus, forming a dimple in the specimen with the lowest (thinnest) point to be the target for ion milling.

The nickel-irradiated zinc sulfide specimens were

approximately 600 microns thick at this step of the preparation.

Typically, a specimen thickness conducive to dimple grinding is between 50 to 100 microns. Therefore, prior to grinding, final thinning and perforation, the bulk of the back side of each of the irradiated ZnS specimens was reduced to yield thicknesses of approximately 80 microns.

This was accomplished with a Gatan Disc Grinder 623, a handheld polishing unit consisting of a 0.375 inch diameter cylindrical specimen mount centrally inserted into a 3 inch diameter polishing base (see Figure 13). A rotating dial (control knob in Figure 13) with a scale mounted on top of the base indicates the thickness of the specimen attached (with melted wax) to the specimen mount. The specimen surface is polished by rotating the dial which lowers this surface just below the polishing unit's face. This permits specimen contact to abrasive paper affixed to a glass plate. The abrasive paper used was Buehler 1200 grit polishing paper.

A top view of the Gatan Dimple Grinder-Model 656 is shown in Figure 14 (Gatan, Inc. 6678 Owens Dr. Pleasanton, CA 94566). Once the desired thickness is achieved, the specimen mount which was used in the hand polisher is placed in a metal ring on the specimen turntable platform of the dimple grinder. The grinding wheel depth is adjusted with the micrometer drive, and the dial indicator shows the thickness of the material removed in microns. The speed of the turntable and the counterweight can be adjusted; optimum settings must be determined empirically. The speed control was set at 5 and the counterweight used was 1 gram for the

zinc sulfide specimens.

Initially, a standard specimen mount and a 15 millimeter phosphor-bronze grinding wheel were used to attempt preparing TEM specimens for ion milling. These are illustrated in Figure 15, along with the smaller 10 millimeter wheel and modified mount. The larger wheel removed too much of the specimen near the perimeter for adequate strength to be retained. This resulted in specimens fracturing during handling with either TEM tweezers or with vacuum tweezers. The smaller wheel formed dimples with diameters significantly smaller than the 3 millimeter diameter of the specimens, thus retaining bulk material at the perimeter. Vacuum tweezers were used successfully in the handling and transfer of these fragile samples.

2.1.6 Chemical Thinning

According to P. Worthington, [36] zinc sulfide can be thinned by a "specially developed chemical thinning method."

Worthington's success with thinning zinc sulfide with chemical flow was made possible by the manufacture of a glass enclosure that permitted the flow of thinning chemicals across the ZnS, the observation of the material removal progress with a backilluminating microscope, and a distilled water wash system to stop the process immediately upon observing a perforation.

For the present work, a South Bay Model 550C Single-Jet
Thinning Instrument (South Bay Technology inc., 5209 Tyler Avenue,
Temple City, CA) was used to introduce the thinning solution to
the zinc sulfide specimen surface. This instrument consists

of a chemically inert plastic platform shaped to form a round base approximately 8 inches in diameter. Molded within this plastic are housings for the pump and motor, inlet and outlet ports for directing the chemical, and a specimen stage which included a splash guard and manification lens for viewing the process. The platform is grooved on the underside. A glass cylinder fits into this gasket-lined groove and the thinning solution is poured into and pumped from this reservoir.

The solution was prepared by pouring 900 milliliters of hydrogen chloride into a 1500 milliliter Corning glass beaker and adding 9 grams of chromium trioxide (CrO₃). This was stirred with a glass stirring rod for approximately one minute, then poured into the jet thinner reservoir. To protect the metallic components of the jet thinner, pressurized air from a chemical hood source was run through a 1/4 inch flexible rubber hose to an inlet in the thinning instrument's platform. The system beginning at the inlet permits the pressurized air to form an envelope between the chemically sensitive components in the jet thinner platform and the chemical stored in the reservoir below.

Non-irradiated zinc sulfide specimens were used to test the abilities of this technique. For irradiated specimens to be thinned with this method, the irradiated surface must be protected from the chemical. To test this, one surface of a non-irradiated specimen was coated with Miccroshield lacquer using a fine oil paint brush. The specimen to be thinned was then located on the pedestal of a sample holder with a 2.3 millimeter hole to minimize the exposure of the chemical to the specimen surface. A

polyethylene diaphragm with a centered hole was placed over the specimen and held into a groove with a rubber ring.

The automatic shutoff feature of the Model 550C was not utilized. Infrared optics are used for the detection of perforation in thinned samples. Being transparent to infrared radiation, specimen perforation was monitored visually with a hand held 10x magnifier and an Olympus Transmission & Back-illuminating optical microscope. The magnifier built into the splash guard, which surrounds the pedestal and jet nozzle, was unable to provide a view of the specimen due to the hydrogen chloride vapor.

A second chemical solution consisting of CrO_3 and H_2O was used with the jet thinner to attempt making TEM specimens with the zinc sulfide. A 3 x 3 disPO weigh boat was tared on a Mettler Type H15 single pan balance (Mettler Instrument Corp. Hightstown, New Jersery). CrO_3 was placed in the boat with a stainless steel spatula until 80 grams were measured. This was poured from the boat into a polypropylene bottle with a screw top. A 250 milliliter glass beaker was filled to 100 milliliters with H_2O and stirred with a 2 inch stir bar and a Cole-Parmer Model 4812 Magnetic 6 x 6 inch Stirrer with Hot Plate. The chromium trioxide was dissolved into the water by stirring the solution, heated to 85 degrees celsius, for 2 minutes. This solution was also used in the jet thinner.

A nickel-irradiated specimen was polished by hand to a thickness of 105 microns, then dimpled to yield a minimum thickness of 20 microns. The polished side was coated with protective lacquer and the specimen was loaded for jet thinning

with the CrO₃/HCl chemical solution. Using the jet thinner autodispense timer, inspections were made at 10 second intervals. After 4 minutes of thinning, it was determined that perforation had occurred much earlier, but was obscured by the red Miccrocoat lacquer. This perforation resulted in a specimen too thick for TEM observations. Table 1 summarizes the chemical thinning procedures and observations.

TABLE 1. Chemical thinning durations and observations.

SOLUTION	THINNING TIME	OBSERVATIONS
CrO ₃ /H ₂ O	15 sec	surface slightly etched
"		no change on lacquer
п	1 min	no change
п	5 min	<pre>preferential material removal (appears "eroded")</pre>
н	10 min	little change
"	60 min	<pre>preferential material removal approx 10 microns</pre>
CrO ₃ /HCl	1 min	slightly etched
"	10 min	dimple depression
II	17 min	deeper depression
n	30 min	further erosion
11	60 min	bowl shape evident

Ç. ξ. â٦ Ì:

:

•

2.1.7 ION MILLING

Final perforation of the polished and dimpled nickelimplanted zinc sulfide specimens was accomplished with ion milling. This was done with a Maxmill Ion Gas Milling System, Model 306/TM 170 (VCR Group Inc. San Francisco). The system includes a liquid nitrogen cooled specimen stage and an automatic perforation detector with variable sensitivity. The minimum beam angle to the horizontal specimen plane that could be set for this system was 18 degrees. An angle less than this would result in detector-beam path interference from the cooling stage. Beam angles of 18 and 30 degrees were used for ion milling the zinc sulfide specimens. The argon back-filled chamber maintained a vacuum of 2×10^{-5} torr. The liquid nitrogen stage temperature average was approximatley minus 50 degrees celsius. An energy of 5 kilo-electron volts and gun current of 1.5 milliamps was typical for the ion milling process. The speed of rotation of the stage was fixed at approximately one-half revolution per minute.

Following ion milling the chamber remained undisturbed to permit returning to room temperature without the aid of the nitrogen gas warming mode. The objective was to minimize the possibility for thermal shock to occur in the specimen. This ambient warming averaged approximately 7 hours in duration.

Several arrangments were used to mount the specimens in the ion milling chamber. The first held the specimen between two washers of aluminum which were placed in the recess of a geardriven brass disc. A brass retainer which held the aluminum and

specimen in place was secured with three screws which threaded into the bottom brass disc After ion milling, black residue was apparent on the aluminum specimen washers. This may have been deposited by the ionization of contaminants either existing in the chamber, or carried into the chamber by the zinc sulfide or aluminum materials, or both.

Platinum washers with central holes 2.3 millimeters in diameter replaced the aluminum washers which are not as durable to ion milling. The standard arrangement above was modified to secure the specimens below the 2.3 millimeter hole in the absence of stress by compression between two washers. This was accomplished by using cyanoacrylate to adhere the specimen to the bottom side of the washer with the non-irradiated specimen surface below the hole and exposed to the ion beam for milling. This arrangement is shown in Figure 16.

Attempts to use the auto-terminator were unsuccessful due to instrumentation instability. Many attempts were made to stabilize the detector with the ion beam at varying levels of sensitivity and gun voltage. This may have been due to excessive use of the mill with many different materials resulting in a high rate of gun contamination.

Following the preparation of a potentially electron-transparent specimen, the specimen was placed in a 50x50 coppermesh Gilder folding grid, (Ted Pella, Inc. PO Box 2318, Redding, CA, Catalog No. GD 50/50) for TEM observation. This procedure was observed with the aid of an Olympus Type JM back-reflection microscope (Olympus Optical Co, Ltd.) and Dupont Type 3c tem

tweezers. An electric vacuum-tweezers apparatus with a one millimeter nozzle was used to transport the specimens from a glass slide to the Olympus microscope stage for enclosure in the coppermesh TEM grid. Pella TEM specimen holders were used to store the specimens, which were then stored in a dessicating cabinet.

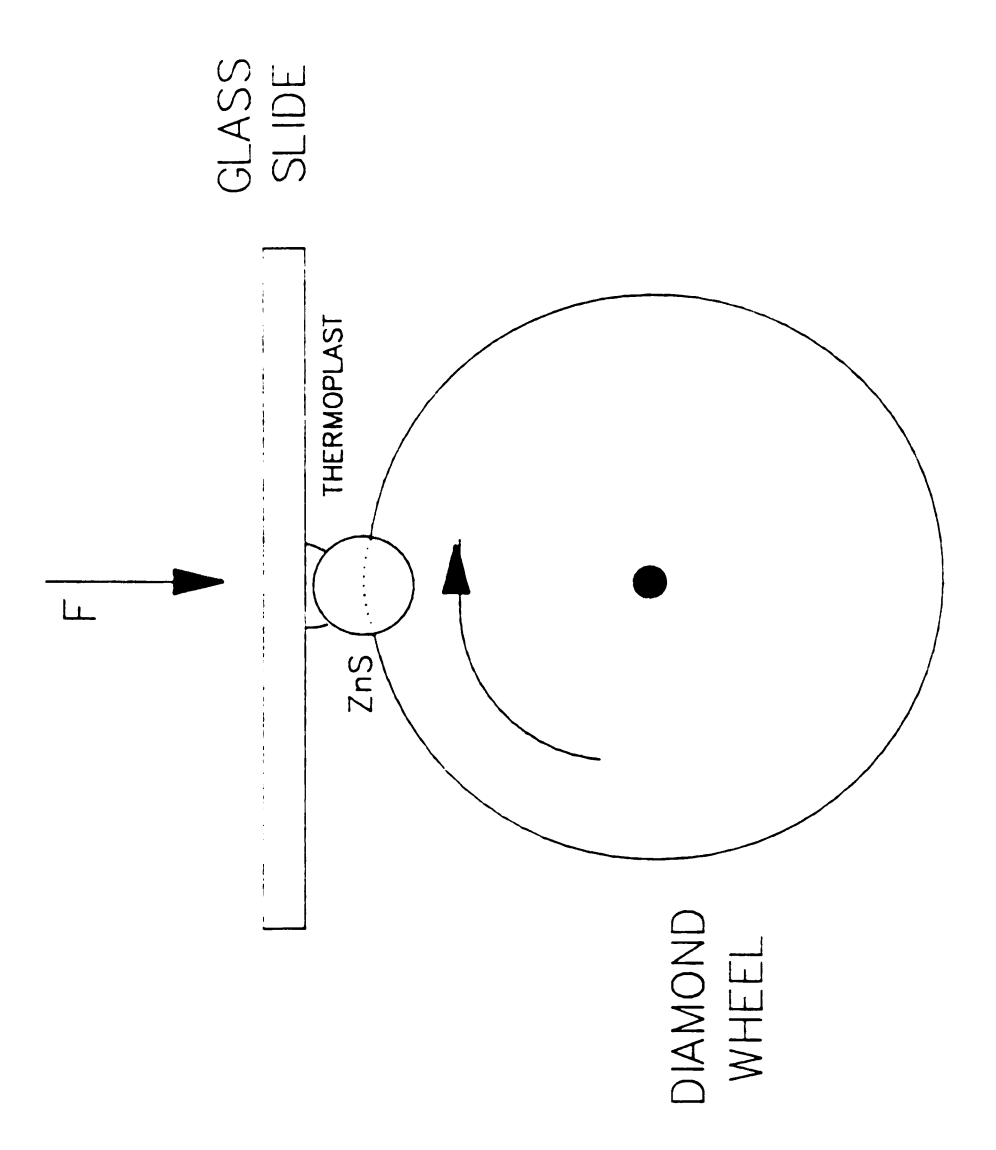


Figure 11. Slicing ZnS for TEM specimens.

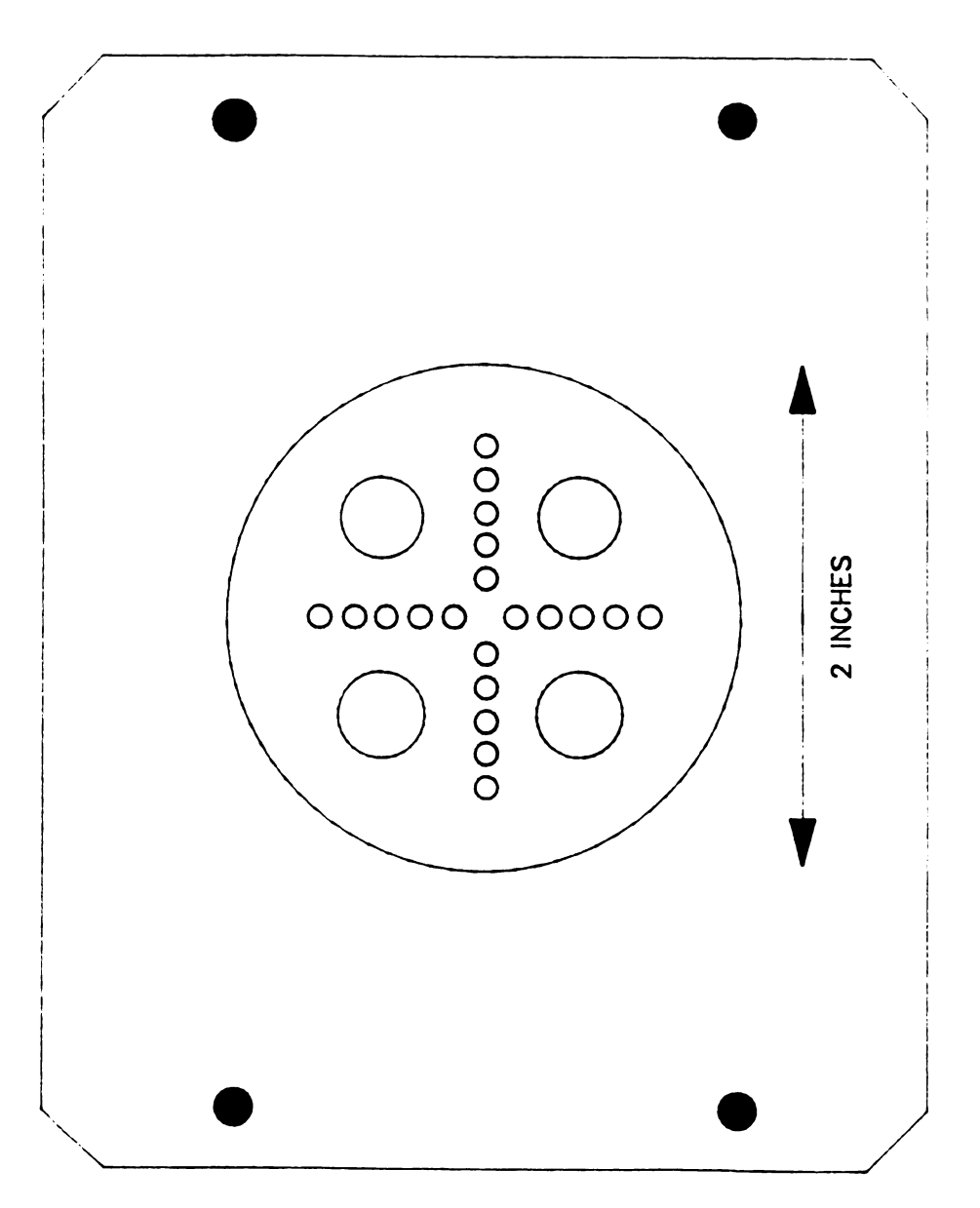


Figure 12. ZnS specimen arrangement for irradiation.

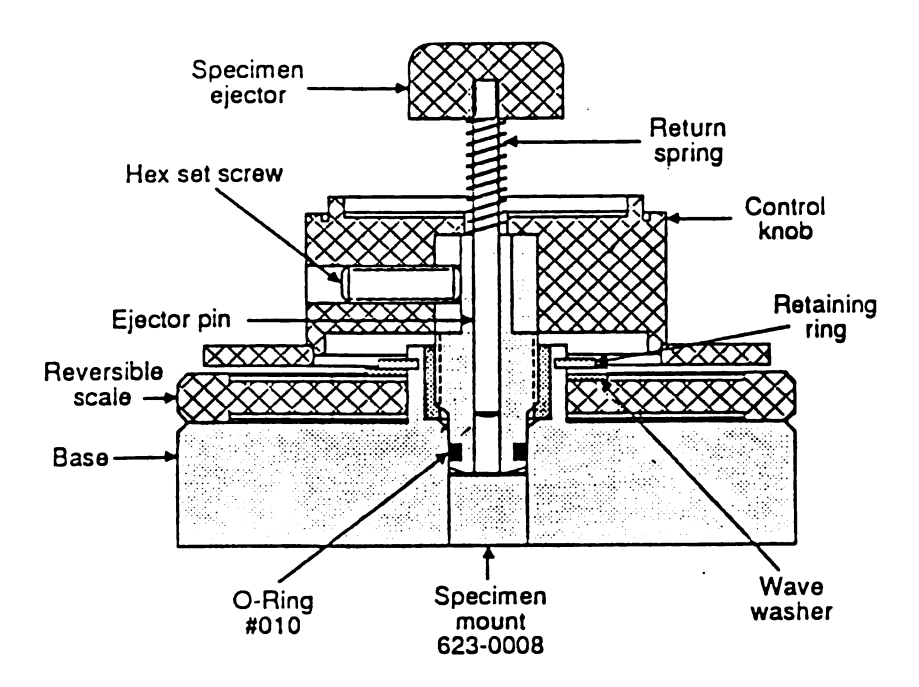


Figure 13. Gatan hand-held disc grinder[35].

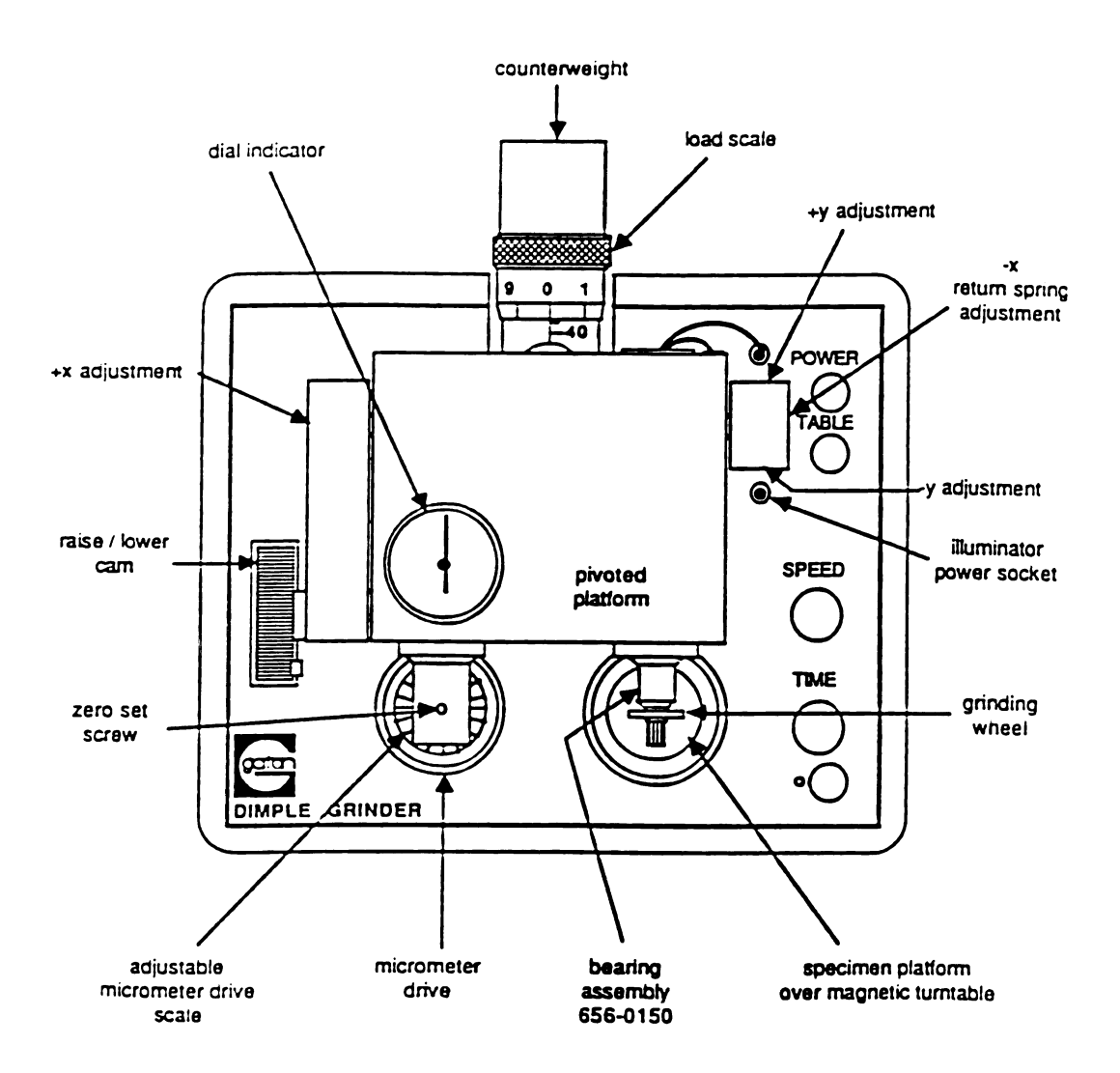
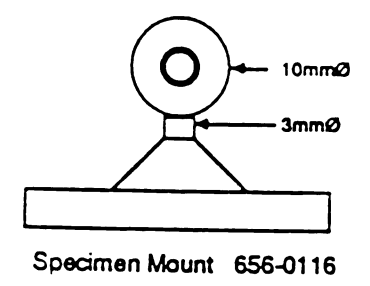


Figure 14. Gatan Model 656 Dimple Grinder (top view)[35].



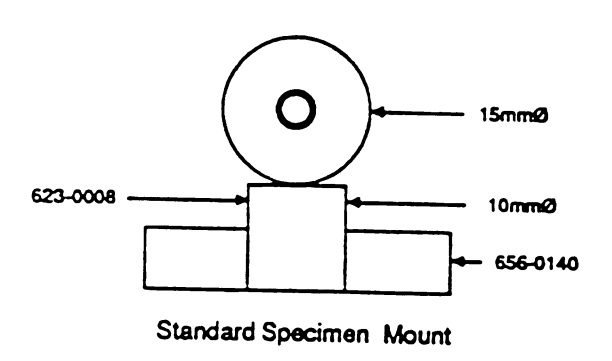


Figure 15. Dimple grinder specimen mounts[35].

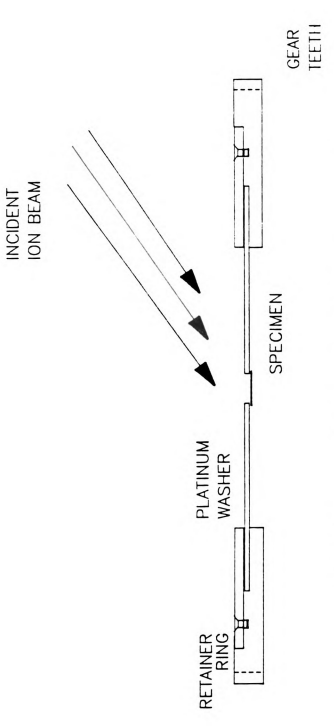


Figure 16. Ion mill specimen holder cross-section.

į,

2.2 X-RAY DIFFRACTION

Zinc sulfide was used as an internal standard for indexing

he diffraction patterns generated by the zinc sulfide irradiated

ith nickel ions. The reflection spots of a transmission electron

icroscope (TEM) diffraction pattern are generated due to

onstructive interference of the waves of an electron beam which

ass through a small, selected area of a specimen, thus they are

alled "selected-area diffraction" (SAD) patterns. As they travel

hrough a TEM specimen, the beam is scattered by parallel atomic

anes in the specimen with interplanar spacing, d.

The known d-spacings for a standard material may be taken

The om the Powder Diffraction File, or "PDF" [37], or they may be

Cermined by other experimental techniques, such as x-ray

Fraction (XRD) or x-ray microanalysis. The interplanar d
Cings given in the PDF for a selected material are those

Coings which were found using these and other methods for

Coings which were found using these and other methods for

Coings which were found using these and other methods for

Coings which were found using these and other methods for

Coings which were found using these and other methods for

Coings which were found using these and other methods for

Coings which were found using these and other methods for

Coings which were found using these and other methods for

Coings which were found using these and other methods for

Coings which were found using these and other methods for

Coings which were found using these and other methods for

Coings which were found using these and other methods for

Coings which were found using these and other methods for

Coings which were found using these and other methods for

Coings which were found using these and other methods for

Coings which were found using these and other methods for

Coings which were found using these and other methods for

Coings which were found using these and other methods for

Coings which were found using these and other methods for

X-ray diffraction was implemented to determine the actual d-Spacings of the zinc sulfide ceramic used in the present work to improve the accuracy of the indexing calculations for the TEM diffraction patterns. Diffraction peaks in the XRD pattern of a material indicate the significant reflections from particular plane orientations at specific 20-angles, the orientations being

an indicator of the material constituents.

A round specimen 15 millimeters in diameter and 7 millimeters

Thick was placed in a holder made of corrugated plastic in which a

1 4 millimeter hole was cut. The surface of the ZnS protruded

approximately 1 millimeter above the holder surface. The surface

of the zinc sulfide was left in the "as received" condition, that

is, the surface was macroscopically smooth but not optically

ransparent.

A General Electric X-ray diffractometer was used to project

— rays into the zinc sulfide. The specimen surface relative to

— rays into the zinc sulfide. The specimen surface relative to

— rays into the zinc sulfide. The specimen surface relative to

— rays into the zinc sulfide. The specimen surface relative to

— rays into the zinc sulfide. The specimen surface relative to

— rays into the zinc sulfide. The specimen surface relative to

— rays into the zinc sulfide. The specimen surface relative to

— rays into the zinc sulfide. The specimen surface relative to

— rays into the zinc sulfide. The specimen surface relative to

— rays into the zinc sulfide. The specimen surface relative to

— rays into the zinc sulfide. The specimen surface relative to

— rays into the zinc sulfide. The specimen surface relative to

— rays into the zinc sulfide. The specimen surface relative to

— rays into the zinc sulfide. The specimen surface relative to

— rays into the zinc sulfide. The specimen surface relative to

— rays into the zinc sulfide. The specimen surface relative to

— rays into the zinc sulfide. The specimen surface relative to

— rays into the zinc sulfide. The specimen surface relative to

— rays into the zinc sulfide. The specimen surface relative to

— rays into the zinc sulfide. The specimen surface relative to

— rays into the zinc sulfide. The specimen surface relative to

— rays into the zinc sulfide. The specimen surface relative to

— rays into the zinc sulfide. The specimen surface relative to

— rays into the zinc sulfide. The specimen surface relative to

— rays into the zinc sulfide. The specimen surface relative to

— rays into the zinc sulfide. The specimen surface relative to

— rays into the zinc sulfide. The specimen surface relative to

— rays into the zinc sulfide. The specimen surface relative to

— rays into the zinc surface relative to

— rays into the zin

The x-ray diffractometer signal output graphs the reflection intensities versus the diffraction angle, 2θ . Bragg's Law [38] was used to calculate the d-spacings for the 15 largest diffraction peaks from the diffraction angle and the wavelength of the x-rays emitted from a copper source (λ = 1.542 angstroms). These were then correlated to the d-spacings and their respective diffracting planes for β -ZnS (sphalerite) listed in PDF Card No. 5-0566 [37]

An additional resource for indexing diffraction patterns are the standard spot pattern monographs of Rarey, Stringer, and Edington [39]. These illustrations provide information on single crystal patterns for various structure types including diffraction planes, radius ratios, and angles between reflections.

2.3 TRANSMISSION ELECTRON MICROSCOPY

A JEOL 100CX transmission electron microscope equipped with STEM (Scanning Transmission Electron Microscopy) and a LINK EDX (Energy Dispersive X-Ray) analytical system was used for all TEM observations of the nickel-irradiated and non-irradiated zinc sulfide specimens. The imaging mode, in bright- and dark-field, and the selected area diffraction (SAD) mode were used. A tungsten filament was the source for the electron beam with an celerating voltage of 100 kilovolts (100 x 103 volts).

Objective apertures 1 through 4 were 120, 60, 40, and 20

The Crons in diameter, respectively. Objective apertures 1 and 2

We be used for most of the observations in conjunction with a 10

The Crons condenser aperture and a diffraction aperture of 20

The Crons.

Preparation of the JEOL 100CX transmission electron

Socope for specimen observations was implemented according to second TEM operation procedures. Vacuum tweezers were used to specimens from a TEM specimen holder to the spring-loaded specimen stage. This stage included a +/- 60 degree tilt

Micrographs of images and diffraction patterns were taken

Kodak 4489 electron microscope film. The majority were taken

agnifications of 72,000 or 100,000 in imaging mode, or with a

ra length of approximately 55 centimeters (55 x 10⁻² meters) in

cted-area diffraction (SAD) mode.

As discussed in Section 2.2, X-ray diffraction was implemented to determine d-spacings for the zinc sulfide used in this study. The ZnS structure, intrinsic to the effects under study, acted as the internal standard for each of the electron diffraction patterns of the ion implanted material. The thinned region of the TEM specimens consisted primarily of zinc sulfide, in spite of the nickel irradiation of the surface. Therefore, the diffraction patterns generated by the irradiated material included the reflections of the zinc sulfide structure and those effections generated by any new phase or species present due to introduction of nickel by ion implantation. An accurate calculating the calibrated camera constant for each individual calculating the calibrated camera constant for each individual the internal standard material.

2.4 INDEXING TEM DIFFRACTION PATTERNS

Transmission electron microscope diffraction patterns of a "selected-area" of the specimen of nickel-irradiated and non-irradiated zinc sulfide were indexed to obtain information relevant to identifying the phases or species in the subsurface region of the ZnS. Relative interplanar angles, pattern ientation, and d-spacings between planes, which are determined radii measurements, all contribute to this analysis.

An Intertech hairspring divider, a compass-like precision

Suring device, and a transparent millimeter scale were used to

Sure the distances of diffraction spots from the central spot,

the angles between them. These measurements were made on the

Sion side of the negative of the micrographs to eliminate

rs which may occur when measuring distances on a contact

The radii were determined by measuring the distance

en spots symmetric about the center and dividing these values

The ratio of radii to focal length, R/L, in the electron of scope has been shown to correlate to the ratio of elerating electron wavelength to d-spacing [40]. Using this tionship, the interatomic spacings for the non-irradiated zinc fide pattern were calculated with $\lambda = 0.037$ angstroms, the elength of electrons for an accelerating voltage of 100 colors [40], and a non-calibrated camera constant of L = 550 colors.

ray d-sg on d diff and

> acci addi

> > gppr

inde

stru from

Zn.S.,

ī:.e

Whic Subs

cons Codi

iiff

These d-spacings were then compared to those given by the xray diffraction results and similarities were matched. A single
d-spacing from the XRD data was assumed as the most accurate based
on correlation to a significant reflection in the electron
diffraction pattern. Knowing the wavelength, \(\lambda\), the spot radii, R,
and a d-spacing for the actual ZnS material used, gave a more
accurate calibrated camera constant, L. Revised values for the
additional d-spacings were then calculated. The reflection planes
given by PDF were correlated to these results, and data from the
appropriate monograph [39] were used to confirm the pattern
indexing.

For the electron diffraction pattern of nickel-irradiated ZNS, features identified as representing the internal standard ZNS Lacture were indexed as above. Additional features resulting the ion implantation were then indexed in a similar manner. The d-spacings were calculated with the calibrated camera constant ch was determined by the measurements of the internal standard. Subsequently, various references for interplanar spacings were calculated to identify the phases or species present in the field specimen which exhibit the reflections in the electron in the Eraction pattern.

212

gpp

spec

àCet

2.5 HARDNESS

To assess the influence of the surface modification upon mechanical properties of zinc sulfide, the Vickers hardness of nickel-irradiated ZnS was determined and compared with that of non-irradiated ZnS. Further studies were conducted to examine the effects of annealing upon the hardness of implanted and

2 - 5.1 Nickel-implanted ZnS

Discs of zinc sulfide 15 millimeters in diameter and Exemple 2 proximately 5 millimeters in thickness were prepared, as cd i scussed in Section 2.1, to provide both irradiated and control Specimens for evaluating the influence of the irradiation and subsequent thermal treatment. Following the implantation P - edure, the irradiated and unmodified discs were each attached 🔁 lass slides with a low-temperature thermoplast. This Tation to the blade as that for the TEM specimens (see Figure - Post-cutting sample dimensions approximated parallelpipeds with top surface areas of about 30 square millimeters. This Cuting was completed with a diamond wheel saw blade on a Buehler at a mond saw with standard cutting oil used as a lubricant and Colling agent. Cutting oil contamination was removed by soaking specimens in warm water with a mild surfactant. Separate Tone and alcohol ultrasounds followed. Specimens were stored

ind

sto

tes:

The

sur:

and

lrav

Were

Were

each

30 5

Apg foli

Wr.e.

spec

fract

individually in 5 dram glass vials with screw tops which were then stored in a non-evacuated dessicant chamber.

Due to the depth of the indents made by the Vickers hardness

tester, actual hardness values represented those of a composite

consisting of the thin implanted layer and the unmodified bulk.

The sensitivity of the indentor to hardnesses of the modified sub
surface region was maximized by using the lowest available load of

kilograms-force for most of the hardness testing. The load time

and load speed were set at 15 seconds and 50 microns of indentor

avel per second, respectively.

Spacings between respective indentations and the sample edges

We be maintained at approximately 8 times the half-diagonal length

the indents for each of the specimens tested [41]. Specimens

soaked in acetone, then alcohol prior to hardness testing and

specimen was transferred to the specimen platform with Dupont

TEM tweezers.

Hardness was determined by entering Vickers indent data

Characteristic Pendix A) into a Basic program (Appendix B) which used the

Characteristic Pendix A) into a Basic program (Appendix B) which used the

Characteristic Pendix A) owing formula to calculate hardness in gigaPascals:

$$H = .464P/a^2$$
 (2)

Where, H = hardness, GPa (1x10¹² Pascals)

P = load, kilogram-force

a = average half-diagonal length of indent

.464 = material constant for ZnS [41].

Toughness values were calculated for the non-irradiated

Cimens, however, the decrease in contrast of the indented

Cture crack-lengths to that of the surface following

1

2

t:

re

te

ŗŗ

i.s

ÃO

5

in: 13 cor

thr

200 Cen

Mi]

ised the implantation and annealing was significant, and prevented measuring the crack lengths for the nickel-irradiated ZnS.

2.5.2 Annealed Nickel-implanted ZnS

Annealing of nickel-irradiated zinc sulfide was implemented to initiate thermal activity such as, radiation-enhanced diffusion, and to enhance precipitation of nickel sulfide. To test the effect of annealing upon the surface-modified ZnS with respect to mechanical properties, a control specimen of ZnS was included with an irradiated specimen for each anneal cycle, and pre-and post-anneal hardnesses were measured.

Annealing cycles were run in a Centorr Series M60 Front

Access vacuum furnace (Model No. M60-3x8-W-D-04S4-A-20, Centorr

Associates, Inc, Route 28, Suncook, New Hampshire 03275; 603-4859504). The furnace stage upon which the specimen crucibles were
placed was a tantalum plate which was located approximately 3
inches from the thermocouple. The initial chamber temperature was
15 degrees celsius and the furnace chamber was maintained under
constant argon pressure such that argon gas flow from the chamber
through a gas venting valve was approximately 10 cubic centimeters
per minute.

The specimens were ultrasonically cleaned with acetone and 200 proof alcohol, then placed in alumina crucibles (Coors Ceramics Company, Golden, Colorado) with dimensions of 30 \times 9 \times 7 millimeters. Dupont Type 3c TEM tweezers cleaned in alcohol were used for transport of the specimens. The crucibles were placed on the tantalum stage in the furnace chamber with Teflon coated lab

t: ur ur s:

> ξ; ...

> > w)

à

t.

7. 11. 11.

ā:

17.

tongs. To minimize transfer of volatiles or other species between treated and untreated specimens, each specimen was placed in an upright crucible with the surface for hardness testing facing upward. This was then covered with another crucible of the same size, inverted such that the edges of the "bowls" of the crucibles met. Each such crucible arrangement was dedicated to irradiated or non-irradiated specimen processing.

The chamber was evacuated to 50 millitorr, then backfilled with argon. This procedure was repeated twice then followed by initiation of the heating cycle. The three temperature profiles which were implemented reached maximums of 750, 800, and 850 degrees celsius. An auto-controller unit was used to set the profiles such that the ramps to maximum temperature were approximately the same. The objective was to reach this maximum as rapidly as the furnace/controller unit could accomodate while still maintaining relative uniformity in the ramps to the peak temperature between each profile. Upon reaching the target temperature, the heat zone power was terminated and the argon flow was maintained for approximately one hour. The three thermal profiles used in the annealing of the specimens are shown in Figure 17. Specimens were removed six to eight hours later using Teflon-coated tongs and TEM tweezers. Each was returned to their respective glass vial and stored in a dessicant cabinet.

Vickers indent data and respective hardnesses for the annealed specimens were obtained using the same procedure as described for the nickel-irradiated zinc sulfide samples. This data is also included in Appendix B.

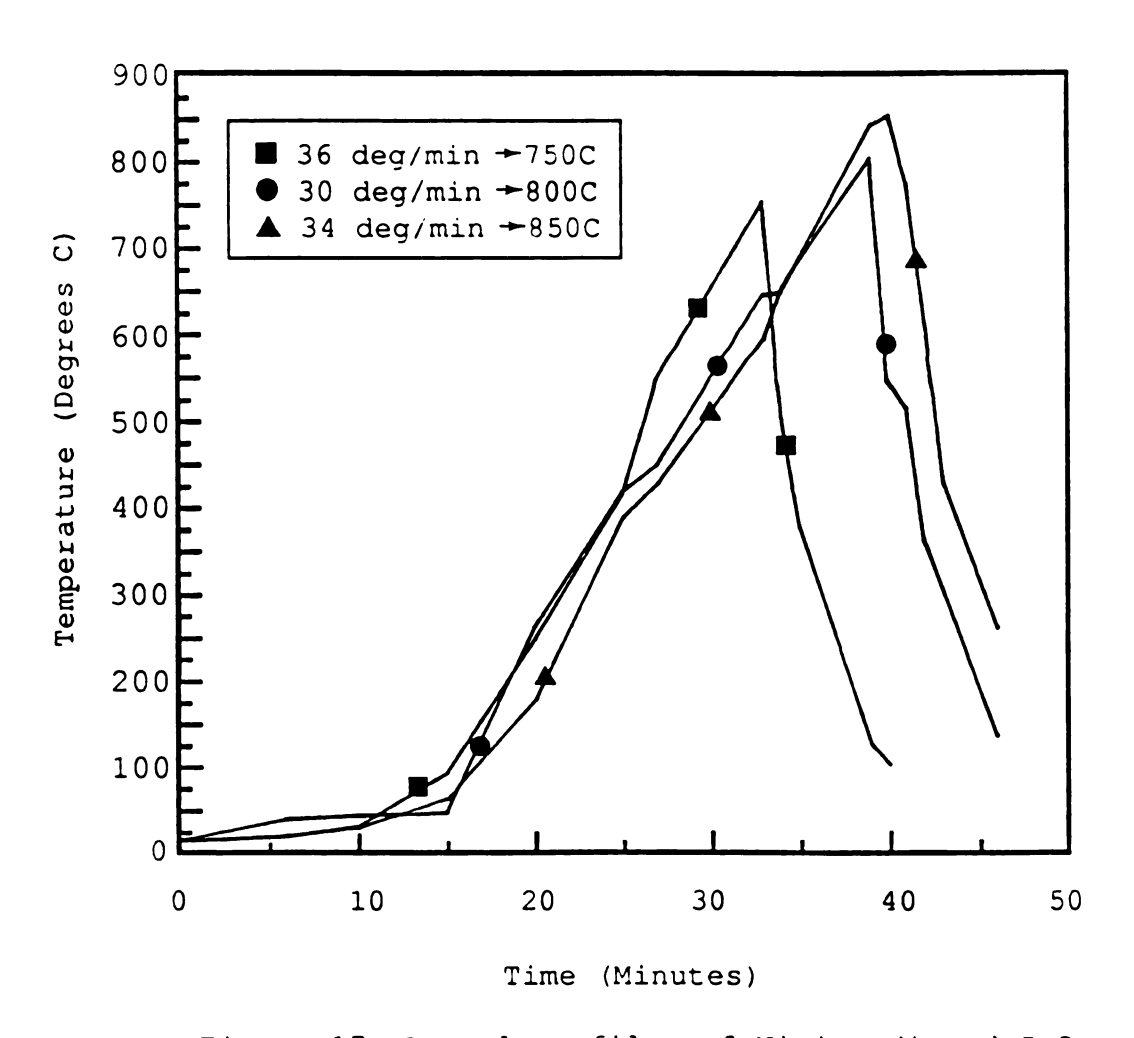


Figure 17. Anneal profiles of Ni-irradiated ZnS.

2.6 SCANNING ELECTRON MICROSCOPY

Nickel-irradiated zinc sulfide specimens underwent SEM (scanning electron microscopy) and EDX (energy-dispersive x-ray) analyses before, and after thermal annealing. Post-annealed non-irradiated ZnS specimens were analyzed as well. SEM micrographs of the zinc sulfide surfaces were obtained with a JEOL JSM-35C at 20 kilovolts. A Tracor Northern D500 X-ray system provided information on the presence and relative concentration of nickel in the ZnS utilizing a Standardless Quantitation computer program.

The annealed and non-annealed nickel-irradiated zinc sulfide specimens were prepared for SEM by attachement to aluminum SEM specimen mounts with a small drop of Conducting Graphite Paint [Ladd Research Industries, Inc., Burlington, VT]. These were then placed in a low-temperature oven set at approximately 60 degrees celsius for approximately seven minutes followed by ten minutes of cooling.

The areas scanned by EDX for each specimen was approximately 10,000 square microns. Tilting angles of the detector were 27 and 0 degrees with a detector distance of 55 millimeters and a working distance of approximately 39 millimeters.

2.

Sp mo:

en

ė.

pi: pa

ve e1

> 35 30 37

> ei ie

îâ

81

÷e ¥e

iz Ti

ŝę.

2.7 X-RAY PHOTOELECTRON SPECTROMETRY

Surface analysis by ESCA, or XPS (X-ray Photoelectron Spectrometry), involves irradiating the surface of a specimen with monoenergetic soft x-rays and sorting by energy the resulting emitted electrons. Each element has a set of electron binding energies that are unique. The kinetic energies of the inner-shell electrons ejected from the surface are equal to the incident photon energy minus the electron's binding energy at its particular level in the electron shells of the solid.

A plot of the number of emitted electrons per energy interval versus their respective kinetic energies yields the unique elemental spectrum. The peaks in the spectrum from a compound are approximately the sum of the elemental peaks from the individual constituents. The mean free paths of the electrons are very small, therefore only the top few atomic layers actually emit electrons from the specimen surface which are registered by the detector. Typical mean escape depths range from 0.3 to 3 nanometers for a kinetic energy of 100 eV.

XPS was performed to measure the presence of nickel or nickel sulfide in the subsurface region of the nickel-irradiated ZnS. A Perkin-Elmer PH1 5400 Small Spot X-ray Photoelectron Spectrometer was used for this analyses. Specimens were the round nickel-irradiated ZnS samples, 15 millimeters in diameter and 3 millimeters thick, and the annealing specimens described in Section 2.5.

CHAPTER 3. RESULTS AND DISCUSSION

The results of the analytical work which lead to the conclusions in Chapter 4 are reviewed and discussed here. First is a preview of the role ion milling effects may have had in the images of the microstructures. Quantitative results from x-ray diffraction lead into the main work conducted with transmission electron microscopy. Hardness comparisons between irradiated specimens and specimens annealed following irradiation is presented with a review of possible mechanisms. The mechanisms proposed are discussed relative to results from scanning electron microscopy and x-ray photoelectron spectrometry. This is followed by a section on diffusion.

3.1 ION MILLING EFFECTS

Zinc sulfide specimens irradiated with nickel ions were thinned by dimple grinder perforation followed by ion milling. The procedure of ion milling involves the conversion of inert gas atoms to a plasma of ions which are then accelerated towards the target material at a glancing angle to physically bombard and sputter the target atoms by transfer of energy. The glancing angle of the incident ions results in removal of the atoms and a "thinning" of the target. Eventually a perforation in the target material forms and the area immediately adjacent to the perforation is transparent to incident electrons. The use of

high energies and the physical nature of this phenomenon result in various effects which may be exhibited through transmission electron microscope observations.

Figure 18 is a micrograph of an ion-implanted ZnS specimen prepared by ion milling and observed in the imaging mode with a JEOL 100CX Transmission Electron Microscope. Exposure time was 1.4 seconds. The view given by this micrograph is from a point perpendicular to the specimens plane; this is the reference for all of the following micrographs. At a magnification of 100,000x (100k), the thinning effect ion milling had upon the specimen is evident. The extreme edge adjacent to the perforation is the thinnest part of the material. Moving towards the thicker region, detail of the material structure is less apparent due to the decrease in electron transparency.

In addition to thinning a material to electron transparent dimensions, ion milling may also contribute undesired effects which may alter the structural detail of an irradiated material, thus prohibiting the analyses of a ceramic which has only experienced the effects of ion implantation. Ion milling physically removes atoms, therefore, an atomically rough surface results. Variations in thickness may be present such that maximum and minimum variations occur over very small distances, i.e. nanometers. Transmission electron micrographs containing artifacts which may be attributed to ion milling effects are shown in the following figures.

A "saw tooth" appearance can be seen in the dark-field image of Figure 19 which may have resulted from variations in ion

Ċ F

٧

2

0

ŗ

beam energy and intensity. Another observation, illustrated in Figure 20, is the presence of light regions which appear as "trails" in the material with an orientation corresponding to the direction of the ion milling beam. Sensitivity of the material's removal rate to beam-energy oscillations may have caused these variations. (The ZnS thinning rate was determined empirically to be approximately 150 nanometers per minute at 5 keV and 68 degrees to specimen normal). The rotation of the thinned edge through the beam by stage rotation may add further variability to the milling conditions. This, however, is only one speculation as to the cause of these artifacts. The ZnS also underwent dimple grinding, in which an imperfect grinding wheel may have influenced grain orientation in the surface of the material.

Figure 21 is a TEM dark-field image of the nickel irradiated ZnS, and corresponds to the location of the bright-field image shown in Figure 20. This micrograph was taken at 100k magnification with an exposure time of 32 seconds. The striations are less apparent in this image, however, small bright "spots" can be seen along the edge. This is evidence that precipitants of one or more phases may be present in the near-surface region of the bulk material.

A bright-field image of the specimen edge adjacent to that shown in Figure 21 can be seen in Figure 22. This image, also magnified at 100k, and exposed for 0.7 seconds, shows dark regions, larger than the spots in the previous micrograph, located at the extreme edge of the specimen. Originally suspected to be precipitants, these spots were estimated to be ranging in size

from approximately 10 to 50 nanometers. Their wide spacing and non-uniform distribution are characteristics that were neither anticipated for the nickel ions implanted in the ZnS, nor for any initial precipitations which may have occurred by the combining of nickel with either zinc or sulfer. Therefore, these regions may also be artifacts of ion milling, or they may be indicative of structural detail at the edge. However, viewing this same region in dark-field mode (Figure 23) revealed reflections with relatively small size and spacing, as well as uniformity in distribution. These features appear to be similar to those observed in Figure 21.

The selected-area-diffraction pattern generated by the specimen image of Figure 23 is shown in Figure 24. The large parallel reflections are those of zinc sulfide. Concentric rings of much smaller reflections also appear in this pattern, and were suspected of resulting from diffraction by the small reflections observed in the imaging mode. The ZnS x-ray diffraction results are presented in the next section, followed by the discussion on the imaging and indexing of reflections and rings in Figure 24.



Figure 18. TEM micrograph of thinned edge of 200keV Ni-irradiated ZnS. (Mag:100k)

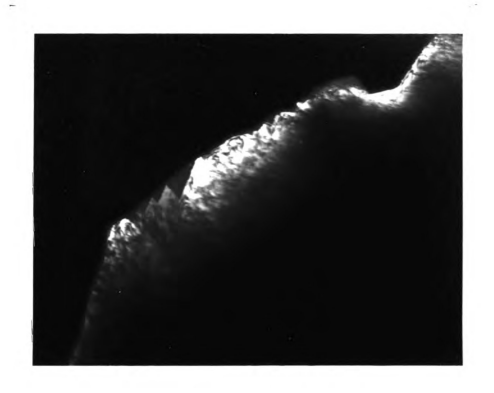


Figure 19. "Saw tooth" features observed in TEM micrograph of 200keV Ni-irradiated ZnS. (Mag:100k)



Figure 20. Bright-field TEM micrograph of 200keV Ni-irradiated ZnS. (Mag:100k)

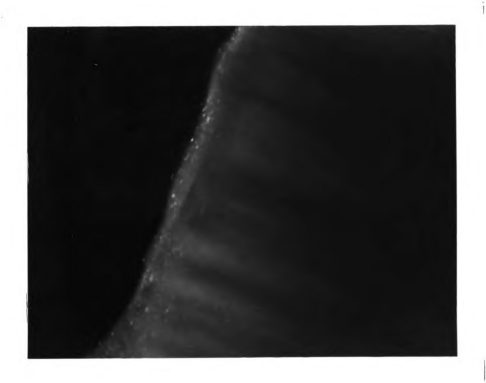


Figure 21. "Reflections" observed in dark
-field TEM micrograph of 200keV
Ni-irradiated ZnS. (Mag:100k)



Figure 22. Bright-field TEM micrograph in precipitant-rich region of Ni-irradiated ZnS. (Mag:100k)



Figure 23. Dark-field image of region in Figure 22 showing precipitant reflections in Ni-irradiated ZnS. (Mag:100k)

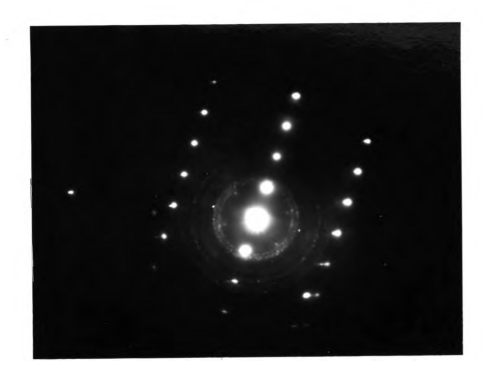


Figure 24. Selected-area diffraction pattern of 200keV nickel-irradiated ZnS. (Mag:100k)

3.2 X-RAY DIFFRACTION

Figure 25 shows the diffraction pattern generated by the detection of x-rays deflected at various angles from the atomic planes of zinc sulfide. The 2θ -angles and the reflecting plane indices are indicated. Table 2 lists the 2θ -angles measured from the diffraction pattern, an intensity rating for each peak (1 = strongest peak), and the corresponding plane's d-spacing as calculated from Braggs Law. These are also listed for sphalerite (β -ZnS) from PDF card no. 5-0566. A rating was assigned to the relative intensities given for ZnS in the Powder Diffraction File to show the intensity correlations between the PDF and the XRD peaks. The d-spacings determined by the XRD analysis were used for the internal standard method of electron diffraction pattern calibration.

Table 2. XRD Diffraction data for $\beta\text{-}\text{ZnS}\,.$

Peak					
Intensity		d (A)		d (A)	
<u>Rating</u>	20 (deg)	XRD	PIR	_PDF	<u>(hkl)</u>
7	26.00	3.427			
1	28.75	3.106	1	3.123	(111)
6	33.50	2.675	4	2.705	(200)
13	43.00	2.104		-	-
2	47.75	1.905	2	1.912	(220)
15	50.80	1.798		-	-
3	56.70	1.624	3	1.633	(311)
12	59.50	1.554	9	1.561	(222)
10	69.70	1.349	6	1.351	(400)
5	76.80	1.241	5	1.240	(331)
14	79.25	1.209	9	1.209	(420)
4	88.60	1.1039	5	1.1034	(422)
9	95.60	1.0408	7	1.0403	(511)
11	107.50	0.9560	8	0.955 7	(440)
8	115.00	0.9142	7	0.9138	(531)

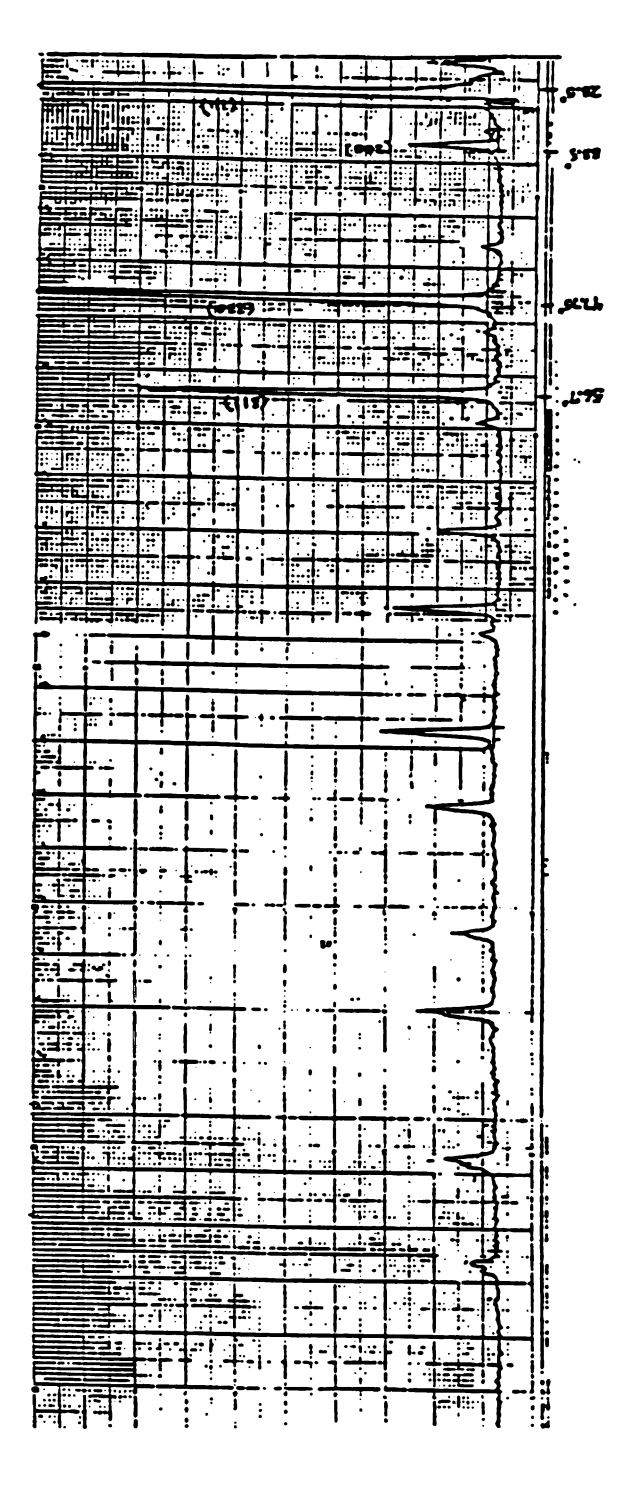


Figure 25. X-ray diffraction pattern of ZnS.

3.3 TEM RESULTS

The bright- and dark-field transmission electron micrographs of the nickel-irradiated zinc sulfide are shown in Figures 22 and 23. These images show illuminated spots which are small in size and display a relatively uniform distribution. These features indicate the presence of precipitation activity within the implanted subsurface region of the ZnS. A greater concentration appears to be present at the surface of the specimen. However, a decrease in the electron transparency of the specimen away from the edge would reduce the number of spots it could illuminate, in spite of concentration uniformity. Therefore, the concentration of the "precipitants" may in fact be uniform. (This may be investigated by observing a cross-section type sample using the procedure described in work by McHarque et. al. [18].)

The illuminations were estimated to have an approximate size of 5 to 10 nanometers. This observation is consistent with the fact that the specimen was not annealed, hence, minimal growth of precipitants would be expected. The only apparant sources available for thermally motivated effects were the ion milling procedure and specimen heating from the transmission electron beam. Ion milling may elevate specimen temperatures several hundred degrees celsius if a method of cooling is not implemented. The irradiated ZnS specimens, however, were thinned while in contact with a cooling stage which maintained the specimens at or below room temperature. Relative to typical annealing

temperatures, the effects would be negligible, particularly with respect to the bulk material. However, heating from the TEM electron beam may have been sufficient to result in modifications to the very thin implanted layer in the specimen. This applies, as well, to the potential for electron beam heating of the specimen surface.

As was discussed in Section 1.2, radiation-enhanced diffusion (RED) is dependent upon thermal activation and moves an atomic system in the direction of equilibrium. The enhancement is realized as the large number of radiation-induced vacancy, substitutional, and interstitial defects move through the atomic structure towards positions with lower free energies. Typically, their concentrations far exceed their equilibrium solubility limits. For this reason, the thermal energy required for their activation to diffuse is less than that required for a stable, equilibrium condition. In the event that a low but sufficient amount of thermal energy was available to initiate diffusion and precipitation of a nickel species, the growth of the precipitants would be expected to have sizes consistent with limited growth kinetics.

Their sizes may also be limited by the competing phenomenon of radiation-induced segregation (RIS). This process enhances the mobility of species due to defect fluxes which are localized, and independent of thermal energy. These fluxes exist due to the local variations in concentration. Solutes (and other species) preferentially couple to these fluxes and are transported to various defect sinks, such as vacancies, grain boundaries, or the

surface. Though the microstructure is moved in a direction away from equilibrium arrangement by this effect, the local compositional changes induced by RIS may be sufficient to precipitate a phase with composition that is normally unstable. It is likely that the diffusion and segregation mechanisms were both operative during the implantation process. Also, it is possible that each contributed to the formation of the precipitants observed.

It is suggested that the constituents of the precipitate phase are nickel atoms bonded with sulfur atoms. This infers that implanted nickel ions predominately displaced zinc atoms and formed bonds with sulfur atoms. The displacement energy for zinc is between 7 and 9 electron-volts, and for sulfur is between 15 and 20 electron-volts[42]. ZnS may, therefore, have become supersaturated with NiS in a metastable state. This condition in the presence of a high concentration of vacancies is one in which the precipitate transformation reaction may occur. Using the general equation from Section 1.2, the reaction for the irradiated ZnS may be described as:

$$\alpha' --> \alpha + \beta$$
 (4)

where, α' = the metastable supersaturated solid solution of nickel, zinc, and sulfur;

- α = ZnS structure with nickel retained closer to an equilibrium concentration;
- β = stable and metastable precipitants of β -NiS and α -Nis, respectively.

The selected-area diffraction pattern, formed in the back focal plane of the electron microscope, of the specimen of Figure 23 was exposed for 64 seconds, and is shown in Figure 24. This micrograph includes two significant features. First is the pattern of reflections forming three rows, with approximately equal spacing between each other, and between the reflections in each row. Second is the group of concentric rings which encircle the center spot. The rings consist of very fine reflections, indicative of a very fine crystalline structure. This was determined by inspection of the rings in an enlargement of Figure 24. Also in this figure, diffuse rings, typical of a diffraction pattern for an amorphous structure, were not observed. From this it can be concluded that no amorphization of the ZnS structure occurred as a result of the implantation.

3.4 INDEXING DIFFRACTION PATTERNS

3.4.1 Zinc Sulfide

Figure 26 shows the selected-area diffraction pattern of the unmodified zinc sulfide ceramic. Exposure time was 110 seconds at an approximate camera length of 55 centimeters. The reflections are illustrated in Figure 27 and are labeled A through E.

Interplanar angles are also shown. A single-crystal diffraction pattern monograph from reference [39] matches the pattern of Figure 26, and is shown in Figure 28 with the reflection indices and relevant angles indicated.

Table 3 lists the data and calculations determined by indexing for the diffraction pattern of Figure 26. The second and third columns list the radii for reflections A through E and the corresponding d-spacings. The spacings were calculated from Bragg's Law, using the approximate camera length of 550 millimeters. D-spacings from the ZnS x-ray diffraction data, which were determined to be the closest in value to the calculated spacings, are also listed along with the plane indices. Next are the indices for each of the reflective planes found to be the sources for the reflection positions by comparison of these positions with those in the reference monograph. Finally, agreement between the plane families indicated by the monograph and those determined through d-spacing correlations are noted.

A single agreement exists by comparing planes in Table 3 for

-

reflection B which has a d-spacing of 2.675 angstroms and indices of (200). Substituting this d-spacing into the camera constant equation, $\lambda L = Rd$, results in a camera constant of 2.207 (square millimeters). Using this calibrated camera constant, recalculated d-spacings for reflections A through E were found and are listed in Table 4. Comparing the XRD planes with those from the monographs resulted in agreement between the plane families for each of the reflections from the diffraction pattern for zinc sulfide. The matching angles shown in the monograph and the diffraction pattern add further confirmation that this monograph is representative of the ZnS selected-area diffraction pattern.

The pattern of Figure 24 was produced by electron beam transmission through ZnS at a particular crystallographic orientation. Patterns from different orientations will result in different reflection arrangements, interplanar angles, and reflection intensities. However, the presence of at least one reflection that was common between the unmodified and modified ZnS SAD patterns allowed the use of the internal standard method of calibration, regardless of crystallographic orientation. This was observed for the pattern generated by electron transmission through the modified ZnS.

Table 3. Indexing data for SAD pattern of unmodified ZnS using camera constant of 2.035.

<u>Label</u>	Reflection Radius (mm)	d-spacing (A)	Closest XRD Spacing	Monograph Plane	<u>Aggr</u>
A	7.50	2.713	2.675 (200)	(111)	no
В	8.25	2.467	2.675 (200)	(200)	yes
С	12.25	1.661	1.624 (311)	(022)	no
D	14.25	1.428	1.349	(311)	no
E	18.68	1.089	1.041 (511)	(133)	no

Table 4. Indexing data for SAD pattern of unmodified ZnS using camera constant of 2.707.

<u>Label</u>	Reflection Radius (mm)	d-spacing (A)	Closest XRD Spacing	Monograph Plane	Aggr
A	7.50	2.943	3.132 (111)	(111)	yes
В	8.25	2.675	2.675 (200)	(200)	yes
С	12.25	1.802	1.905 (220)	(022)	yes
D	14.25	1.549	1.624	(311)	yes
E	18.68	1.181	1.241 (331)	(133)	yes



Figure 26. Selected-area diffraction pattern of zinc sulfide. (Mag:100k)

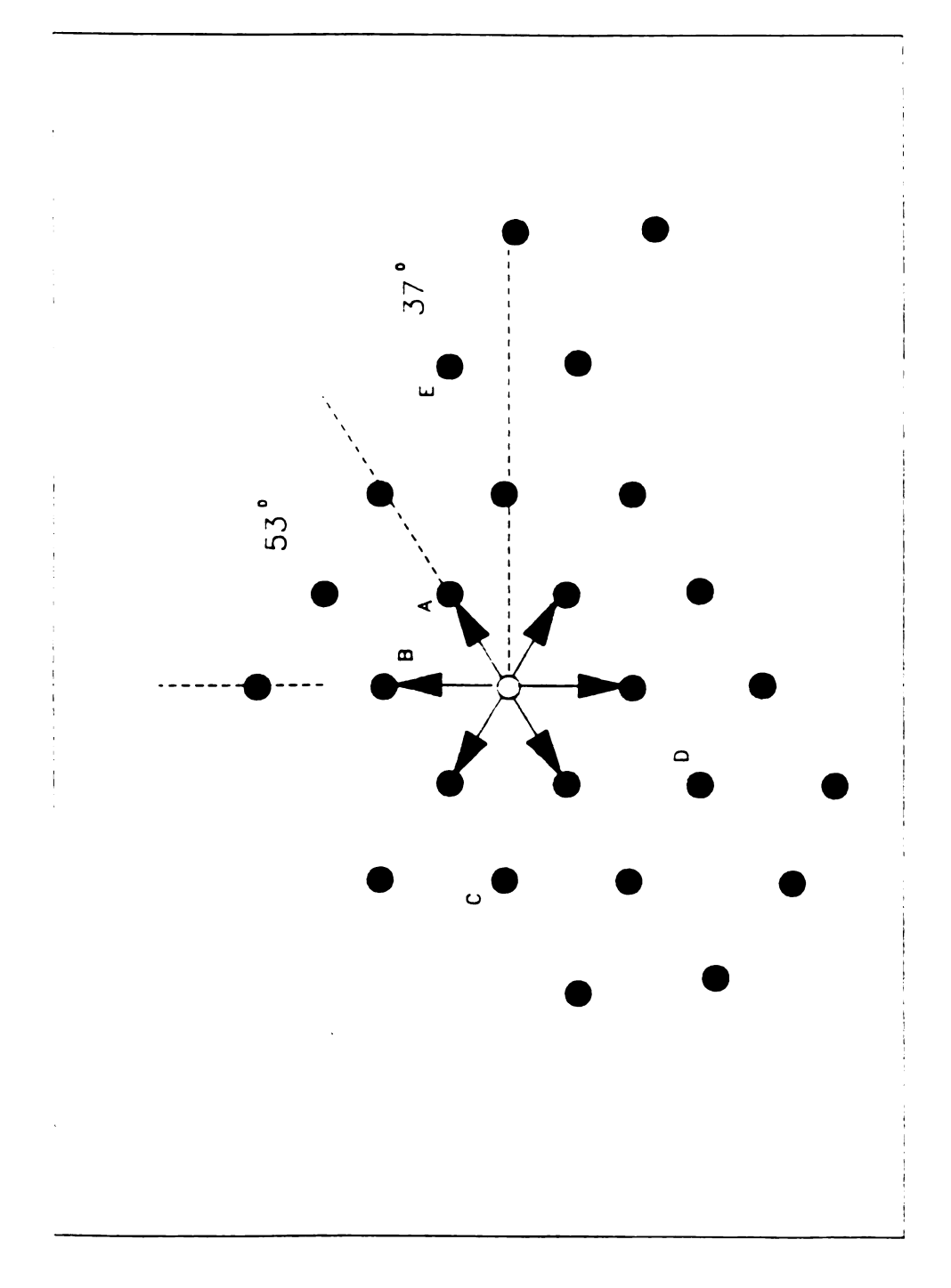


Illustration of ZnS selected-area diffraction pattern of Figure 26. Figure 27.

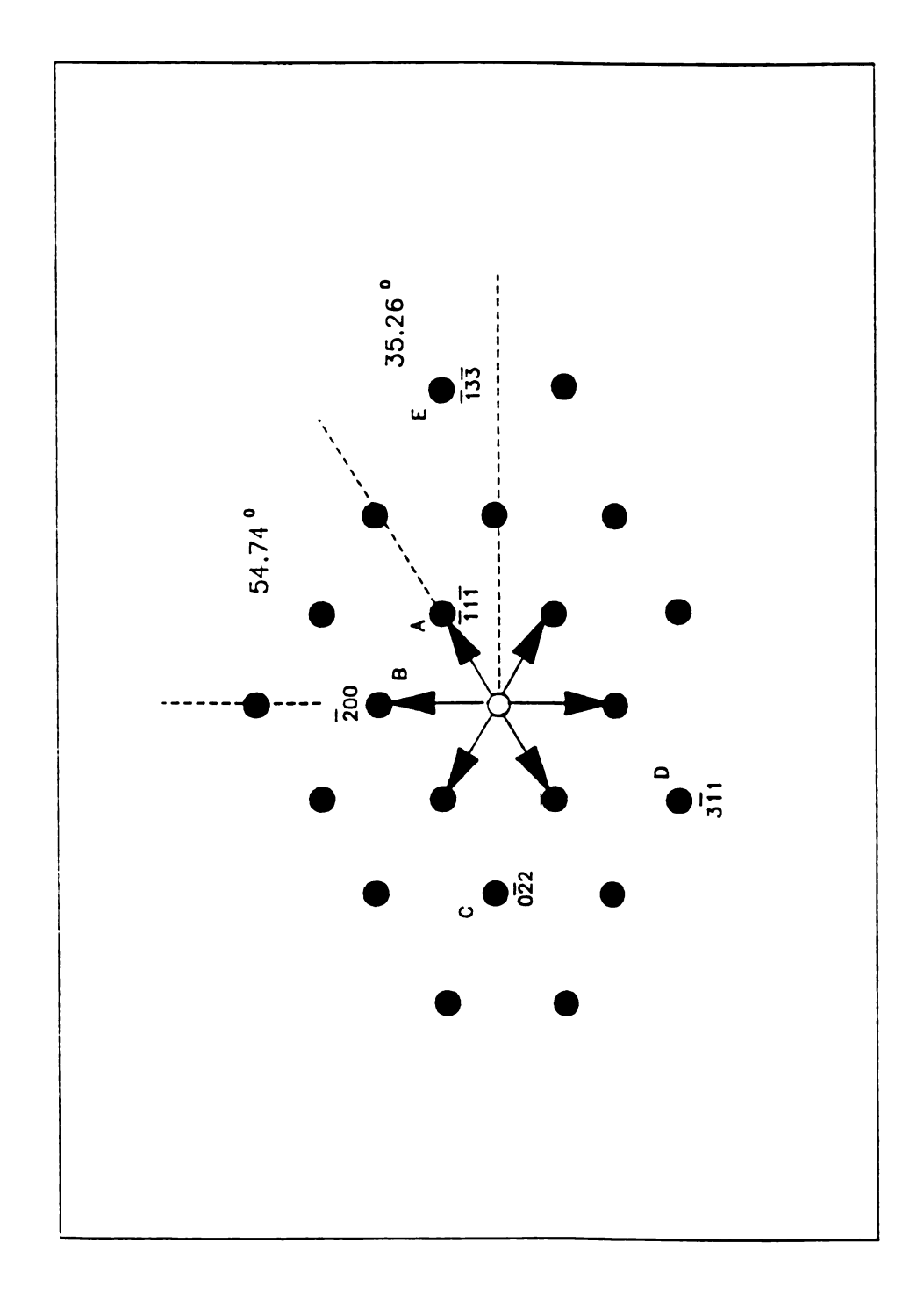


Figure 28. Monograph matching ZnS in Figure 26.[39]

3.4.2 Nickel-Implanted Zinc Sulfide

The selected-area diffraction pattern obtained with the nickel-irradiated zinc sulfide specimen is shown in the micrograph of Figure 24, and is illustrated with labels in Figure 29.

Reflection spots have been assigned the letter designations of A through H, and numbers 1 through 7 identify the individual rings.

The indexing data for the irradiated ZnS pattern are given in tables similar to those for the unmodified ZnS SAD pattern.

Table 5 lists the radii for the reflection spots, the initial approximated d-spacing calculations (camera constant = 2.035), the closest d-spacings from the XRD data, the plane of reflections indicated by the reference monograph, and any correlation ascertained by comparison. The reference monograph pattern for the irradiated ZnS diffraction image is illustrated in Figure 30.

Table 5. Indexing data for irradiated ZnS using calibrated camera constant of 2.035.

<u>Label</u>	Reflection Radius(mm)	d-spacing (A)	Closest XRD spacing	Monograph Plane	Aggr
Α	6.50	3.131	3.106 (111)	(111)*	yes*
В	6.75	3.105	3.106 (111)	(111)	yes
С	9.25	2.200	2.104	-	
D	17.00	1.197	1.209	(242)	no
E	17.50	1.163	1.209/1.241 (420)/(331)	(331)	yes
F	17.75	1.146	1.104 (422)	(420)	no
G	20.50	0.993	0.956((440)	(511)	no
Н	23.50	0.866	0.855		
			(620)	(153)	no

^{(* -} by comparison to Figure 28)

The data in Table 5 shows that agreement exists between the XRD plane indices and those indicated by the reference monograph for three reflections. The first is of reflection spot A. illustration of Figure 29 indicates this reflection is atypical. It is not included in any of the three rows of reflections which represent the bulk ZnS. Additionally, its location is clearly interior to the inner ring, thus it is not believed to be associated with the ring reflections. Yet, this spot does appear to be part of a regular pattern. Three additional spots are present within ring 1 which form, with spot A, an arrangement which is symmetrical about the central axis of the diffraction pattern. Table 5 indicates they have plane indices of {111}. However, reflection B also appears to be (111) related. symmetry of these four reflections, the angles between them, and their d-spacing all indicate they are the (111) reflections indexed for the non-irradiated ZnS pattern, as shown in Figure 27.

The SAD patterns of Figures 26 and 24, excluding the rings, have both been presented as those of ZnS. The reflection arrangements appear different as a result of variation in the angle of the incident electron beam with respect to the crystal orientation. Double diffraction, the phenomenon whereby a secondary diffracted beam acts as a primary incident beam, may have been the cause for the atypical reflections in the irradiated specimen. This may be the reason that a pattern similar to that observed in Figure 26, for the unmodified ZnS is present in the irradiated ZnS reflection arrangement. Spot A in Figure 24 may be the same reflection as that represented as A in Figure 26.

The second agreement noted in Table 5 exists between the plane indices indicated by the XRD, and monograph data for reflection B. The spot is located in a main row of reflections, therefore it is not suspected as resulting from double diffraction. Additionally, the calculated d-spacing of 3.105 angstroms (10⁻¹⁰meters) is a close match to 3.106 angstroms, the d-spacing from the (111) XRD peak. Furthermore, the (111) peak was that which exhibited the greatest x-ray diffraction intensity, which lends further confidence to the d-spacing correlations. With B as the internal standard reflection with a d-spacing of 3.106 angstroms, the calibrated camera constant was calculated as 2.097.

Table 6 lists the indexing data, revised by the calibrated constant, for the pattern of reflections in Figure 24.

Correlation was found for five of the eight reflections which strongly suggests that the main pattern for the irradiated specimen does represent zinc sulfide. The angles between reflections which are illustrated in Figure 29 and the monograph pattern of Figure 30, further indicate correlation for this pattern.

The reflection labeled C in the diffraction pattern is shown in both tables as having correlation to the XRD d-spacing of 2.104 angstroms. This d-spacing was calculated for the XRD peak of 43.00 degrees 2θ which had a Peak Intensity Rating of 13, i.e., an extremely low intensity. No extraneous reflections were observed in the unmodified ZnS SAD pattern, and the d-spacing of 2.267 angstroms calculated from the modified ZnS data was not a value in

the unmodified indexing. Further assessment of this reflection is discussed with the results of indexing the rings in the modified ZnS pattern.

Table 7 lists the radii and calculated d-spacings for each of the rings observed in Figure 24. It was hypothesized that these rings were generated by very fine crystalline precipitates of nickel sulfide. Data supporting this hypothesis came from the d-spacings of the rings. The data given in Table 7 are for d-spacing calculations using the calibrated camera constant of 2.097, as determined by the internal standard based upon reflection B.

An additional improvement in indexing the rings was obtained by use of an 8 inch by 10 inch enlargement of the SAD pattern. The rings in the original negative were spaced very close together thus resulting in greater probability of error in measuring the radii. Measurement of the radius for spot B on the original negative was assumed to be the most accurate because of the reflection intensity and uniformity. Therefore, the enlargement factor was determined from the ratio of radii measurements for reflection B on the negative and on the enlargement. This was found to be 0.342. Multiplying this into the radii measured from the enlargement resulted in more accurate ring radii from the original SAD pattern negative. The results from this procedure, and the corresponding d-spacings are given in Table 8.

Reflection C, discussed previously, is also listed in this table with the corresponding corrected d-spacing as determined by the enlargement measurement.

Table 9 shows the correlations made between the d-spacings for the rings produced by the nickel-irradiated zinc sulfide specimen and those for various phases of nickel sulfide. The correlating phases are those which most closely match the ring data out of all the available data for phases involving any two, or all three of the nickel, zinc, and sulfur elements. The data for α - and β -NiS were taken from [42], the others from the Powder Diffraction Files. [37]

Table 6. Indexing data for "reflections" in irradiated ZnS with a camera constant of 2.097

<u>Label</u>	Reflection Radius(mm)	d-spacing (A)	Closest XRD spacing	Monograph Plane	<u>Aggr</u>
Α	6.50	3.226	3.427	-	
В	6.75	3.106	3.106	(111)	yes
С	9.25	2.267	2.104	-	
D	17.00	1.234	1.241 (331)	(242)	no
E	17.50	1.198	1.209/1.241 (420)/(331)	(331)	yes
F	17.75	1.181	1.209 (420)	(420)	yes
G	20.50	1.023	1.041 (511)	(511)	yes
Н	23.50	0.892	0.9142 (531)	{153}	yes

Table 7. Indexing data for ring pattern of Figure 24 with camera constant of 2.097.

Ring <u>Number</u>	Radii <u>(mm)</u>	d-spacing (angstroms)
1	7.50	2.796
2	8.00	2.621
3	8.75	2.397
4	11.50	1.823
5	13.25	1.583
6	14.75	1.422
7	15.75	1.331

Table 8. Indexing data for ring patterns from enlargement of Figure 24 with calibrated camera constant of 2.097.

Ring <u>Number</u>	Enlargement Radii (mm)	Corrected Radii (mm)	d-spacing (angstroms)
1	21.75	7.44	2.819
2	23.50	8.04	2.608
3	25.50	8.72	2.405
4	31.75	10.86	1.931
5	37.75	12.91	1.624
6	41.25	14.11	1.486
7	45.00	15.39	1.363
С	26.50	9.06	2.314

Table 9. Comparison of Ni-irradiated ZnS d-spacings to various phases of nickel, sulfur, and zinc.

Ni-ZnS d-spacings

d-spacings						
(angstroms)	<u> α-NiS</u>	β -NiS	β-ZnS	<u>Ni3S2</u>	NiS2	<u>Ni3S4</u>
					_	
0.010						
2.819					2.830	2.850
					(200)	(311)
2.608	2.602					
2.000	(101)					
	(101)					
2.405		2.404				
25		(220)				
		(220)				
1.931			1.912			
			(220)			
1.624		1.634	1.633		1.634	
		(321)	(311)		(311)	
1.486	1.489					
	(200)					
1.363		1.388			1.375	1.369
		(600)		(015)	(410)	(444)
					(322)	
2.314		2.227				
2.314		(211)				
		(211)				

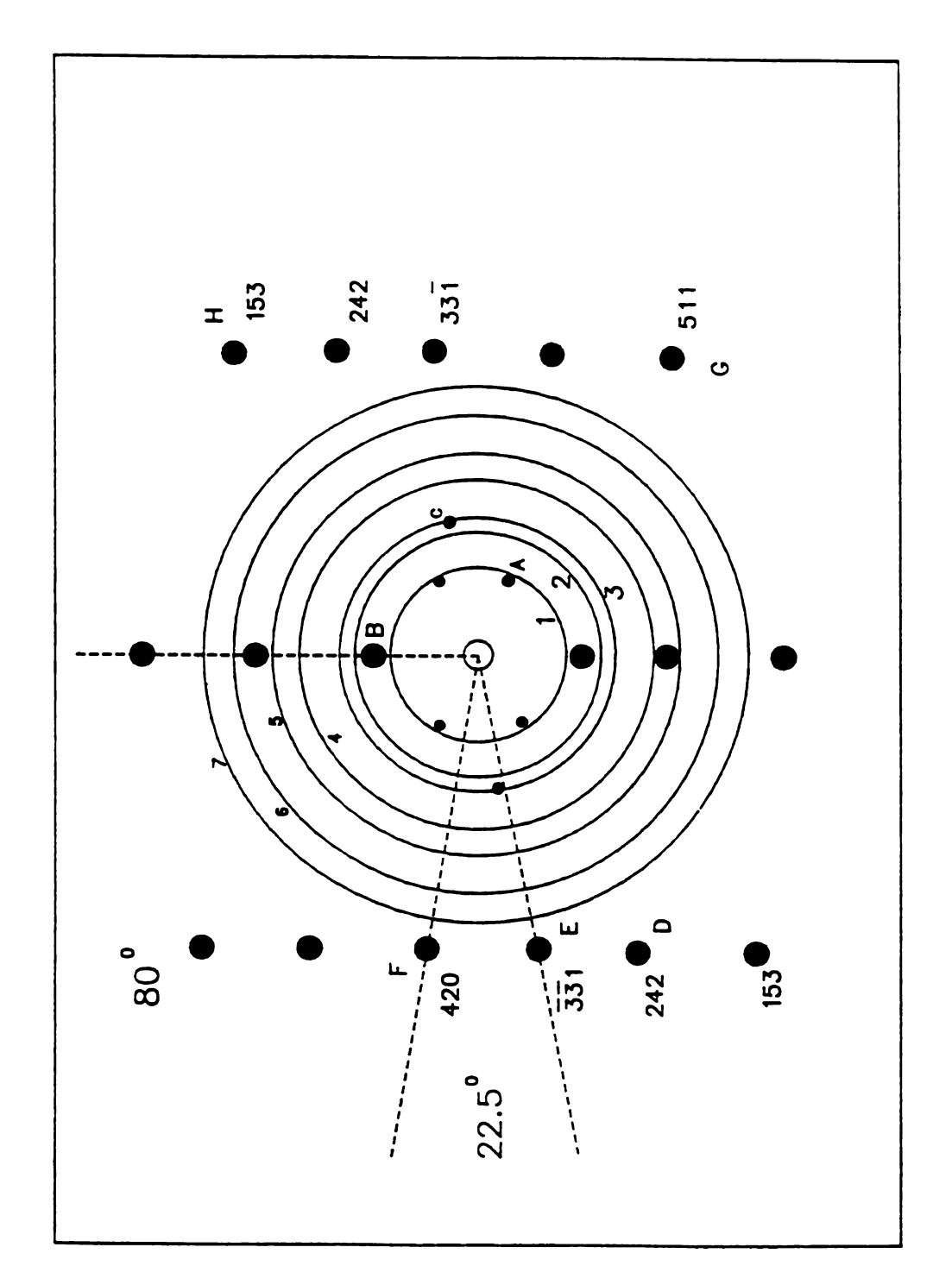


Figure 29. Illustration of Ni:ZnS pattern of Figure 24.

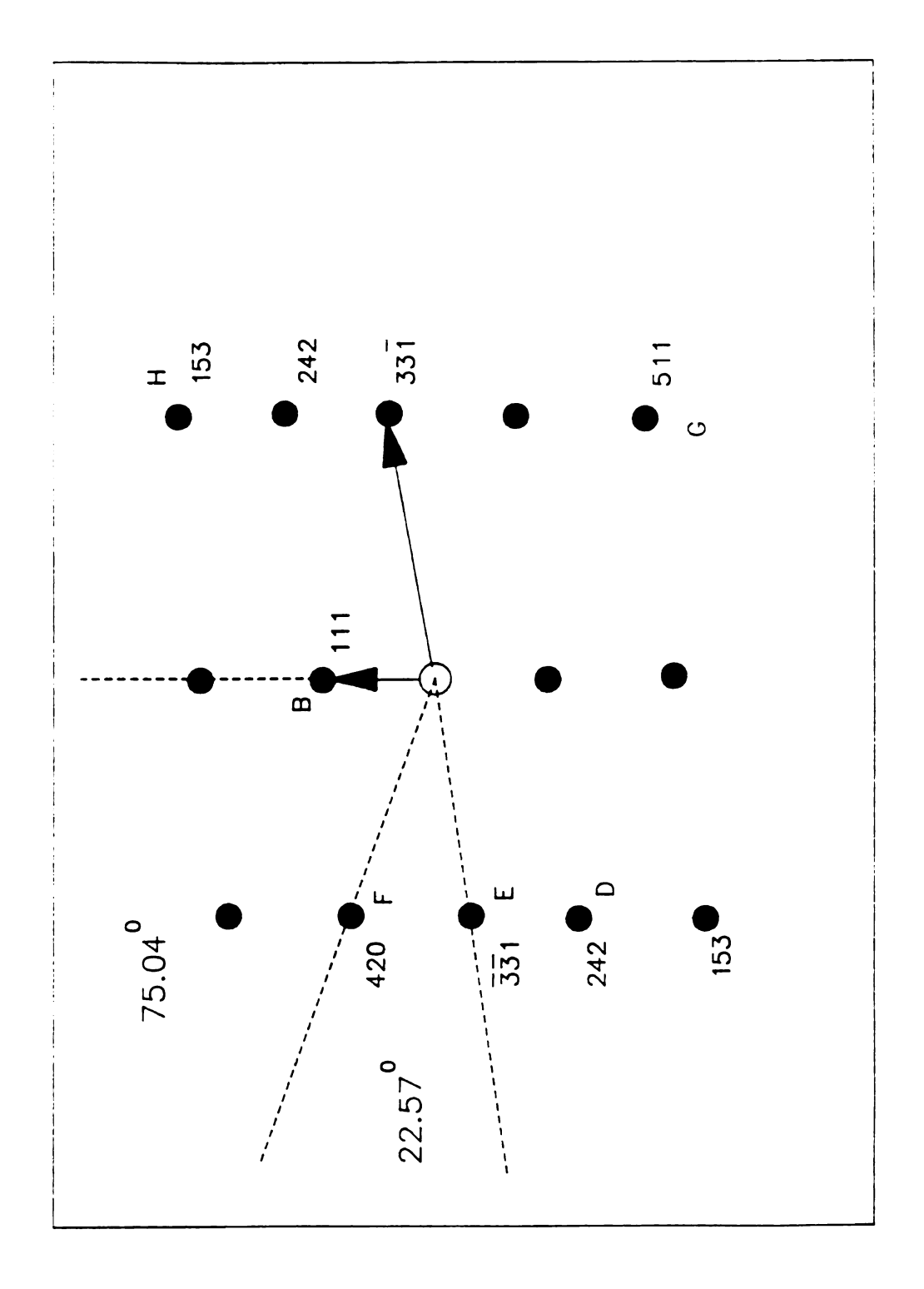


Figure 30. Monograph matching Ni:ZnS in Figure 24. [39]

3.5 HARDNESS

The range of the nickel-implanted layer prior to annealing was approximated by the "Profile" software to be 1104 angstroms, about a tenth of a micron. The depth of the Vickers indentor was calculated from the data and simple geometry (Vicker's indentor angle = 136 degrees) to be as high as 12 microns. Therefore, the hardness results represent values for the composite consisting of the nickel-irradiated ZnS and the untreated ZnS layer below. The change in hardness from unmodified to modified, and modifiedannealed specimens represent trends in the hardness of the irradiated surface alone. Though the depths of nickel or nickel sulfide phases were examined analytically and theoretically, the results were neither exhaustive nor conclusive. However, some evidence suggests that following the annealing, diffusion of such species away from the surface and into the bulk may have occurred. If this were the case, the Vickers measurements would more closely represent the hardness of the modified layer. Final hardness results were determined from data generated using the lowest available load on the Vickers indentor, thus, optimizing the results to best reflect the hardness attributable to conditions in the modified layer alone.

3.5.1 Nickel-Implanted Zinc Sulfide

Following the irradiation of zinc sulfide with nickel, the hardnesses of both modified and untreated specimens were measured by Vickers indents. Appendix A contains the Basic program which calculates hardness in GigaPascals (GPa), given the load used for indenting and the indent measurements in microns.

The initial hardness values determined for irradiated versus non-irradiated ZnS were 1.84 GPa and 1.77 GPa, respectively. The indentor load used was 1.0 kilograms-force and 14 indents were measured for each specimen. The standard deviations were +/- 0.051 for irradiated ZnS and +/- 0.055 for unmodified ZnS, while the coefficients of variation for each were 0.028 and 0.031, respectively. This small increase of about 4 percent, and the standard deviations for both values, appear to indicate that thermodynamic constraints typical of conventional processing did not significantly affect the "metastable" state of the implanted nickel. Cooling of the substrate during implantation by use of a chill block and liquid nitrogen flow may have been sufficient to permit only the action of implanting nickel ions into the sub-surface region of the ZnS. Once implanted, little thermally motivated activity occurred for, and between, the nickel, zinc, and sulfur atoms. Further confirmation of this can be seen from the hardnesses of irradiated and non-irradiated pre-anneal specimens which were determined using the decreased indentor load of 0.3 kilograms-force.

As discussed, the decrease in the indentor load resulted in hardness data more representative of the nickel-implanted layer. An average hardness of 1.77 GPa was calculated for three irradiated ZnS specimens from 4 indents per specimen with a load of 0.3 kilograms-force. The average of the standard deviations and coefficients of variation were +/- 0.062 and 0.035, respectively. The average hardness, standard deviation, and coefficient of variation for the three non-irradiated specimens were 1.75 GPa, +/- 0.067, and 0.038, respectively. These results are included in Table 10 with the post-anneal hardness data. (The raw data for all the hardness calculations are given in Appendix B).

3.5.2 Annealed Nickel-implanted ZnS

The Vickers hardness of three specimens of nickel-irradiated zinc sulfide were determined prior to, and following annealing to their respective peak temperatures of 750, 800, or 850 degrees celsius in a furnace chamber with a continuous flow of argon gas. The change in hardness for the irradiated and the control specimens of ZnS are shown in Table 10. All three of the control specimens experienced an increase in hardness of approximately 6.5 percent. The irradiated specimens exhibited larger increases in their Vickers hardness.

For the specimen annealed to 750 degrees celsius, the preand post-anneal hardnesses were 1.77 and 2.13 GPa, respectively.

This represents a 20.3 percent improvement. A 28.6 percent
increase was observed for the 800 degree profile specimen which
exhibited 1.75 and 2.25 Gpa pre- and post-anneal hardnesses. The
850 degree celsius anneal schedule resulted in a 24.4 percent
increase, from 1.80 to 2.24 GPa. The indent load used was 0.3
kilograms-force for 4 indents pre-anneal and 12 indents postanneal testing of each specimen.

The objective in the selection of profiles for annealing was to provide thermal energy to initiate the solid state of the nickel-irradiated ZnS to move towards thermodynamic equilibrium by assisting in overcoming diffusion barriers thus resulting in precipitation of nickel sulfide. The melting point of ZnS (sphalerite) has been estimated to be 1870 degrees celsius

although, it has been observed to transform to wurtzite at around 1000 degrees celsius under atmospheric pressure [26].

It would be advantageous to the performance of the modified ZnS surface if the precipitated metastable transformation toughener (NiS) was of minimal size, for this would maximize uniformity in the distribution of the precipitant and, therefore, in the surface modification effects. It was estimated that an homologous annealing temperature (based on the melting point of the ZnS bulk; 1830 degrees celsius) of 0.45 to 0.55 would be the most conducive to this end [38]. The maximum annealing temperatures were attained by heating as rapidly as possible, then cooling with an even greater thermal descent to achieve, in effect, a "quench" of the specimens undergoing thermal treatment. This too, was implemented to maintain control of the precipitant size.

Figure 17 illustrates the thermal profiles used in annealing as temperature versus time, in degrees celsius and minutes, respectively. It is apparant the slopes of these cycles are similar, both during heating and cooling of the specimens. The 750 celsius profile averaged a 36 degrees celsius per minute rise in temperature between 15 and 750 degrees celsius. The average heating rate for the 800 C profile was 34 degrees celsius per minute, and the 850 C target temperature was met with a 30 degree celsius per minute average increase in heating. The times to reach the target temperatures of 750, 800, and 850 degrees celsius were 32.5, 39.0, and 39.5 minutes, successively.

Similar uniformity in thermal influences were attained

for the average cooling rates from peak temperature to just over 100 degrees celsius. Each of these rates were within +/- 10 percent of the others. Uniform cooling rates near the beginning of the quench, where it is most critical, were maintained within +/- 2.5 percent for the rates from the peak temperatures to an average of about 360 degrees celsius.

The hardness values in Table 10 show that the irradiated ZnS experienced an average increase in hardness of approximately 25 percent, compared to a 7 percent approximate increase in the hardness of the non-irradiated zinc sulfide specimens. The highest average hardness value of 2.25 GPa was measured for the specimen annealed with the 800 degree profile. Figure 31 illustrates the changes in the hardness of both irradiated and non-irradiated ZnS specimens with their annealing temperatures. From this it can be seen that annealing to 800 degrees celsius provided the maximum increase in hardness. Annealing beyond this had little additional effect. The formation of NiS in the subsurface region by the annealing may have been limited by solubility constraints of nickel sulfide precipitants in the zinc sulfide matrix..

Figure 31 clearly indicates that an increase in the annealing temperature from ambient to 800 degrees celsius resulted in an increase in the Vickers hardness of the nickel-irradiated ZnS.

If the diffusion-barrier model is considered, one may anticipate no significant change in hardness with temperature followed by an abrupt increase in hardness, signifying attaining the thermal energy level necessary for the atomic "jump" across the barriers

to diffusion. This may be true if all the implanted nickel ions were resting in the same metastable energy state. However, due to the nature of the irradiation process, the atoms can be in various states of mobility and rest, depending on the defect type with which they were associated as well as their position with respect to the surface.

Therefore, the increase in hardness observed for the anneal at 750 degrees celsius is an indication that the proposed mechanism may have been initiated. If this is accurate, then 750 degrees celsius must be sufficient thermal energy to induce the diffusion of implanted nickel in zinc sulfide. It is likely that a concentration of nickel was present at ZnS grain boundaries prior to the annealing process, in the form of nickel sulfide and as nickel atoms. Grain boundaries are sites for nucleation and growth; processes which lower the free energy of the system. time required for diffusion of nickel atoms which are in the grains themselves but immediately adjacent to the grain boundaries would be less than for species further away, fully into the bulk of the zinc sulfide grains. This would result in an increase in hardness, as was observed for the 750 anneal, if the toughening phase precipitated to a certain minimum concentration in the subsurface region.

Annealing to a higher temperature or for a longer time would then allow additional diffusion from the bulk and precipitation to occur. However, it follows that those grains which precipitated first would continue to grow at the expense of other newly precipitating nucleation sites. Since a fine grain

size is desired for optimum uniformity and distribution of the toughening phase, the time of anneal can be minimized while increasing the utilization of precipitating species by increasing the anneal temperature. Additionally, a finer grain size may be obtained by a fast rate of heating which results in the formation of more nucleation sites. The further increase in hardness observed for the 800 degree celsius anneal may be due to an increase in concentration of the toughening nickel-sulfide precipitants, with grain sizes still kept at a minimum by minimizing the time at temperature.

Through thermal elevation, nickel sulfide in the hexagonal form (α -hi temp) enters the liquid state at approximately 995 degrees celsius and experiences a phase change to β -NiS (millerite) upon cooling to around 380 degrees celsius. A change to β -NiS is reported to exhibit a positive change in volume of approximately 4 percent [26]. This was the apparant increase in hardness determined for ZnS after the implantation procedure.

Table 10. Vickers hardness data for nickel-irradiated and non-irradiated ZnS pre- and post-anneal.

	NON-IRRADIATED			<u>IRRADIATED</u>			
Anneal <pre>Temp (C)</pre>	Hardness _(GPa)	+/-	<u>CFV</u>	Hardness (GPa)	<u>+/-</u>	<u>CFV</u>	
pre	1.75	.058	.033	1.77	.037	.021	
750	1.85	.046	.025	2.13	.073	.034	
pre	1.77	.065	.037	1.75	.050	.028	
800	1.88	.084	.045	2.25	.095	.042	
pre	1.74	.077	.045	1.80	.099	.055	
850	1.88	.079	.042	2.24	.095	.042	

CFV = coefficient of variation

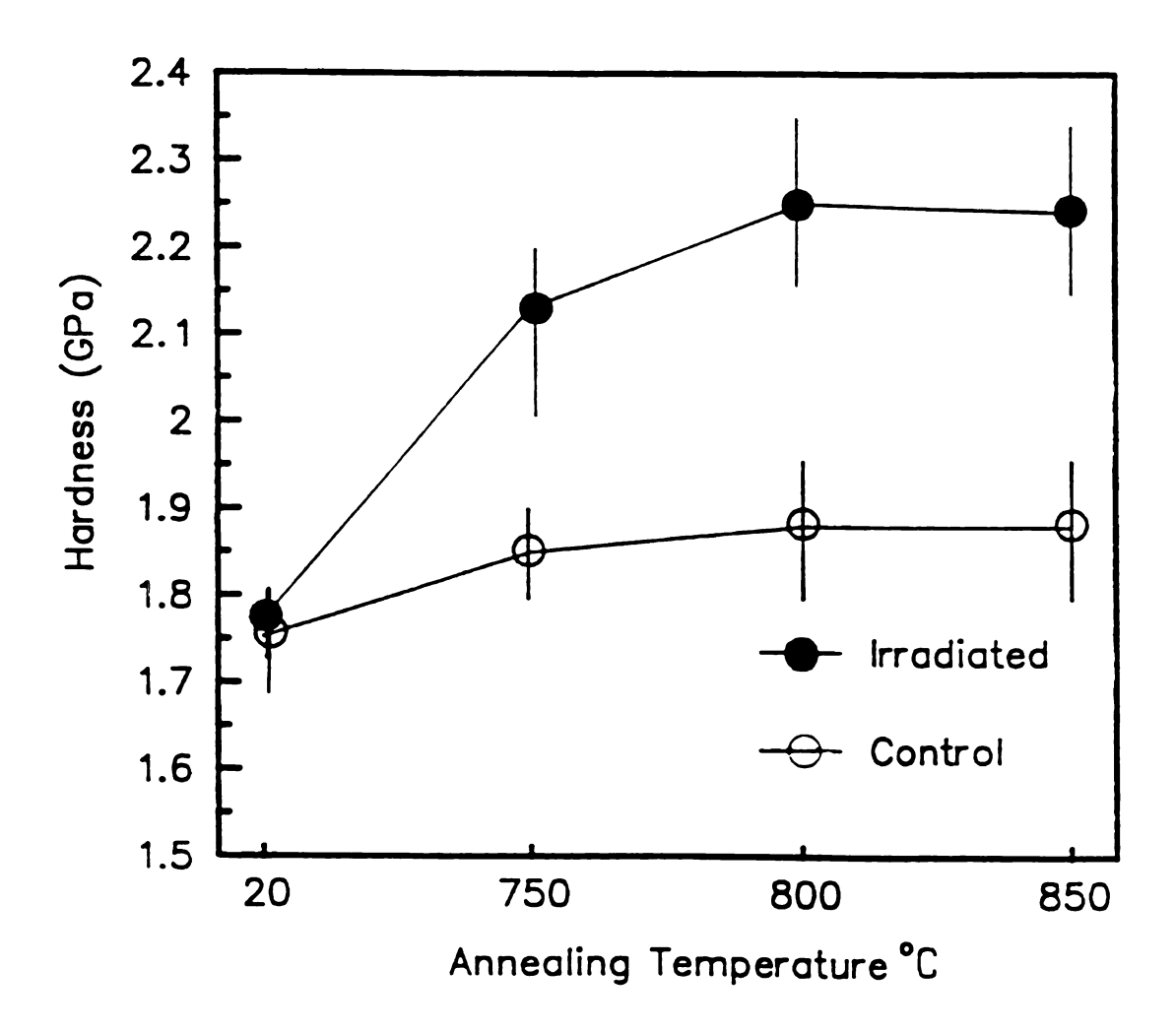


Figure 31. Increase in Vickers hardness for 200keV Ni-irradiated ZnS and control samples with annealing.

3.6 SCANNING ELECTRON MICROSCOPY

A non-irradiated specimen of zinc sulfide annealed with the 750 degrees celsius schedule (see 2.5.2) was analyzed using SEM and EDX. Percents, by weight, of the zinc and sulfer were 78.58 and 21.30, respectively. Trace amounts of various elements were attributed to contamination by the conductive paint, the aluminum base, and handling. No trace of nickel was found.

Figure 32 is a micrograph of the non-irradiated ZnS surface at a magnification of 1100. Evidence of grain "pullout" can by seen by the presence of voids in the surface which appear to be greater than or equal to 2.0 microns.

Voids similar to those in Figure 32 appeared relatively uniformly distributed with spacings of approximatley 20 to 30 microns. Figure 33 shows the voids at a higher magnification (x3300). The surface of other grains canbe seen at the bottom of these shallow voids.

A nickel concentration of 1.61 weight percent (1.24 atomic percent) was found for a specimen of nickel-implanted zinc sulfide prior to annealing. Small voids, or "micropores" were observed in the surface before annealing. As shown in Figure 34, these pores appear to be different from the voids in Figure 33 in that no grain surfaces could be seen at the bottom, thus giving them the appearance of a deep pore, or pit. Sizes averaged 1.0 micron or greater, and the distribution was also relatively uniform, with a pore spacing of about 15 to 25 microns. This may be evidence of surface damage caused by irradiation.

Following annealing to 750 degrees celsius of the irradiated ZnS, the concentration of nickel as determined by EDX decreased to 0.42 weight percent at the surface of a Vickers indentation, and 0.32 weight percent at the specimen surface. This may represent a qualitative indication of nickel diffusion further into the bulk of the ZnS. Figure 35 is a scanning electron micrograph of the post-annealed irradiated ZnS.

Several observations can be made by commparison of Figure 35 with Figure 34. First, the "pitting" seen in the pre-anneal specimen is not evident following the anneal. This may be due to a thermal surface healing phenomenon, or may be less apparant simply due to the increased contrast of the grain boundaries following the thermal cycle. This leads to a second observation, the appearance of an "etching" effect resulting in the enhanced contrast seen in Figure 35. Grain-boundary definition appears to be an artifact of the thermal exposure during annealing of the specimen. Finally, the grain size of zinc sulfide for the various specimens subjected to annealing did not change appreciably. The average size regardless of processing was approximated to be 5 microns.

Figure 36 shows the nickel-irradiated ZnS following the anneal to 850 degrees celsius. AGain, no appreciable change in grain size is observed, and the "etching" effect is enhanced. However, the weight percent of nickel decreased further, from the levels for the non-annealed and 750-annealed specimens, to a concentration too low for detection by the EDX system. This was true regardless of variation in the detector angle. The annealing

temperature of 850 degrees celsius also represented the peak anneal at which improvement in hardness of the modified zinc sulfide appeared to level off. These two results, though preliminary, indicate that the nickel ions implanted into the zinc sulfide surface diffused away from the surface between the temperatures of 750 and 850 degrees celsius.

The TEM results show evidence that various nickel sulfide phases were present in the irradiated ZnS surface region. Theough the elctron diffraction results came from irradiated ZnS not subjected to annealing, the effects of ion milling and electron beam heating may ahve been sufficient to initiate diffusion of the implanted nickel and subsequent association and precipitation of nickel sulfide particles.

Regarding the quantitative EDX data generated for nickel in the ZnS, the relative weight percents determined for the nickel were below the tolerance for EDX, which is generally approximated as around plus or minus 3 to 5 percent, depending on the system in use. In spite of this, nickel was detected and measured where it was known to be present, and the various concentrations followed a qualitative trend consistent with observed annealing behavior for various implanted species [8,18,23].

There may be a correlation between the improvement in hardness of the irradiated ZnS and the extent of nickel diffusion/dispersion away from the sub-surface region of the zinc sulfide. Auger analysis may be used to further understand the diffusion behavior of nickel in ZnS with annealing.

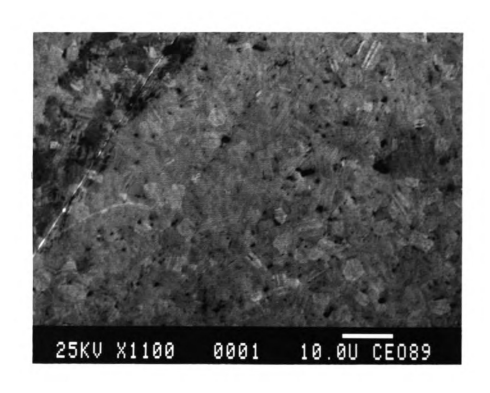


Figure 32. Scanning electron micrograph of zinc sulfide. (Mag:1100)

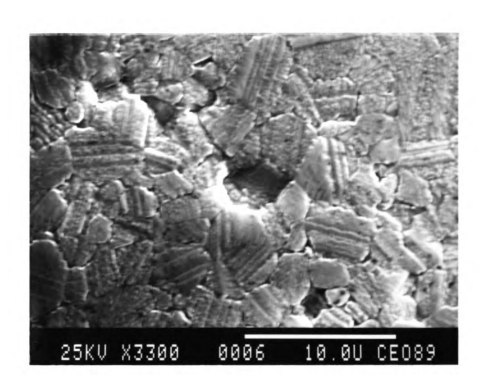


Figure 33. Scanning electron micrograph of zinc sulfide surface "voids." (Mag:3300)

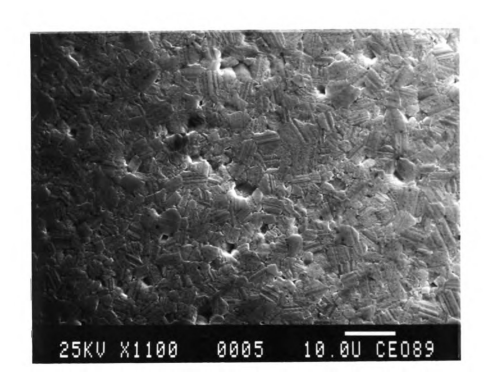


Figure 34. Scanning electron micrograph of 200keV Ni-irradiated ZnS. (Mag:1100)

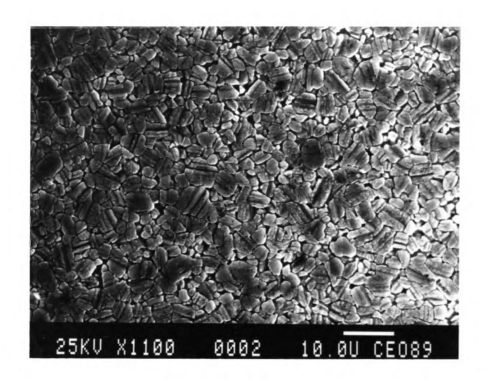


Figure 35. Scanning electron micrograph of Ni-irradiated ZnS annealed to 750 degrees celsius. (Mag:1100)

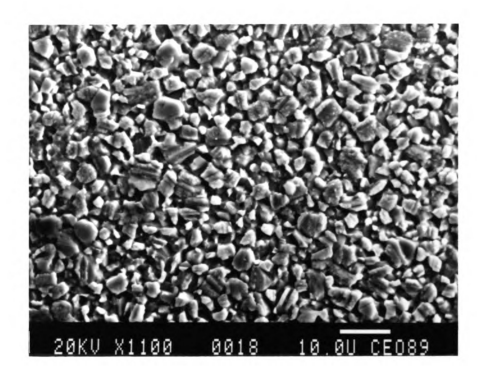


Figure 36. Scanning electron micrograph of Ni-irradiated ZnS annealed to 850 degrees celsius. (Mag:1100)

3.7 X-RAY PHOTOELECTRON SPECTROMETRY

Figure 37 shows the XPS spectrum for ZnS irradiated with nickel ions at 200 keV with a fluence of 1x10¹⁷ ions/cm². Peaks were found which correlate to the inner-electron binding energies for zinc and sulfur, respectively. These energies are listed in Table 11 along with those that correlate to the compounds of nickel-sulfide and zinc-sulfide. For those electron energies indicating the presence of a compound, the element of that compound to which the electron is associated is given in parenthesis. Peaks which resulted from Auger, rather than inner shell electron ejections are labeled in the spectrums, as are some of the various electron levels. (Auger electrons are those electrons which are ejected in response to the charge imbalance created by the absence of an inner-shell electron). A small nickel peak is also present in Figure 37 at a binding energy of 855.0 electron-volts. This is shown enlarged in Figure 38.

The carbon peak in Figure 37 was not present in the spectrum after minimal sputtering of the specimen surface. Additional sputtering of the specimen surface followed by analysis was conducted, until approximately 50 nanometers of the top surface were removed. The peak indicating the presence of nickel increased very little in height and area, even up to 50 nanometers in depth. Atomic concentration of the nickel at this depth was measured to be 3.75 percent. However, the sensitivity of the spectrometer for such a low concentration makes this value a rough

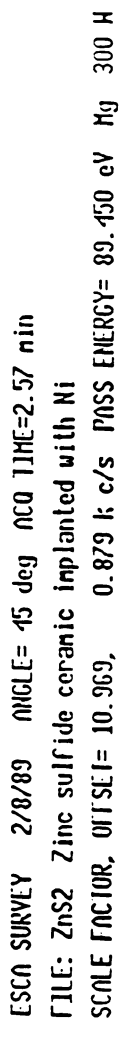
approximation. The computer generated data of the "Profile" software calculated the concentration at this depth to be approximately 7.0 atomic percent.

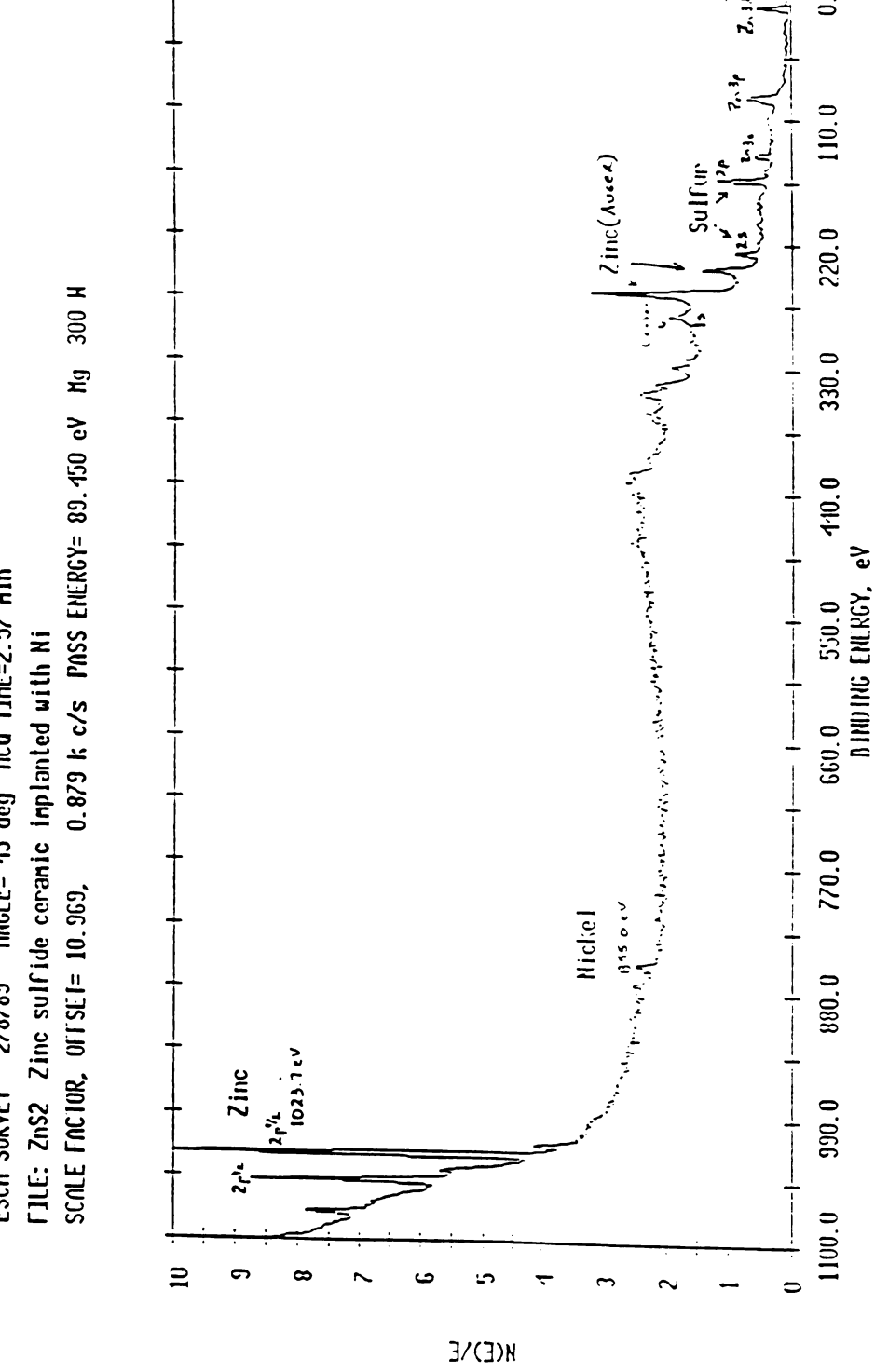
The binding energy for a 2p level electron of sulfur, if the sulfur is associated with nickel, is 162.2 electron-volts. The sulfur peak in Figure 39, corrected by 2.0 electron-volts (an instrument calibration) had a binding energy of 162.0 electron-volts; a reasonable correlation to 162.2 eV. This indicates that nickel-sulfur bonds were present in the ZnS specimen prior to the annealing operations.

The XPS spectrum of nickel-irradiated ZnS annealed to 800 degree celsius is given in Figure 40. There was neither an indication of nickel in the spectrum nor an increase in the nickel-sulfur bond peaks. Additionally, nickel peaks were not found after sputtering the specimen surface up to 100 nanometers, the theoretical range for the pre-annealed implanted nickel. The high level of diffusion associated with nickel is considered to be the primary reason for this result. Two oxygen peaks were removed following sputtering while all other features in Figure 40 remained unchanged.

Table 11. Binding energies of nickel, zinc, and sulfur,

<u>Ni</u>	NiS	ZnS	<u>Zn</u>	
857.7	162.2 (S)	164.0 (S)	1021.8	
	855.1 (Ni)	1022 (Zn)		





X-Ray photoelectron spectrum of 200keV nickel-irradiated zinc sulfide. Figure 37.

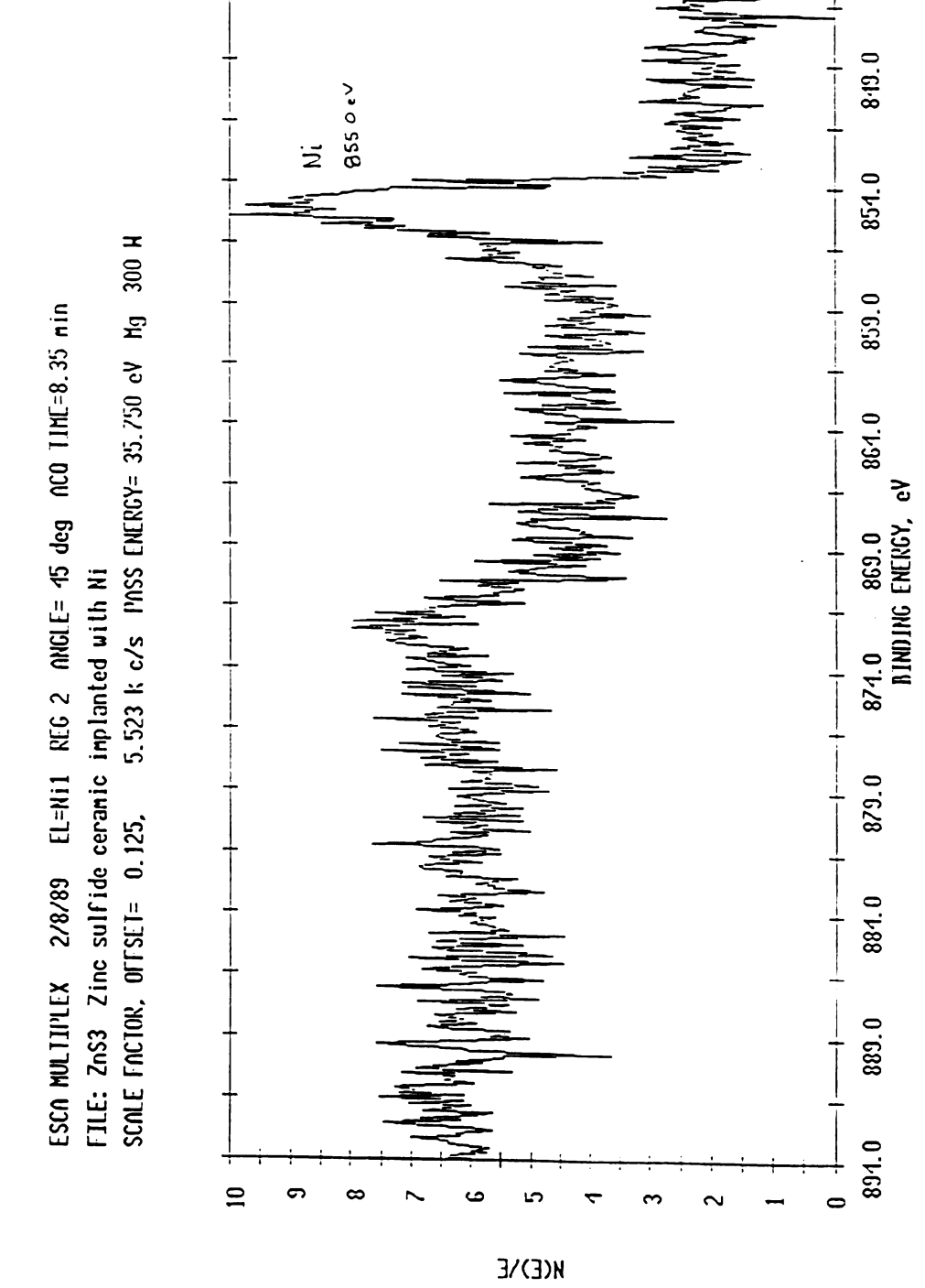


Figure 38. X-Ray photoelectron spectrum of 200keV nickel-irradiated zinc sulfide in region of nickel peak.

8-11.0

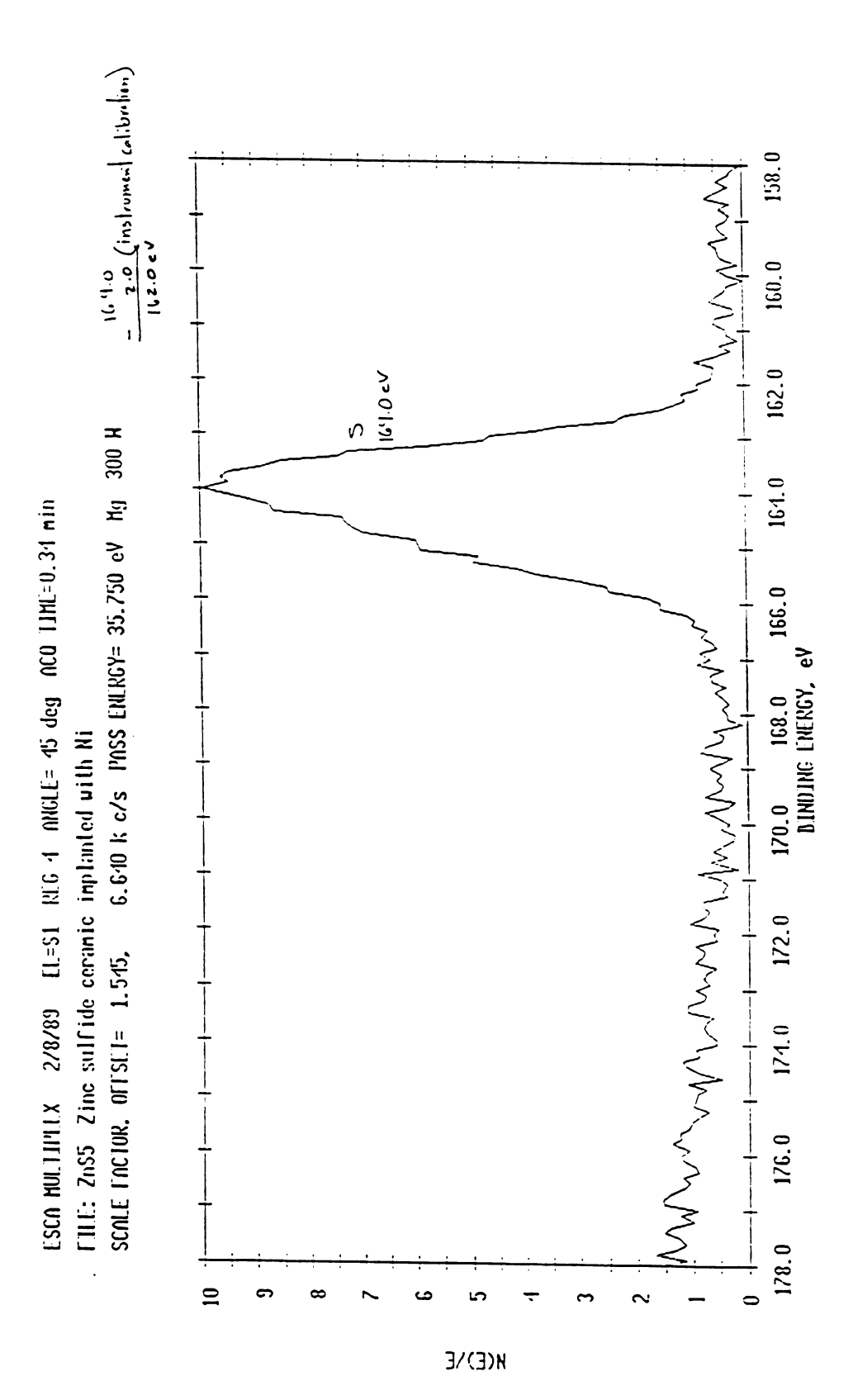
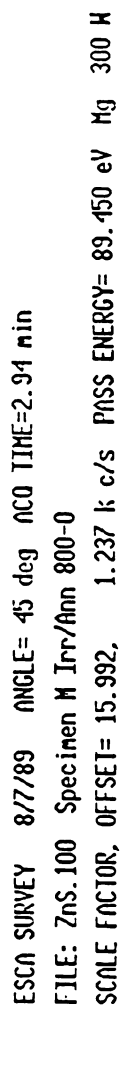


Figure 39. X-Ray photoelectron spectrum of 200keV nickel-irradiated zinc sulfide in region of sulfur peak.



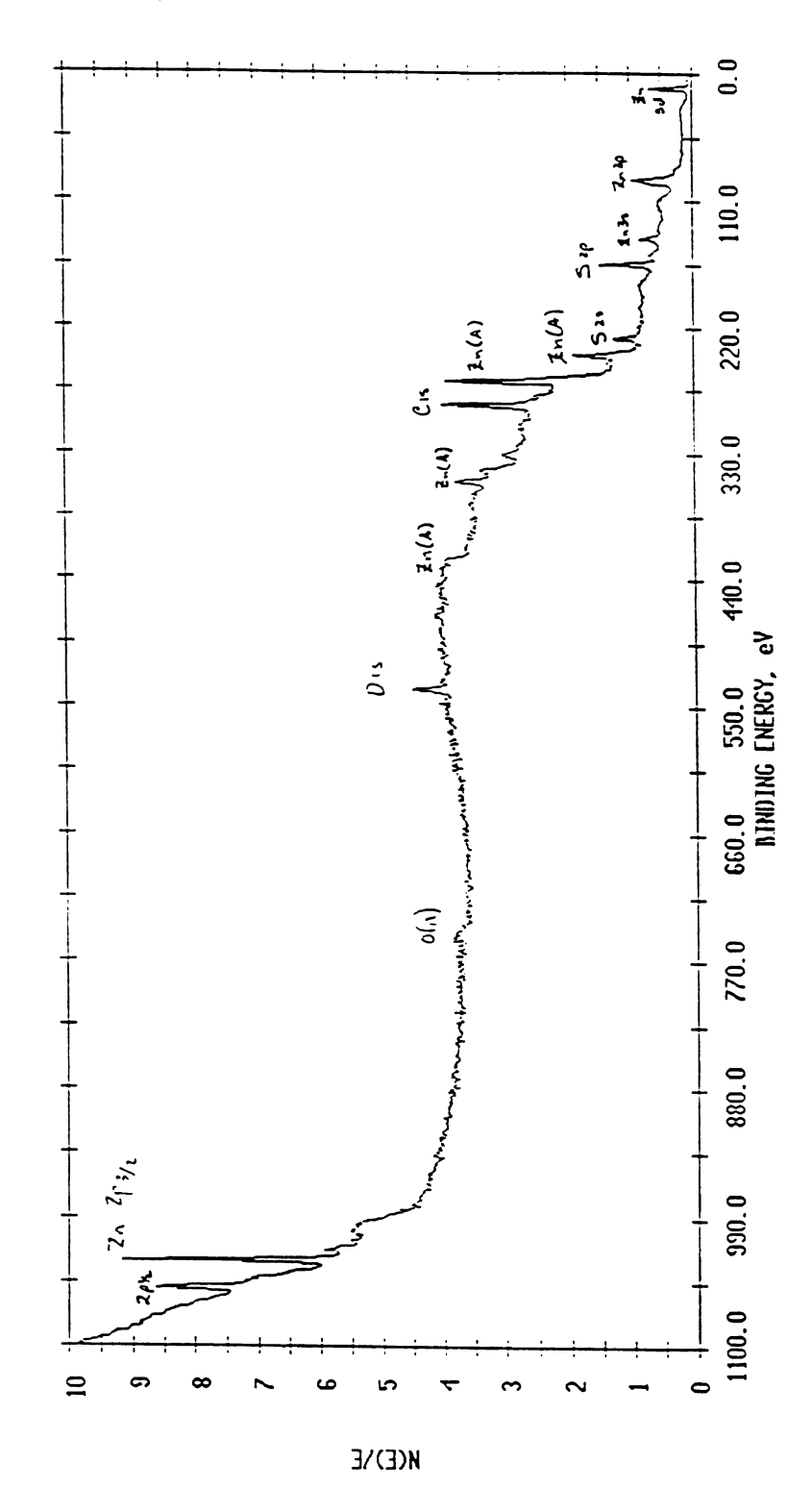


Figure 40. X-Ray photoelectron spectrum of 200keV nickel-irradiated zinc sulfide annealed to 800 degrees celsius.

3.8 DIFFUSION

Figure 41 is a plot of the implanted nickel as determined by the software "Profile Code" developed by Implant Sciences Corporation, Danvers, MA. The concentration profile was calculated given the incident and target material data, as well as the implantation specifications. Figure 41 indicates the range of the nickel irradiated into ZnS to be 1105 angstroms, or 110 nanometers. The atomic concentration at this depth was 8.9×10^{21} nickel atoms/cm³. This maximum concentration is also given as approximately 17 atomic percent. This result comes from dividing the range concentration of nickel into the atomic concentration of ZnS $(5.23 \times 10^{22} \text{ atoms/cm}^3)$. The maximum depth of the implanted nickel was determined to be approximately 240 nanometers.

Also from Figure 41, the concentration of nickel at the surface can be estimated as a few atomic percent. This is consistent with the pre-anneal XPS concentration result of 3.75 atomic percent nickel. SEM/EDX measurements detected only 1.24 atomic percent. For such a low concentration, it is likely that even a small difference in the XPS and EDX measurement volumes could result in this difference.

While all of these values reflect the modeling of the implantation results, and represent a useful qualitative approximation, other mechanisms may have affected the true nickel profile. Through the implantation process, radiation damage results in a greater concentration of vacancies in the region of irradiation. The maximum concentration of vacancies would most

likely lie between the surface and the region where most of the nickel ions come to rest, ie. the range. For each nickel ion, there exists a "collision cascade," which was initially discussed in Section 1.2. This cascade is the corridor of damage remaining in the path of each ion after it has traveled through the atomic system dissipating its kinetic energy by collisions with other atomic species.

As is true for the nickel atoms, radiation damage may also result in a vacancy concentration which exceeds the equilibrium solubility concentration in the atomic matrix. This condition results in non-equilibrium concentration gradients. The driving force for vacancies to move across such a gradient are the sudden atomic changes occurring within the bombarded atomic structure. Therefore, such a vacancy flux may be active during or shortly following the irradiation process.

Diffusion of implanted nickel atoms may also occur, for the vacancy flux is operative in proximity to the implanted species. These atoms move in the direction opposite to the movement of a vacant site and result in non-equilibrium concentration gradients. The local changes in composition may induce precipitation of a second phase at sites of nucleation. This phenomenom of "radiation-induced segregation" is activated independent of thermal energy, and may be the mechanism responsible for the formation of the nickle-sulfide precipitants observed in Figure 23.

The movement of nickel atoms by the vacancy mechanism of diffusion could result in zinc vacancies being filled by nickel

atoms, and subsequent bonding of the nickel to adjacent sulfur atoms. The concentration of zinc vacancies is also believed to be higher than that of sulfur due to their relative displacement energies within a crystal of ZnS. During the ion implantation process, sulfur atoms require 15 to 20 electron-volts of energy transferred to them to be displaced from their atomic positions, whereas zinc need only absorb 7 to 9 electron-volts to become dislodged from their atomic positions [42].

Thermally assisted atomic motion may have commenced with the minimal beam heating of the ion milling procedure and the TEM studies. The result of this energy application on the conditions described above may have been sufficient to result in additional nickel-sulfide embryo formation leading to the precipitation transformation reaction described in Section 1.2 (p.7).

Radiation-induced segregation moves a structure away from an equilibrium state. Therefore, following irradiation, conditions are highly-conducive to the diffusion of species due to the excess number of defects in the metastable energy state. This radiation-enhanced diffusion, being thermally activated, drives the energy state of the matrix closer to a state of equilibrium.

Section 3.4 includes TEM observations of precipitants in the implanted ZnS. The corresponding selected-area diffraction pattern included very fine crystalline rings, indexed to be those of one or more phase of nickel sulfide. Their presence in the absence of the annealing procedures strongly suggest that one or more of the mechanims discussed here may have been active prior to heat treatment of the irradiated samples. It should be noted from

Table 9, the indications that the low-temperature stable phase of β -NiS may have been present in greater concentration in the preannealed samples than the precipitants of the meta-stable, high-temperature phase, α -NiS. This outcome may be due to the relative dominance of the two radiation-assisted diffusion mechanisms of radiation-induced segregation and radiation-enhanced diffusion. It may also be relevant to the 5 percent increase in hardness measured for the pre-anneal samples.

During ion implanation, RIS may have been more active than RED for several reasons. Due to the relatively high dose with which nickel ions were implanted into zinc sulfide, a higher concentration of vacancies would be generated and able to contribute to the radiation-induced segregation mechanism.

Additionally, the zinc sulfide was maintained at a relatively low temperature during implantation, therefore the temperature-dependent RED activity was suspected of being mimimal at that point.

The procedures and results of annealing nickel-irradiated ZnS to temperature of 750, 800, and 850 degrees celsius in an argon environment were presented in Sections 2.5 and 3.5, respectively. The Vicker's hardness was shown to improve after annealing.

Complete analyses was not performed to determine the actual nickel profile following the heat treatment cycles. However, attempts by XPS to find nickel at the surface in the ZnS following the 800 degrees anneal were unsuccessful. The surface was then sputtered to a depth of 100 nanometers, approximately the pre-anneal range of the implanted nickel ions. Nickel was not detected by XPS even

at this depth. This result is consistent with the high diffusivities which have been associated with nickel, even with a moderate elevation in temperature. Although specific data was not cited, Woodbury attested to the high diffusivity of nickel in zinc sulfide in a commentary on work conducted by Pappalardo and Dietz [43].

From [44], nickel and sulfur combined in a 1:1 ratio were found to produce α -NiS in a temperature range of 400 to 900 degrees celsius. The corresponding range of time for this product to form was between 4 and 168 hours. Assuming the minimum temperature for the α -NiS reaction as 400 degrees celsius, the thermal profiles in Figure 18 show the time duration above this temperature for each anneal cycle. The time above 400 degrees for the 750 degree anneal was 600 seconds, while the 800 and 850 degree anneals were above 400 degrees for 1,080 seconds. The heat treatment durations for nickel-irradiated zinc sulfide were much less than the time for the α -NiS annealing in [44]. However, the highly metastable conditions within the sub-surface region of the irradiated ZnS represented a state of enhanced diffusivity.

The self-diffusivity of nickel can be calculated from the experimentally determined diffusion equation:

$$D = D_{o} \exp(-Q/RT)$$
 (7)

where, D = diffusion coefficient, of diffusivity, cm^2/sec

 D_o = material dependent factor, cm²/sec

Q = activation energy, kilo-Joules/mole

R = 8.314 Joules/mole-Kelvin

T = temperature, Kelvin [44].

 $\rm D_o$ and Q for the self-diffusivity of nickel are 1.5 and 283.0 kilo-Joules/mole, respectively [44]. The following diffusivities for nickel were calculated using the anneal temperatures for the nickel-irradiated ZnS:

 $D_1(1023K) = 5.315x10^{-15} \text{ cm}^2/\text{sec}$

 $D_2(1073K) = 2.505x10^{-14} cm^2/sec$

 $D_3(1123K) = 1.029x10^{-13} cm_2/sec$

These values are approximations and serve more to highlight the change from 1023K to 1123K. The increase from D_1 to D_2 is greater than that from D_2 to D_3 . This correlates to the increase in hardness observed for the annealed specimens, illustrated in Figure 31. The actual diffusivities may be significantly higher than those calculated. Self-diffusivity is a measure of diffusion of a species within itself. The melting point of nickel is 1453 degrees celsius, therefore, the bond-energy between nickel atoms is significant. This bond-energy would be less for nickel atoms surrounded by zinc and sulfur atoms. And again, a condition of

the highly metastable environment created by ion implantation is one of enhanced mobility

Nickel sulfide formed in the subsurface region of the ZnS may have diffused to depths much greater than the range during the annealing procedure. Due to the depth of the indents made by the Vicker's hardness tester, it was originally stated that the resulting hardness values represented those of a composite consisting of the thin implanted layer and the unmodified bulk. If NiS did in fact diffuse to significant depths away from the surface, as is eluded to by the failure of XPS to detect nickel at the range depth, then the increase in Vicker's hardness observed for the annealed samples more closely represents the hardness improvements for the modified layer of the ZnS. This increases the sensitivity of the Vicker's indentor to changes exhibited by the presence of nickel sulfide, i.e. a positive change in volume present from the α -> β phase transformation induced by the energy from the indentor during the hardness test.

To estimate the nickel concentration after annealing at a certain depth, several models may be develop after the diffusion couple or thin-film solutions to Fick's Second Law for Diffusion [45]. Auger analyses of annealed specimens would also provide empirical data for understanding the diffusion behavior of nickel in the ZnS structure.

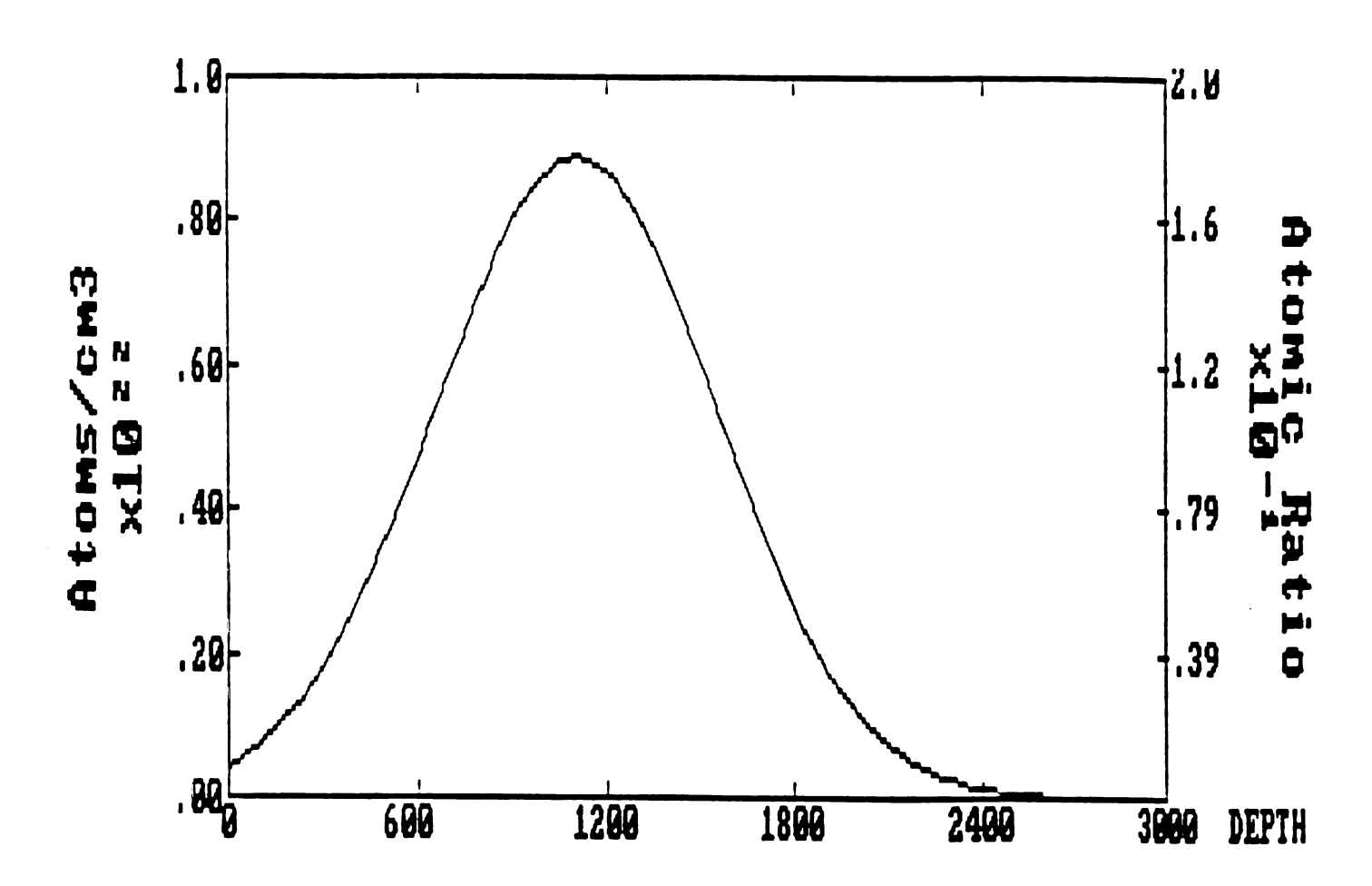


Figure 41. Distribution of 200keV nickel ions implanted into zinc sulfide.

CHAPTER 4. CONCLUSION

Zinc sulfide, an infrared transmitting ceramic, was ion implanted with a dose of 10^{17} nickel ions/cm² at 200 keV under a controlled atmosphere of argon, with the surface temperature retained below 200 degrees celsius.

The specimens were then prepared for scanning electron and transmission electron microscopic evaluations, surface hardness and fracture toughness measurements, elemental analyses by x-ray photoelectron spectroscopy, and x-ray diffraction.

Evaluation of the mechanical properties was conducted on samples before and after heat treatments to assess the effect that annealing may have on facilitating nickel diffusion and precipitation of nickel sulfide, believed to be a metastable transformation toughener.

The presence of nickel and any precipitants forming in the implanted substrate was investigated by transmission electron microscopy in selected-area diffraction mode. Zinc sulfide was used as the internal standard by which the diffraction pattern measurements were calibrated. This work revealed various nickel sulfide phases in the subsurface region of the implanted ZnS.

Motivation for this work followed the supposition by W.M.

Kriven that nickel sulfide possesses the attributes of a stressinduced transformation toughener. Implantation of nickel into
zinc sulfide, followed by thermal treatment, may induce the lower
volume metastable NiS phase to form in the subsurface region.

Upon the application of energy in the form of impact with an accelerating force, this phase is believed to transform to a more stable phase of NiS that requires a greater volume within the matrix. This volume increase would then establish a compressive stress in the surface region, thereby increasing the surface's resistance to impact damage.

Transmission electron microscope diffraction patterns of nickel-implanted zinc sulfide revealed both α and β nickel-sulfide phases as precipitants, as well as NiS_2 . Precipitant sizes were measured to be approximately 5 to 10 nanometers, thereby being coherent in the matrix of zinc sulfide grains determined to be approximately 5 microns. Beam heating may have induced initial precipitant growth prior to annealing. Additional growth with heat treatment may have produced precipitants semi-coherent with respect to the matrix.

The average increase in hardness observed for annealed nickel-implanted zinc sulfide as compared to unmodified zinc sulfide was approximately 25 percent. This has been attributed to the presence and action of metastable $\alpha\textsc{-NiS}$ in the subsurface region of the ZnS. This phase of NiS undergoes a positive change in volume when transformed to $\beta\textsc{-NiS}$. It is suggested that transformation may have been induced by stresses associated with the impact of the Vicker's hardness indentor. As the energy propagated through the surface region, the atoms of a fine distribution of metastable $\alpha\textsc{-NiS}$ phases absorbed sufficient energy to displace their positions to the lower energy arrangement of $\beta\textsc{-NiS}$. This represents an increased resistance to surface

damage which may then be sustained further in the region of impact by the presence of a residual surface compressive stress due to the volume increase. Additional "shielding" from crack propagation is established by the semi-coherency of β -NiS precipitants which constrain the ZnS matrix.

There was no significant change observed on the grain size of the zinc sulfide following the annealing procedures, although there was a small increase in hardness observed for control samples of zinc sulfide. Certain measures were taken to minimize possible contamination of the control by volatilized species in the annealing chamber, however, this may be the cause for the increase in hardness of the control samples. The ion implanted nickel was determined by x-ray photoelectron spectroscopy to have diffused further into the bulk away from the pre-anneal range of 1100 angstroms presumably by the vacancy mechanism of diffusion. XPS also measured the presence of both nickel and sulfur, in pre-anneal specimens, with binding energies indicative of nickel-sulfer bonds.

A preliminary evaluation on the refractive index of zinc sulfide by Fourier Transform Infra-Red spectroscopy indicated that the ion implantation of nickel in the surface region of the ZnS resulted in no observable degradation. A change in refractive index for a material is dependent upon changes in polarization, absorption, and volume. Although the phase change from α to β nickel sulfide results in a 4 percent increase in volume, the relative increase for the entire bulk material of ZnS would be negligible.

Primary sources of error in this work may potentially lie in the camera constant calibration and selected-area diffraction beam calibrations, as well as measurement errors on the SAD diffraction patterns. The load used for Vickers hardness measurements was too high to measure the hardness increase for the modified layer alone. The post-anneal composite hardness did show an increase, however, it would be difficult to extrapolate a hardness for the modified layer from this data.

Additional work of interest would include investigating the depth profile and diffusion behavior of nickel by XPS or Auger Electron Spectroscopy in the post-annealed samples. Selected-area diffraction patterns of irradiated and annealed specimens would allow indexing the final precipitants and their sizes.

Additionally, microhardness measurements may be more representative of the modified surface alone, rather than the composite. Micro-micro diffraction of a single precipitant would provide detail regarding the nature, size, and orientation of precipitants in the subsurface region of an implanted target material while in-situ annealing in a transmission electron microscope would reveal information about the precipitation process.



APPENDIX A VICKERS INDENT HARDNESS DATA

APPENDIX A

VICKERS INDENT HARDNESS DATA

For specimen ZnS spec.X non-irr, annealed test Indented on 7-24-89

Indent 1 2 3 4 5 6 7	Load(kg) 0.30 0.30 0.30 0.30 0.30 0.30	a1 (um) 53.00 53.20 51.90 52.80 52.90 55.80 55.70	a2(um) 55.10 54.70 53.10 54.00 54.30 52.30 55.50	C1 (um) C.00 C.00 C.00 C.00 C.00 C.00	C.00 C.00 C.00 C.00 C.00 C.00
8	0.30	52.40	53.40	0.00	C.00 C.00
9 10	0.30	51.90 54.00	52.40 59.00	0.00	C.00 C.00
11 12 Break in	0.30 0.30 4600	52.70 51.90	55.30 57.50	0.00 C.00	0.00 C.00

break in 4600 Ok

Indent	Amean(m)	Cmean(m)	Hard(GPa)	<pre>Kic(MPam1/2)</pre>
1	27.025E-06	0.000E+00	0.187E+01	U.UUUUE+00
2	26.975E-06	0.000E+00	0.187E+01	C.0000E+00
3	26.250E-06	0.000E+00	0.198E+01	0.0000E+00
4	26.700E-06	0.000E+00	0.191E+01	C.0000E+00
5	26.800E-06	0.000E+00	0.190E+01	0.0000E+00
6	27.025E-06	0.000E+00	0.187E+01	0.0000E+00
7	27.800E-06	0.000E+00	0.177E+01	0.0000E+00
8	26.450E-06	0.000E+00	0.195E+01	0.0000E+00
9	26.075E-06	0.000E+00	0.201E+01	0.0000E+00
10	28.250E-06	0.000E+00	0.171E+01	C.0000E+00
11	27.000E-06	0.000E+00	0.187E+01	C.0000E+00
12	27.350E-06	0.000E+00	0.182E+01	C.0000E+00

Mean hardness +/- std = 1.877393 8.427361E-02 Coefficient of variation for hardness = 4.488865E-02

Mean Kic +/- std = Coefficient of variation for Kic =

```
For specimen ZnS spec.X not irr pre-anneal test
Indented on 7-24-89
                        Load (kg. al:um) al:um cl um c
 lndent
Ereak in 4600
                           Amean(m) Cmean(m) Hard(GFa) K10(MFam1/2)
27.875E-06 0.000E+00 0.176E+01 0.0000E+00
27.175E-06 0.000E+00 0.185E+01 0.0000E+00
28.375E-06 0.000E+00 0.169E+01 0.0000E+00
27.525E-06 0.000E+00 0.180E+01 0.0000E+00
Indent
Mean Kic +/- std =
                                                                                                    C
  Coefficient of variation for Kic = 0
 For specimen ZnS spec.M irr. pre-anneal test
 Indented on 7-24-89
 Indent Load(kg) a1(um) a2(um)
                                                                                                                                c1 (um)
                                                                                                                                                                   c2 (um)
                                 0.30 55.40 56.50 C.00

0.30 56.70 56.20 C.00

0.30 53.90 55.50 C.00

0.30 56.10 56.30 C.00
                                                                                                                                                                         0.00
              2
                                                                                                                                                                        C.30
C.30
              3
Break in 4600
 For specimen ZnS spec.M irr. pre-anneal test
 Indented on 7-24-89
                       Indent
     1
Mean hardness +/- std = 1.751702 4.960323E-02
   Coefficient of variation for hardness = 1.831717E-02
Mean Kic +/- std =
    Coefficient of variation for Kic = 0
```

```
For specimen 2nS spec.Z annealed 750-0
Indented on 8-10-89
Indent
        Load(kg)
                 al(um) a2(um)
                                  cl(um)
                                           117.00
                                   157.80
  1
         0.30
                 53.40
                         53.10
                                             86.60
          0.30
                  54.40
                           55.10
                                   104.60
                                             111.50
   3
         0.30
                 54.70
                          55.30
                                    116.00
                                    122.70
         0.30
                 55.40
                          55.00
                                  107.90
                                             138.70
         0.30
                 53.00
                          54.90
         0.30
                 53.80
                          54.40
                                   148.30
                                             109.50
   ć
                                   139.60
         0.30
                 55.20
                                             116.00
                          55.40
                                   134.40
   8
         0.30
                 54.30
                          53.70
                                             96.00
   9
                                   118.10
                                             113.00
         0.30
                 54.60
                          53.60
   10
                                   109.00
                                            106.76
         0.30
                 54.10
                          55.90
                                   111.90
                                             88.00
         0.30
                 54.00
                          53.30
   12
                 52.90 54.70 115.00
                                             106.76
         0.30
Ereak in 4600
ЭK
                   0.000E+00 0.187E+01
        27.025E-06
                                            C.0000E+00
        26.975E-06
                    0.000E+00 0.187E+01
                                            C.0000E+00
  3
       26.250E-06
                   0.000E+00 0.198E+01
                                            C.0000E+00
                                            C.0000E+00
  4
       26.700E-06
                    0.000E+00
                              0.191E+01
  5
       26.800E-06
                   C.000E+00
                                            C.0000E-00
                               0.190E+01
       27.025E-06
                   0.000E+00 0.187E+01
                                            C.0000E+00
                                            C.0000E+00
                   0.000E+00 0.177E+01
       27.800E-06
  8
                                            C.0000E+00
       26.450E-06
                    0.000E+00 0.195E+01
  9
        26.075E-06
                     0.000E+00
                               C.201E+01
                                            C.0000E+00
 10
                  0.000E+00
        28.250E-06
                               0.1715+01
                                            C.3000E+00
        27.000E-06
                    0.000E+00
                                            0.0000E+00
                              C.187E+01
                                             C.0000E+00
        27.350E-06
                   0.000E+00
                              C.182E+01
Mean hardness +/- std = 1.877393
                                      8:42T361E-02
 Coefficient of variation for hardness = 4.4888855-00
Mean Kic +/- std =
 Coefficient of variation for Kic =
```

For specimen 2nS spec.M irr. annealed test $800\,^{\circ}\text{C} + 600\,^{\circ}\text{C}$ Indented on 7-31-89

Indent	Load(kg)	a1(um)	a2 (um)	cl(um)	c2 (um)
1	0.30	49.90	48.30	C.00	С.ЭО
2	0.30	50.40	50.40	0.00	C.00
3	C.30	52.30	48.50	C.00	C. 00
4	0.30	48.60	46.50	0.00	0.00
5	0.30	48.00	48.40	C.00	С.ОО
6	0.30	48.40	49.80	0.00	0.00
7	0.30	47.70	49.50	0.00	0.00
8	0.30	48.40	51.40	0.00	C.00
9	0.30	50.50	51.60	0.00	C.00
10	0.30	49.70	48.70	0.00	C.00
11	0.30	47.50	49.40	0.00	0.00
12	0.30	50.50	49.50	C.00	0.00
Break	in 4600				

Эk

Indent	Amean(m)	Cmean(m)	Hard(GPa)	Kic(MPaml/2)
1	24.55 0E-06	0.000E+00	0.226E+01	0.0000E+00
2	25.200E-06	0.000E+00	0.215E+01	0.0000E+00
3	25.200E-06	0.000E+00	0.215E+01	C.0000E+00
4	23.775E-06	0.000E+00	0.241E+01	0.0000E+00
5	24.100E-06	0.000E+00	0.235E+01	0.0000E+00
6	24.550E-06	0.000E+00	0.226E+01	0.0000E+00
7	24.300E-06	0.000E+00	0.231E+01	0.0000E+00
8	24.950E-06	0.000E+00	0.219E+01	0.0000E+00
9	25.525E-06	0.000E+00	0.209E+01	0.0000E+00
10	24.600E-06	0.000E+00	0.225E+01	C.0000E+00
11	24.225E-06	0.000E+00	0.232E+01	0.0000E+00
12	25.000E-06	0.000E+00	0.218E+01	0.0000E+00

Mean hardness +/- std = 2.24517 9.478985E-02 Coefficient of variation for hardness = 4.221947E-02

Mean Kic +/- std = Coefficient of variation for Kic = 0

For specimen ZnS IRR. spec.Q annealed 850 C Indented on 8-10-89

Indent	Load(kg)	al(um)	a2(um)	c1 (um)	c2(um)
1	0.30	47.80	51.30	0.00	0.00
2	0.30	48.60	50.50	0.00	0.00
3	0.30	48.90	50.30	0.00	0.00
4	0.30	45.90	47.90	0.00	0.00
5	0.30	49.40	51.30	0.00	0.00
6	0.30	47.60	51.30	0.00	0.00
7	0.30	48.80	50.00	0.00	0.00
8	0.30	51.30	50.00	0.00	0.00
9	0.30	48.90	48.20	0.00	0.00
10	0.30	47.70	49.80	0.00	0.00
11	0.30	48.50	49.70	0.00	0.00
12	0.30	48.50	52.60	0.00	0.00
_ , .	4 6 0 0				

Break in 4600

Ok

Indent	Amean(m)	Cmean(m)	Hard(GPa)	<pre>Kic(MPam1/2)</pre>
1	24.775E-06	0.000E+00	0.222E+01	0.0000E+00
2	24.775E-06	0.000E+00	0.222E+01	0.0000E+00
3	24.800E-06	0.000E+00	0.222E+01	0.0000E+00
4	23.450E-06	0.000E+00	0.248E+01	0.0000E+00
5	25.175 E- 06	0.000E+00	0.215E+01	0.0000E+00
6	24.725E-06	0.000E+00	0.223E+01	0.0000E+00
7	24.700E-06	0.000E+00	0.224E+01	0.0000E+00
8	25.325E-06	0.000E+00	0.213E+01	0.0000E+00
9	24.275E-06	0.000E+00	0.231E+01	0.0000E+00
10	24.375E-06	0.000E+00	0.230E+01	0.0000E+00
11	24.550E-06	0.000E+00	0.226E+01	0.0000E+00
12	25.275E-06	0.000E+00	0.214E+01	0.0000E+00

Mean hardness +/- std = 2.241701 9.524485E-02 Coefficient of variation for hardness = 4.248777E-02

Mean Kic +/- std = 0 0 Coefficient of variation for Kic = 0

APPENDIX B

BASIC PROGRAM - HARDNESS IN GIGAPASCALS

APPENDIX B

BASIC PROGRAM - HARDNESS IN GIGAPASCALS

```
1000 REM Hardness and toughness calculations
1010 N = 30
1020 DIM KG(N), A1(N), A2(N), C1(N), C2(N)
1040 DIM H(N), KIC(N), AMEAN(N), CMEAN(N), HMEAN(N), KCMEAN(N)
1060 READ NSPEC : REM read the number of specimens, npsec
1100 FOR K = 1 TO NSPEC
1200
              GOSUB 3000 : REM Read input data for specimen
1340
              GOSUB 4000 : REM View input data on CRT
1360 REM
              GOSUB 14000: REM Output initial data to lineprinter
1640
              GOSUB 2000 : REM Compute hardness
1720
              GOSUB 2400 : REM Calculate fracture toughness
1740
              GOSUB 6000 : REM Statistics on hardness
1760
              GOSUB 7000 : REM Statistics on toughness
1820
              GOSUB 5000 : REM Output results to CRT
1860 REM
              GOSUB 15000: REM Output results to lineprinter
1920 NEXT K
1940 END
2000 REM Calculate hardness
2020 FOR I = 1 TO NN
2040 P(I) = KG(I)*9.8 :REM Multiply "mass" by acceleration due to gravity to
2045
                       obtain the load P.
                 REM
2060 CONV = .000001 : REM convert microns (read from Buehler indentor) to meter
2080 A1(I) = A1(I) \pmCONV : A2(I) = A2(I) \pmCONV
2090 C1(I) = C1(I) * CONV : C2(I) = C2(I) * CONV
2120 AMEAN(I) = (A1(I) + A2(I))/4! : REM Amean is the average half-diagonal leng
2140 \text{ ASO} = \text{AMEAN}(I) * \text{AMEAN}(I)
2160 \text{ H(I)} = (.464 * P(I))/ASO
2180 H(I) = H(I) * 9.999999E-10: REM Convert hardness in Pa to GPa
2200 NEXT I
2380 RETURN
2400 REM Calculate fracture toughness
2410 FOR I = 1 TO NN
2420 IF (Cl(I) = 0 \text{ AND } C2(I) = 0) THEN FTEST = 0
2480 \text{ CMEAN(I)} = (C1(I) + C2(I))/2!
2680 CAL = .016 : REM Cal is a material-independent calibration constant
2740 FAC = SQR(E/H(I)) : REM Hard is the calculate hardness for the indent
2750 REM Note: Both E and H are in GPa, so that FAC is unitless
2760 DENOM = CMEAN(I) \star (SQR(CMEAN(I))) : REM Kic depends on cmean to the 3/2 power
2780 KIC(I) = (CAL*FAC*P(I))/DENOM
2820 KIC(I) = KIC(I) \star .000001 : REM Convert Kic in Pam1/2 to MPam1/2
2880 NEXT I
2990 RETURN
3000 REM Input data for specimen
3020 READ SPEC$, DAT$ : REM Read the specimen label and date
3040 READ NN, E: REM read the number of indents for this specimen
3060
                 REM
                       and the Young's modulus E, in GPa
3080 FOR I = 1 TO NN
3100
        READ KG(I), A1(I), A2(I), C1(I), C2(I)
3180 NEXT I
3900 RETURN
4000 REM View initial data
4080 PRINT " " : PRINT " "
4090 PRINT"For specimen ",SPEC$ : PRINT "Indented on ",DAT$ : PRINT " "
i100 A$ = " ###
                      ##.##
                             ###.##
                                          ###.##
                                                    ###.##
                                                               ###.##"
4120 PRINT "Indent
                      Load(kg) al(um)
                                          a2 (um)
                                                    c1 (um)
\pm 300 FOR J = 1 TO NN
        PRINT USING A$;J,KG(J),A1(J),A2(J),C1(J),C2(J)
```

```
4400 NEXT J
4600 STOP
4990 RETURN
5000 REM Output hardness, toughness to CRT 5020 PRINT " " : PRINT " "
5040 PRINT"For specimen ",SPEC$ : PRINT "Indented on ",DAT$ : PRINT " " 5060 B$ = "### ###.###^^^^ #.###^^^^ #.###^^^^ #.###
                                                                  #.####^^^ "
5080 PRINT"Indent
                       Amean(m)
                                     Cmean(m)
                                                   Hard(GPa)
                                                                  Kic(MPam1/2; "
5100 FOR I = 1 TO NN
5140 PRINT USING BS; I, AMEAN(I), CMEAN(I), H(I), KIC(I)
5400 NEXT I
5500 PRINT " "
5600 PRINT "Mean hardness +/- std = ",HMEAN,HSTD
5620 PRINT " Coefficient of variation for hardness = ", HCFV
5800 PRINT " "
5820 PRINT "Mean Kic +/- std = ", KMEAN, KSTD
5840 PRINT " Coefficient of variation for Kic = ", KCFV
5900 STOP
6000 REM This subroutine calculates the mean, variance, standard deviation
5010 REM and coefficient of variation for vector H
5030 \text{ SUM} = 0!
6040 SOSUM = 0!
5050 FOR I = 1 TO NN
5060
        SUM = SUM + H(I)
6080
         SQSUM = SQSUM + H(I) *H(I)
6100 NEXT I
6120 \text{ HMEAN} = \text{SUM/NN}
6140 \text{ HVAR} = (\text{NN*SQSUM} - \text{SUM*SUM}) / (\text{NN*}(\text{NN} - 1!))
6160 HSTD = SQR(ABS(HVAR))
5180 HCFV = HSTD/HMEAN
5900 RETURN
7000 REM This subroutine calculates the mean, variance, standard deviation
7010 REM and coefficient of variation for vector KIC
^{\circ}030 SUM = 0!
7040 \text{ SQSUM} = 0!
7050 FOR I = 1 TO NN
7060
        SUM = SUM + KIC(I)
080
        SOSUM = SQSUM + KIC(I)*KIC(I)
7100 NEXT I
~120 KMEAN =
              SUM/NN
^{140} KVAR = (NN*SQSUM - SUM*SUM)/(NN*(NN - 1!))
~160 KSTD = SQR(ABS(KVAR))
~180 KCFV = KSTD/KMEAN
7900 RETURN
14000 REM View initial data
14080 LPRINT " " : LPRINT " "
14090 LPRINT"For specimen ",SPEC$ : LPRINT "Indented on ",DAT$ : PRINT " "
14100 AS = " ###
                        ##.##
                                ###.## ###.##
                                                       ###.## ###.##"
14120 LPRINT "Indent
                         Load(kg) al(um)
                                              a2(um)
                                                         c1 (um)
                                                                    c2 (um) "
14300 \text{ FOR } J = 1 \text{ TO NN}
         LPRINT USING A$;J,KG(J),A1(J),A2(J),C1(J),C2(J)
14320
14400 NEXT J
14990 RETURN
15000 REM Output hardness, toughness to lineprinter 15020 LPRINT " " : LPRINT " "
15040 LPRINT"For specimen ",SPEC$ : LPRINT "Indented on ",DAT$ : PRINT " "
15060 B$ = "### ###.###^^^^ #.###^^^^ #.###^^^^ #.###^^^^ "
15080 LPRINT"Indent
                         Amean(m)
                                         Cmean(m)
                                                      Hard(GPa)
                                                                    Kic(MPam1/2) "
15100 FOR I = 1 TO NN
```

LIST OF REFERENCES

- Paul Kuttner, "Measuring The Critical Properties Of Infrared Optical Materials," Laser Focus/Electro Optics, April 1985, pp. 91-99.
- 2. D. F. Horne, <u>Optical Production Technology</u>, 2 ed., Ch.8, Adam Hilger Ltd., Bristol, 1983.
- 3. Kenneth Krane, Modern Physics, Ch.3, John Wiley and Sons, Inc., 1983.
- 4. E. D. Case and A. G. Evans, "Length Of Maximal Impact Damage Cracks As A Function Of Impact Velocity," Proc. Int. Conf. on Erosion by Liquid and Solid Impact, University of Cambridge, 1983.
- 5. E. D. Case, K. M. Louie, and A. G. Evans, "Statistical Analysis Of Damage Induced By Water Drop Or Water Jet Impact," Journal of Materials Science Letters, 3, 1984, pp. 879-884.
- 6. J. E. Field, S. van der Zwaag, and D. Townsend, "Liquid Impact Damage Assessment For A Range Of Infra-Red Materials", Proc. 6th Int. Conf. on Erosion by Liquid and Solid Impact, University of Cambridge, 1983.
- I. W. Donald and P. W. McMillan, "Review: Infra-Red Transmitting Materials: Part 1, Crystalline Materials," Journal of Materials Science, 13, 1978, pp. 1151-1176.
- 8. R.S. Averback and M.A. Kirk, "Atomic Displacement Processes in Ion Irradiated Materials", <u>Surface Alloying by Ion, Electron, and Laser Beams</u>, eds. L.E. Rehn, S.T. Picraux, H. Wiedersich, American Society for Metals, Metals Park, 1985.
- 9. David K. Brice, <u>Ion Implantation Range & Energy</u>
 <u>Deposition Distributions</u> Vol. 1, 1975, IFI/Plenum,
 New York, p.1.

- 10. J.K. Hirvonen, ed., <u>Treatise On Materials Science And Technology: Ion Implantation</u> Vol. 18, 1980, Academic Press, New York.
- 11. W. Hayes and A.M. Stoneham, <u>Defects and Defect Processes</u>
 <u>in Nonmetallic Solids</u>, John Wiley and Sons, 1985.
- 12. I.J. McColm and N.J. Clark. <u>Forming, Shaping and Working of High-Performance Ceramics</u>, 1986 Chapman and Hall, New York, p.334.
- 13. P.J. Burnett and T.F. Page, "Surface softening in silicon by ion implantation", Journal of Materials Science, 19, (1984), pp. 845-860.
- 14. C.J. McHargue, et. al. "Microstructure and Properties of TiB₂ Implanted with 1 MeV Nickel", Nuclear Instruments and Methods, B1 (1984) pp. 246-252.
- 15. A.G. Evans, (S.W. Freiman, ed.), <u>Fracture Mechanics</u>
 <u>Applied to Brittle Materials</u>, American Society for
 Testing Materials, Philadelphia, PA, 1979, p.112.
- 16. R.H. Marion, Ref. 15, p.103.
- 17. C.J. McHargue, et. al., "The Structure and Properties of Ion-Implanted Al₂0₃", Nuclear Instruments and Methods, B10/11, 1985, pp. 569-573.
- 18. T. Hioki, et. al., "Effect of Ion Implanation on Fracture Stress of Al_2O_3 ", Nuclear Instruments and Methods, B7/8, 1985, pp. 521-525.
- 19. T. Hioki, et. al., Journal of Materials Science Letters, (in press).
- 20. G.B. Krefft and E.P. EerNisse, Journal of Applied Physics, Vol. 49, 1978, pp. 2725-2730.
- 21. Y.S. Touloukian, R.K. Kirby, R.E. Taylor and T.Y.R. Lee, "Thermal Expansion, Nonmetallic Solids," <u>Thermophysical</u> <u>Properties of Matter Vol. 13</u>, Plenum, New York, 1977.

- 22. K.O. Legg, et. al., "Modification of Surface Properties of Yttria Stabilized Zirconia by Ion Implantation, Nuclear "Nuclear Instruments and Methods, B7/8, 1985, pp. 535-540.
- 23. Carl J. McHargue, "Structure and Mechanical Properties of Ion Implanted Ceramics", Nuclear Instruments and Methods, B10/11, 1987, pp. 1127-1133.
- 24. C.H. Mathewson, <u>Zinc: The Science and Technology of the Metal, Its Alloys and Compounds</u>, Plenum, New York, 1967.
- 25. B. Cooper, "IR Window Advances: FLIRS and Beyond," Photonic Spectra, Oct., 1988, pp. 149-156.
- 26. Max Hansen, <u>Constitution of Binary Alloys</u>, McGraw-Hill Book Company, Inc. New York, 1958, p.1171.
- 27. R. C. Wheast, ed. <u>Handbook of Chemistry and Physics</u> 62nd ed., 1981-82, CRC Press, p.f-54.
- 28. W. D. Kingery, Bowen, Uhlmann, <u>Introduction to Ceramics</u>
 John Wiley and Sons, Inc., New York, 1976, p.63.
- 29. D. F. Horne, Optical Production Technology, 2 ed. 1983, Adam Hilger Ltd., Bristol, p.249.
- 30. M. V. Swain, "Nickel sulphide inclusions in glass: an example of microcracking induced by a volumetric expanding phase change," Journal of Materials Science, 16, 1981, pp. 151-158.
- 31. W. M. Kriven, "Possible Alternative Transformation Tougheners to Zirconia: Crystallographic Aspects," (in press) Dept. of Materials Science and Engineering., University of Illinois at Urbana-Champaign.
- 32. G. Thomas and M.J. Goringe, <u>Transmission Electron</u>
 <u>Microscopy of Materials</u>, John Wiley and Sons, Inc.,
 New York, 1979, p.13.
- 33. Powder Diffraction File, Joint Committee on Powder Diffraction Standards, International Centre for Diffraction Data, Swarthmore, PA.
- 34. B.D. Cullity, <u>Elements of X-ray Diffraction</u>, Addison Wesley Pub. Co., Reading, MA., 1978, p.84.

- 35. Beeston, Horne, and Markham, <u>Electron Diffraction and Optical Diffraction Techniques</u>, American Elsevier Pub. Co. Inc, New York, 1973, Ch.4.
- 36. C.R. Rarey, J. Stringer and J.W. Edington, Trans. A.I.M.E., Vol. 236, p.811.
- 37. P. Worthington, "Observation of Polytypes and Stacking Faults in Zinc Sulphide by Transmission Electron Microscopy," Journal of Materials Science, Vol. 8, 1973, pp. 1194-1200.
- 38. D.S. Grummon and E.D. Case, private communication.
- 39. Gatan Corp. Dimple Grinder Model 686 Operations Manual.
- 40. G. Kullerud and R.A. Yund, "The Ni-S System and Related Minerals," Journal of Petrology, Vol. 3, Part 1, 1972, pp. 126-175.
- 41. H.H. Woodbury, "Diffusion and Solubility Studies,"

 <u>Physic and Chemistry of II-VI Compounds</u>, Aven and Prener p.232.
- 42. Paul G. Shewmon, <u>Diffusion in Solids</u>, J. Williams Book Co., Jenks, OK, 1983.

MICHIGAN STATE UNIV. LIBRARIES
31293010432064